Modelling of Atomization and Vaporization in Industrial Gas Turbine Injectors

Dominic Luke Moffat

School of Mechanical Engineering

University of Leeds

Submitted in accordance with the requirements for the degree of

Doctor of Philosophy

May 2016

The candidate confirms that the work submitted is his own, except where work which has formed part of jointly-authored publications has been included. The contribution of the candidate and the other authors to this work has been explicitly indicated below. The candidate confirms that appropriate credit has been given within the thesis where reference has been made to the work of others.

Chapter 3 contains reference to work which was presented in a paper at ASME Turbo Expo 2013 and was co-authored with Dr Alexey Burluka of the University of Leeds. The reference is listed below:

Moffat, D.L and Burluka, A.A. (2013,Jun). Modelling of a turbulent jet in a gas cross-flow. *In proc. ASME Turbo Expo*, San Antoino, GT2013-94309.

Acknowledgements

My parents, David and Carolyn Moffat. Thank you for everything.

My supervisor, Dr Alexey Burluka, for wisdom and encouragement throughout this endeavour.

Siemens, Lincoln, in particular: Dr Jim Rogerson, Dr Suresh Sadasivuni and Dr Ghenadie Bulat for their support and assistance.

Abstract

In many industrial gas turbine combustors the injection of liquid fuel resembles the simple configuration of a jet in a rectangular channel with cross-flowing air, albeit with complex geometry both upstream and downstream from the channel. Therefore the detailed study of a jet in cross flow is an appropriate platform for the development of models for atomization and vaporization, both of which are key processes influencing efficiency and the emissions of pollutants from practical combustion devices. In the current study the breakup of a liquid jet and vaporization of droplets are modelled using an entirely Eulerian approach, where the liquid phase is treated analogously to a gas species in a multi-component reacting mixture. A novel boundary condition is proposed for the liquid surface area per unit mass at the jet inlet, and results are found to be insensitive to adjustments of the size parameter for this boundary condition.

Validation is carried out in two stages: firstly turbulence closure via the Reynolds Averaged Navier–Stokes (RANS) approach with the standard constants is assessed for a gas-phase jet in cross flow with two different software packages; then predictions of the Sauter mean diameter of droplets are compared to measurements of a liquid jet in cross flow at 6 bar pressure. The turbulence model yields a reasonably accurate prediction of the flow field provided that the distribution of velocity across the jet inlet is specified. Droplet sizes agree well with the experiment except for a small region near the floor of the channel, where discrepancies can be attributed to the RANS closure. Application of the model is demonstrated for an industrial gas turbine combustor at its full load operating condition.

Abbreviations

B	Spalding transfer number
c_p	specific heat capacity (kJ/kgK)
D_{32}	Sauter mean diameter (m)
D_t	turbulent diffusivity (m^2/s)
ϵ	turbulent kinetic energy dissipation rate (m^2/s^3)
k	turbulent kinetic energy (m^2/s^2)
L	latent heat (enthalpy) (kJ/kg)
$\dot{m}_{\text{vap}}$	vaporization rate per unit surface area (kg/m^2s)
μ	dynamic viscosity (kg/ms)
ν	kinematic viscosity (m^2/s)
q	jet momentum ratio
Re	Reynolds number
ρ	density (kg/m^3)
S_c	Schmidt number
Σ	droplet surface area per unit mass (m^2/kg)
We	Weber number
Y	mass fraction
ω	specific turbulent kinetic energy dissipation rate (s^{-1})

DNS	Direct Numerical Simulation
ELSA	Eulerian–Lagrangian Spray Atomization
LES	Large Eddy Simulation
RANS	Reynolds Averaged Navier–Stokes

Contents

List of Figures

List of Tables

Chapter 1

Introduction

1.1 Motivation

In recent years concerns about anthropogenic climate change and the harmful effects of emissions on human health have prompted efforts to reduce mankind's dependence on fossil fuels for energy. Yet the need to keep pace with global energy demand, e.g. by replacing power plants with more efficient units as they reach the end of their productive life, presents a challenge for industry and policymakers (IEA, 2014). A major contribution is expected to come from technological advancements in response to increasingly stringent regulatory limits on the emissions of NO_x, CO, and particles such as soot. To a large extent these regulations dictate the market conditions in the power sector and affect many fields of engineering including internal combustion engines, and aerospace and industrial gas turbines.

For liquid-fuelled combustion devices, where the rates of chemical reactions are relatively fast and the flow is usually highly turbulent, the rate of vaporization and hence atomization of the liquid are key limiting factors affecting efficiency and the emissions of pollutants (Lefebvre, 1989). Therefore the design of next-generation combustors depends crucially upon understanding these processes. However the physics of liquid breakup due to turbulent straining is extremely complex and difficult to model despite the increasing accessibility of high performance computing to tackle the problem (Demoulin et al., 2013).

1.2 Objectives

The focus of the current study is the breakup and vaporization of a liquid jet in cross flow. In this context, the primary objective is to validate the predictions of an entirely Eulerian model, known as the Σ–Y_{liq} model, which has previously been applied to various air-assisted atomization and vaporization cases (Beheshti et al., 2007; Sidhu and Burluka, 2008). Implementation of the model in a commercial CFD package serves another goal, which is to provide insights relevant to the industrial design process for liquid-fuelled gas turbine combustors.

1.3 Structure of Thesis

Background information relating to the physics of jets in cross flow and modelling approaches for atomization and vaporization are presented in Chapter 2. Following a review of the various different closure methods for turbulence, the phenomena of liquid breakup and vaporization are described, then the Σ–Y_{liq} model is explained in detail. The submodel for droplet vaporization is presented, along with a novel boundary condition for the liquid surface area per unit mass at the jet inlet.

In Chapter 3 the ability of the Reynolds Averaged Navier–Stokes (RANS) turbulence model to capture the aerodynamic structure of a jet in cross flow is assessed by comparison with measurements of a gas-phase jet by Crabb et al. (1981). RANS simulations with the standard model constants are carried out using two different software packages, and a Large Eddy Simulation (LES) is also performed. Additional simulations include RANS and LES cases with different jet momentum ratios to illustrate the effect on the predicted flow field.

Chapter 4 compares the results of the Σ–Y_{liq} model with droplet size measurements carried out at the German Aerospace Centre (DLR) for a liquid kerosene jet in cross flow at 6 bar pressure (Becker, 2004). Four test cases are studied including two different cross flow velocities and two jet momentum ratios. An additional simulation (without validation data) is carried out at elevated temperature to demonstrate the vaporization submodel. Finally, in Chapter 5 a

nonreacting simulation of the Siemens SGT-400 combustor at its full load operating condition is presented. Diesel atomization-only and vaporization cases are compared in terms of the Sauter mean diameter of droplets in the region immediately upstream from the main combustion chamber. The findings of the thesis are summarized in Chapter 6, where recommendations for future work are also given.

Chapter 2

Background

This chapter covers relevant background material and previously conducted studies which will elaborate on the work performed within this field. The fundamental governing equations of fluid mechanics are covered first, followed by a review of jet in cross flow studies and liquid modelling. Computational approaches to these topics are then considered along with an outline of important CFD considerations. Application of the Σ–Y_{liq} model to various different systems is then presented along with the modifications and assumptions made during the current study.

2.1 Turbulent Flows

2.1.1 Governing Equations

The following are the equations for momentum and continuity of a two-dimensional fluid system. Multiple assumptions are made here, including incompressibility and constant physical properties (Alfonsi, 2009).

$$\frac{\partial u}{\partial t} + u\frac{\partial u}{\partial x} + v\frac{\partial u}{\partial y} = -\frac{\partial p}{\partial x} + \nu\left(\frac{\partial^2 v}{\partial x^2} + \frac{\partial^2 u}{\partial y^2}\right) \tag{2.1}$$

$$\frac{\partial v}{\partial t} + u\frac{\partial v}{\partial x} + v\frac{\partial u}{\partial y} = -\frac{\partial p}{\partial x} + \nu\left(\frac{\partial^2 v}{\partial x^2} + \frac{\partial^2 v}{\partial y^2}\right) \tag{2.2}$$

$$\frac{\partial u}{\partial x} + \frac{\partial v}{\partial y} = 0 \tag{2.3}$$

Turbulence

Turbulence refers to the random instabilities and fluctuations within a fluid and by utilising Reynolds decomposition, the Reynolds Averaged Navier–Stokes equations can be formed. This consists of the separation of a quantity into a mean and fluctuating component, as detailed in Kleinstreuer (2003) and Hinze (1975), which takes the form of Eq. (2.4) below:

$$u = \bar{u} + u' \tag{2.4}$$

Substituting Eq. (2.4) into Eqs. (2.1)–(2.3) and neglecting higher order times yields the Reynolds-averaged Navier–Stokes equations (for a 2D flow):

$$\frac{\partial \bar{u}}{\partial t} + \bar{u}\frac{\partial \bar{u}}{\partial \bar{x}} + \bar{v}\frac{\partial \bar{u}}{\partial \bar{y}} = -\frac{\partial \bar{p}}{\partial \bar{x}} + \frac{\partial}{\partial y}\left(\nu\frac{\partial \bar{u}}{\partial y} - \overline{u'v'}\right) \tag{2.5}$$

A closure is needed to account for the turbulent stress components generated as a result of this averaging (Kleinstreuer, 2003). Equation (2.6) describes the viscous stress in a laminar flow and inspired a similar approach for turbulence. Turbulent viscosity, described in Launder and Spalding (1972), was an approximation suggested by Boussinesq where the turbulent shear stress is replaced by the product of the mean velocity gradient, μ_t.

$$\tau_{ij} = \mu\left(\frac{\partial u_j}{\partial x_i} + \frac{\partial u_i}{\partial u_j}\right) \tag{2.6}$$

$$\left(\overline{u'v'}\right) = -\mu_t\left(\frac{\partial \bar{u}}{\partial y} + \frac{\partial \bar{v}}{\partial x}\right) \tag{2.7}$$

The Reynolds number is a measure of how turbulent a flow is, dependent upon the velocity, viscosity and density of the medium along with the characteristic length scale of the flow. This is given in Massey and Ward-Smith (2006) as:

$$Re = \frac{\rho u l}{\mu} \tag{2.8}$$

With a value of 400 used to define the separation between a laminar and turbulent flow, this dimensionless number is a ratio of the fluid inertia forces

to the viscous forces, where l is the width of the domain, assuming that the flow is internal (Massey and Ward-Smith, 2006). Laminar flow does not exhibit any turbulence characteristics and has no fluctuations within any of its component quantities, whilst turbulent flow contains these random fluctuations as per Eq. (2.4).

It has been observed that a singular change in the Reynolds number only has little effect on the flow, but a change in the inlet velocity, which alters both the Reynolds and Weber numbers, causes an increase in the number of small-scale liquid structures (Desjardins and Pitsch, 2010). This increase in the number of small scale eddies at high Reynolds number has an effect on the boundary layer turbulence (Metzger and Klewicki, 2001).

2.1.2 Turbulence Closures

In order to successfully model a flow, the averaged Navier–Stokes equations must be closed to account for the additional stress terms. There are numerous approaches to this problem, each with its own merits and disadvantages and their selection can depend heavily on the availability of computational resources and applicability to the problem in question.

RANS

The Reynolds averaged Navier–Stokes (RANS) approach refers to the averaging of the Navier-Stokes equations, to describe a fluid flow. However in both incompressible and compressible cases, CFD solvers are frequently structured around the use of Favre averaged equations, which are density weighted. These take the following form (Hinze, 1975) :

$$\bar{\rho}\left(\frac{\partial \widetilde{u_i}}{\partial t} + \widetilde{u_j}\frac{\partial \widetilde{u_j}}{\partial x_j}\right) = -\frac{\partial \bar{p}}{\partial x_i} + \frac{\partial}{\partial x_j}\left(\mu\left(\frac{\partial \widetilde{u_i}}{\partial x_j} + \frac{\partial \widetilde{u_j}}{\partial x_i}\right) - \bar{\rho}\overline{u'v'}\right) \tag{2.9}$$

These density weighted equations reduce the number of turbulence terms in comparison to the unfiltered Navier-Stokes equations for compressible fluids, but has the effect of not being applicable in a Lagrangian framework due to taking into account the changes in both volume and mass, making it rely on a Eulerian

only framework, one of the key assumption in the application of the Σ-Y_{liq} model (Hinze, 1975). These problems are solved using a finite volume approach (Kim and Benson, 1992), which is applicable to a round jet in cross flow for a k-ε closure.

Roache (1998) outlines the process of developing RANS turbulence modelling as the averaging of the velocity fluctuations over time scales which are not directly resolved in the computations due to their small size. It is from this process which the Reynolds stresses are introduced: $\overline{u'_i u'_j}$.

The relation of the turbulent fluctuations to large-scale flow characteristics is modelled through the use of additional equations in order to provide a closure (Roache, 1998). There are multiple examples of these including the mixing length hypothesis, one-equation and two-equation models such as k-ε and k-ω proposed by Jones and Launder (1972) and Wilcox (1988) respectively. Throughout this study, it is the two-equation type turbulence models which were utilised due to their extensive use in industry (Menter et al., 2003).

An evaluation of the RANS approach against a modified version, Unsteady RANS (URANS), was conducted in Ivanova et al. (2010) and Ivanova et al. (2009). It was found that the traditional RANS approach had difficulty predicting the velocity fields due to the steady-state nature, URANS solves in an unsteady state, resolving large-scale turbulence structures with respect to time. Alfonsi (2009) also reviews the capabilities of URANS, addressing the issue of closure in conventional RANS approaches which prevent the solving of the Navier-Stokes equations in unsteady form.

The effect of this approach is an improvement in the velocity structure predictions even when using an identical turbulence model to the steady-state RANS counterpart. Both studies show improvements to velocity peaks and stress predictions, despite a dependence on the associated turbulence model to calculate the turbulent kinetic energy compared to LES (Ivanova et al., 2010).

RANS Turbulence Models

k–ε Model

One of the more commonly used two-equation turbulence models is the k-ε model, presented in unmodified form by Launder and Sharma (1974) and defined in Mohammadi and Pironneau (1993) as equations which represent the turbulent kinetic energy, Eq. (2.10), and its rate of dissipation, Eq. (2.11).

$$\frac{\partial \rho k}{\partial t} + \frac{\partial \rho \bar{u} k}{\partial x_i} - \frac{\partial}{\partial x_j}\left(\rho \frac{\nu + \nu_t}{\sigma_k}\right)\frac{\partial k}{\partial x_i} = 2\rho\nu_t\left(\frac{\partial \bar{u}_i}{\partial x_i} + \frac{\partial \bar{u}_j}{\partial \bar{x}_j}\right)\frac{\partial \bar{u}_i}{\partial x_i} - \rho\epsilon \tag{2.10}$$

$$\frac{\partial \rho \epsilon}{\partial t} + \frac{\partial \rho \bar{u} \epsilon}{\partial x_i} - \frac{\partial}{\partial x_j}\left(\rho \frac{\nu + \nu_t}{\sigma_\epsilon}\right)\frac{\partial \epsilon}{\partial x_i} = C_1 2\rho\nu_t\left(\frac{\partial \bar{u}_i}{\partial x_i} + \frac{\partial \bar{u}_i}{\partial \bar{x}_j}\right)\frac{\partial \bar{u}_i}{\partial x_i}\frac{\epsilon}{k} - C_2\frac{\epsilon^2}{k} \tag{2.11}$$

This model represents one of the most used two-equation closures for the RANS method both in industry and academia for a wide range of flows. Whilst the previous equations represent the basic model, there have been a number of modifications over time in an attempt to improve predictions for specific flow types (Alfonsi, 2009).

A study conducted by Balabel and El-Askary (2011) examines the applications of the standard k-ε turbulence model in a variety of jet flows including free jet, wall jet and impinging jet. They observed that although the standard k-ε performed to good agreement with mean velocity characteristics when examining simple engineering flows, the magnitude of the predictions was severely affected for the more complex flow structures (Balabel and El-Askary, 2011). This is a well documented occurrence, covered in several other texts including Keimasi and Taeibi-Rahni (2001) and Javadi et al. (2007).

k–ω Model

A variant of a two-equation turbulence model which predicts the turbulent kinetic energy along with its specific dissipation rate which is dependent upon the scale used for the flow modelling. This model, proposed and modified by Wilcox (1988) has come into increasing use due to the difference in prediction in comparison to k–ε; particularly in regions of high shear flow.

$$\frac{\partial \rho k}{\partial t} + \frac{\partial \rho \bar{u} k}{\partial x_i} - \frac{\partial}{\partial x_j}\left(\rho \frac{\nu + \nu_t}{\sigma}\right)\frac{\partial k}{\partial x_i} = -\beta k\omega + \tau_{ij}\frac{\partial \bar{u}}{\partial x_i} \tag{2.12}$$

$$\frac{\partial \rho \omega}{\partial t} + \frac{\partial \rho \bar{u} \omega}{\partial x_i} - \frac{\partial}{\partial x_j}\left(\rho \frac{\nu + \nu_t}{\sigma}\right)\frac{\partial k}{\partial x_i} = -\beta\omega^2 + \frac{\sigma_d}{\omega}\frac{\partial k}{\partial x_i}\frac{\partial \omega}{\partial x_i} + a\frac{\omega}{\bar{k}}\tau_{ij}\frac{\partial \bar{u}}{\partial x_i} \tag{2.13}$$

The near-wall behaviour of RANS based turbulence models was evaluated in Speziale et al. (1992), concluding that both the k-ε and k-ω have issues when dealings with solid walls. Whereas k-ε suffers from numerical stiffness for the dissipation rate near walls, (Speziale et al., 1992), the original k-ω model may cause issues due to lack of dissipation near walls. To this end, wall functions have been developed to address these models and improve the model predictions in near-wall situations.

A common derivative of the k–ω model is the variant presented in Menter (1994) and reviewed in Menter (2009), k–ω–SST, which is designed to predict shear-stress transport and improve predictions at walls, regarding the sensitivity of the k–ω model outside of boundary layers whilst retaining the improved free-stream predictions of k–ε.

Comparisons between the k-ε and k-ω–SST models have been conducted for many different flow types. Javadi et al. (2007) examines the differences between results for a turbulent jet in cross-flow. Findings indicated that the separation between predictions increased with the increase of the velocity ratio, suggesting that although the mean flow is more dependent upon the eddy viscosity for flows with a low pressure gradient, any complex flow field is more suited to a variant of the k-ω–SST model rather than k-ε (Javadi et al., 2007).

RANS Turbulent Averaging

The steady-state nature of the RANS simulations mean that there is no fluctuation in the velocities or turbulence quantities at any of the boundary conditions with time and the entire internal field is modelled rather than directly calculated. As a result of this, the simulation will term to a single solution value which will not change with respect to time. Then any average quantities needed for analysis can be obtained, ensuring the deviation from the average obtained once the

simulation has reached convergence is very low when compared to previous time steps.

$$\bar{u}(x) = \frac{1}{N} \sum (u(x_n)) \tag{2.14}$$

Reynolds averaging is shown here as an example. In reality CFD solvers solve using Favre or density-weighted transport equations. However, an example such as a scenario representing two gas flows with no variation in density and using an incompressible solver means the two equate for this instance. The estimation of the turbulent kinetic energy for the boundary conditions is based upon the 3 individual Cartesian velocity components, after separation of the flow into the average and turbulent components and then substituted for:

$$k = \frac{1}{2} \left(u_x'^2 + u_y'^2 + u_z'^2 \right) \tag{2.15}$$

This assumption means that for the bulk flow the RMS velocity of the turbulent flow can be defined as:

$$\bar{(u_x'^2)}^{\frac{1}{2}} \simeq k \tag{2.16}$$

However since each directional flow component is not modelled individually as in LES, the following supposition must be made in order to predict the remaining RMS velocity components which equates the y and z components as they are unable to be calculated individually due to the definition of Eq. (2.17).

$$u_x^2 = u_y^2 = u_z^2 \tag{2.17}$$

For jet and wake-type flows where the main flow direction is aligned with an average x velocity component and is much larger than the y or z components, the approximate relationship between the RMS components is as Eq. (2.18). This equation is not universal and locally, where there is no dominance of the flow in a single direction, the approximate relationship is as Eq. (2.17).

$$u_x'^2 = 2u_y'^2 = 2u_z'^2 \tag{2.18}$$

Finally, the Reynolds stress components can be calculated from the turbulent viscosity and the change in velocity components respectively.

$$-\frac{1}{2}\mu_t\left(\frac{\partial(u_x)}{\partial y}+\frac{\partial(u_y)}{\partial x}\right) \tag{2.19}$$

Overall, the RANS averaging for the RMS velocity possess several limitations due to the steady-state nature of the problem. The lack of direct calculation of terms instead of modelling means that multiple assumptions have to be made with regards to the flow turbulence characteristics. These assumptions limit the level of refinement of variables when determining the flow structure.

LES

An alternative CFD approach to the RANS method is that of the Large Eddy Simulation or LES. Lesieur (2008) outlines the LES process where the flow is divided into large and small scales by a filter, with the unknown small scales being modelled whereas the larger are directly resolved.

Anderson et al. (1984) notes that whilst the methodology for calculating LES flow turbulence is similar to RANS in that it computes through a closed set of filtered Navier-Stokes equations, there are a number of crucial differences. The first is the use of spatial rather than temporal averaging used in RANS, see RANS approach and averaging of the simulation quantities (Anderson et al., 1984). The second is the difference in handling of the stress terms, which are significantly smaller in LES due to the use of a sub-grid scale stress tensor (SGS) model which resolves all stress below a pre-set filter size which is applied to the computational grid, leaving the Navier-Stokes equations to account for all large scale eddies (Anderson et al., 1984). A thorough supporting guide to the LES method is found within Pope (2004). Since the application of LES can be used to predict more complex flows, it has been seen to have been coupled with various additional models for use in particular fields, such as combustion. One approach to the filtering of the Navier-Stokes equations is presented in Germano (1992).

Unlike RANS there is no required separate turbulence model required for closure, this is instead replaced by a sub-grid scale model used to predict the small eddies. With the increase in computing power over the last 2 decades,

LES is becoming far more widely used. In acknowledgement to this, Pope (2004) addresses several key aspects for the conduction an LES simulation, noting in particular the importance of the filter size needed for a sub-grid scale model. Stating the importance of turbulent length scale, Pope (2004) also acknowledges that the accuracy of LES results may depend upon the chosen value for this length scale which in itself depends upon the flow being examined. Examples of applied LES modelling for a round jet can be found in Yuan et al. (1999), confirming the ability of an LES to produce similar results to RANS predictions despite the differences in methods and modelled fields.

Another crucial aspect of LES concerns the inlet boundary conditions, which are now subject to time and spatial averaging as with the rest of the flow in comparison to the steady state conditions used for RANS. Multiple reviews of LES inlet boundaries can be found in Dietzel et al. (2014), Montomoli and Eastwood (2011) and Tabor and Baba-Ahmadi (2010). Each outlines the different approaches used to generate flow at inlets, addressing the various types in current use:

- Random fluctuations or 'white noise', which is observed as being too dissipative, particularly in turbomachinery applications Montomoli and Eastwood (2011) and lacks quality as to not conform to any temporal scale present within the main flow Tabor and Baba-Ahmadi (2010).

- Diffused noise generate velocity fluctuations based upon given length scales and RMS values. This approach generates mostly large scale structures, which are directly resolved as part of the Navier-Stokes equations but does not account for small-scale features (Dietzel et al., 2014).

- Fourier schemes, which can predict velocities at appropriate scales when supplied with additional information and has been associated with RANS-LES hybrid methods (Tabor and Baba-Ahmadi, 2010).

- Alternatively it is possible to construct libraries of information on turbulence from additional LES simulations and apply these as inlet conditions, with the advantages of real-turbulence scales applied to the problem but as a result of largely increased computational cost to provide the initial

information as the data must be relevant to the flow under examination to establish the correct scales (Tabor and Baba-Ahmadi, 2010).

For a turbomachinery application, Montomoli and Eastwood (2011), covers how the choice of inlet conditions can affect the spread of a jet from the inlet along with a focus on the greater computational cost required in order to provide sufficient domain space for the turbulent flow to naturally develop or utilising conditions from a previous LES simulation if complex geometry is required as this can alter the scale of turbulence. In addition, Fureby (2008) links the trend in computational power increase and availability to the rise in use of the LES method in industry rather than the more common RANS approach, with the focus being on increased prediction accuracy thanks to unsteady prediction capability.

Sub-grid Scale Modelling

With the sub-grid scale model such an integral part of LES method, there are many different versions which have been developed. Fureby et al. (1997) examined a range of separate SGS models, grouped into numerous categories and evaluated the differences. Despite the changes in large-scale flow predictions being small, the choice of SGS was shown to be of little consequence providing the computational grid was refined to a sufficient degree (Fureby et al., 1997). The small-scale predictions, however, did vary greatly upon examination, in particular with complex flow phenomena including vortices. This suggested that whilst no individual SGS model was capable of predicting all flow features, it was the individual flow under study which determined what type of model is most suitable providing it is the small-scale features which are of primary importance (Fureby et al., 1997).

The wall behaviour of an LES approach where the grid needs to be heavily refined in order to successfully use the SGS model within this region to capture small-scales, however this adds heavily to the computational cost of an LES simulation and can depend upon the type of SGS model employed.

An approach detailed in Nikitin et al. (2000) evaluates using detached eddy simulation (DES) coupled with RANS equations at the wall boundaries to alter the SGS model at the boundary in order to reduce computational costs. Another variation upon the standard LES approach is implicit LES which does not utilise

sub grid scale modelling and instead relies on modified Navier-Stokes equations which have been discretised with high order schemes (Kokkinakis and Drikakis, 2015).

Smagorinsky/Eddy Viscosity Models

One of the most commonly used SGS models is that proposed by Smagorinsky (1963), which is defined as an eddy viscosity model used to relate it to the sub-grid scale stresses. Majander and Siikonen (2002) evaluates multiple Smagorinsky based SGS models including multiple versions of the updated dynamic version (Germano et al., 1991) in which multiple filters are used to correct the SGS predictions. Findings from this study raised several issues, stating that a high-order scheme was necessary to improve the results of the dynamic models on a suitably refined grid for a low Reynolds number flow. For a higher Reynolds number flow, the dynamic SGS models can improve stability in the central flow (Majander and Siikonen, 2002), however it was noted that all models require a fine grid to improve predictions. Lesieur (2008) additionally notes that the dissipation of the standard Smagorinsky SGS model is very high in close-wall regions. This is also mentioned in Argyropoulos and Markatos (2015) which addresses the issue as being the eddy viscosity prediction at walls along with the requirement to set the Smagorinsky constant for each flow.

Ultimately, it is the sub-grid scale model which models the small scale eddy phenomena whereas the large scale flow features are solved from filtered Navier–Stokes equations.

$$\tau_{ij} = 2\mu_t S_{ij} \tag{2.20}$$

$$S_{ij} = \frac{1}{2}\left(\frac{\partial \bar{u_i}}{\partial x_j} + \frac{\partial \bar{u_i}}{\partial x_j}\right) \tag{2.21}$$

$$\mu_t = \rho\left(C_s \nabla^2 \sqrt{(S_{ij} S_{ij})}\right) \tag{2.22}$$

Further modifications to the dynamic Smagorinsky model can be found in Lilly (1992), which optimises the correlation between the closed solution to the equations against the directly resolved stresses.

LES Turbulent Averaging

Unlike RANS averaging, LES averaging does not rely on reaching a single converged average value, but instead must be run for a suitable length of time in order to adequately represent the flow.

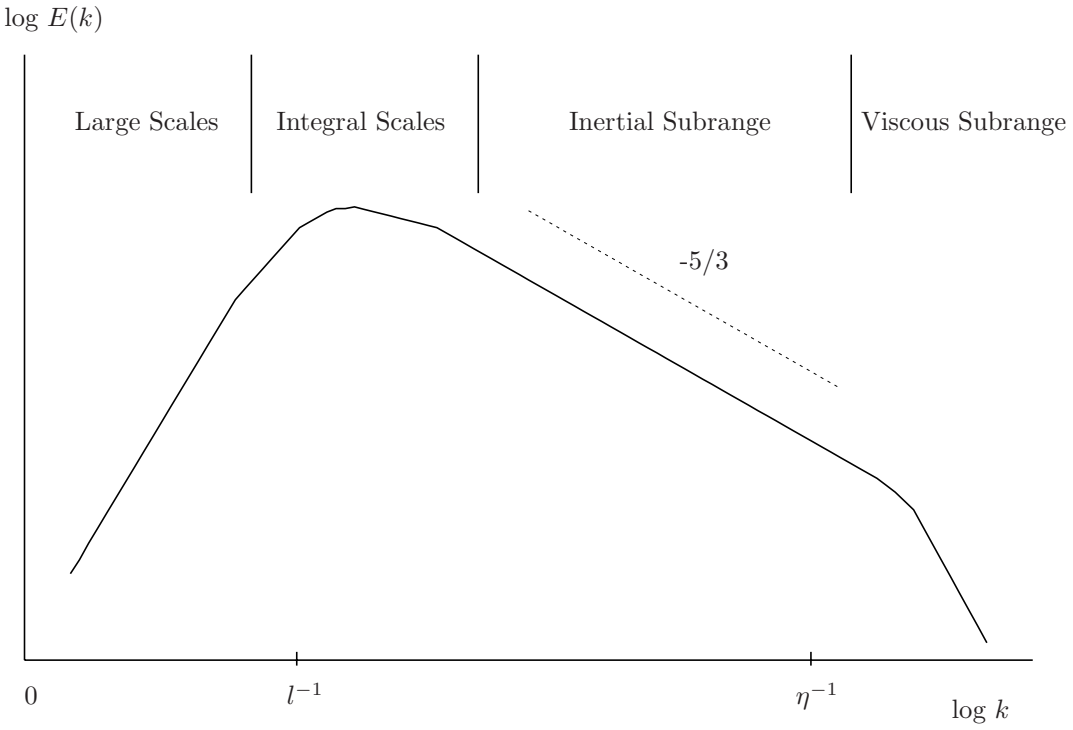

Figure 2.1: Energy spectrum (after Peters (2000)).

Figure 2.1 illustrates the importance of averaging correctly in order to capture the small-scale features of the flow by showing the level of turbulent energy against various time scales needed to resolve the problem due to the separation of large and small scale flow characteristics. For LES simulations conducted within this study, the adequate time scale has been defined as a multiple of the Kolmogorov scale, η^{-1} (Kolmogorov, 1942).

$$\eta_k \approx \left(\frac{\nu l_t}{u'^3}\right)^{0.5} \tag{2.23}$$

For the case contained within Chapter 3, assuming a value for viscosity of 0.2 cm^2/s for air due to the gas/gas jet nature of the problem and a value of 120 cm/s for the fluctuating velocity component to give:

$$\eta_k = \frac{0.2(0.230)^{0.5}}{120^3} = 8.3 \times 10^{-4} \text{ s} \tag{2.24}$$

The total physical time for the simulation to run is determined from the turbulent length scale and the velocity of the problem. It should also be of sufficient length to prevent the instantaneous time samples from being measured directly after one another. Calculating this integral time scale as an example:

$$\eta_i = \frac{l_t}{u'} = \frac{6}{120} = 0.05 \text{ s} \tag{2.25}$$

Ideally the simulation total time should be run over a multiple of this time period in order to adequately average the large-scale flow components. The LES average filtered velocity is obtained by integrating each filtered velocity data set, itself a product of time, over a suitably defined time period Δt .

$$\bar{u}(x,t)_{\Delta t} = \frac{1}{\Delta t}\int_{t-\Delta t}^{t+\Delta t}(u(x,t))dt \tag{2.26}$$

Unlike the assumption used in RANS, where the RMS velocity values are dictated by the square root of the turbulent kinetic energy, LES can produce results for all three Cartesian components without the issue in dealing with Eq. (2.18). This is accomplished by the summation of the difference between the instantaneous velocity and the average velocity. The number of data samples used to calculate the average velocity has an effect here, unless the number of samples across the run-time is sufficient then there may be too great a difference between the instant and average velocities which may lead to very high RMS values suggesting that the flow may not have been adequately resolved under this time period.

$$u'^2(x,t) = \frac{1}{N}\sum(u(x_t,t_i) - \bar{u}(x_t))^2 \tag{2.27}$$

The RMS stress components for LES can be calculated from the root of the filtered velocity components e.g. Eq.(2.27). In addition to this, there are sub-grid scale stresses produced which are not calculated from the RMS values; such as $(u'_x u'_y)$.

Finally, there is the integral time scale. This can measure the scale within specific regions of the flow to examine the differing effects of the changing flow pattern depending upon the velocity. To accomplish this the difference between two instantaneous velocities separated by a suitably large time period, τ ,against the average velocity. To determine the effect of the time-scale upon the average velocity components, correlation between points within the domain over time is defined as:

$$R(\tau) = \frac{1}{u'^2(x_t)}\sum(u(x_\alpha,t_i) - \bar{u}(x_\alpha))(u(x_\alpha,t_{i+\tau}) - \bar{u}(x_\alpha)) \tag{2.28}$$

Considering the turbulent nature of the flow, it is probable that the integral turbulence time scale may change drastically over the total run-time of the simulation. For example, in a vortex there will be regions of both positive and negative velocities accounting for recirculation. As a result, flow statistics should be obtained over multiple time-scales to provide sufficient data to calculate the averaged quantities.

Other Approaches

In addition to the basic RANS and LES approaches, there are a number of alternative approaches which utilise these methods either in alternate form or as part of a combined approach. One such approach is found in Gopalan et al. (2013) where the computational grid is sectioned and switches between the RANS and LES approaches with a defined interface between the two, which was found to improve LES accuracy on coarse grids and increase computational efficiency, but

with many variations upon this approach - further clarification upon the best approach was needed. Abe (2014) address one of these aspects with respect to the switching parameter used to change methods close to the wall, which is dependent upon the computational grid size and the scale of the turbulence; establishing that LES should be chosen providing the grid resolution is high enough. This factors into the continuing goal of CFD approaches to both reduce computational cost and improve accuracy (Abe, 2014). An example of coupling an existing RANS approach to an LES method is covered in Temmerman et al. (2005).

Another approach coming into use is that of Very Large Eddy Simulation (VLES), reviewed in Argyropoulos and Markatos (2015), whose purpose is to improve upon RANS predictions using an unsteady LES format but with a greater portion of the small-scale turbulence being modelled in order to decrease grid requirements and speed up computation time.

DNS or direct numerical simulation is the most accurate and most costly approach to CFD as the grid resolution must be sufficient to capture all scales of turbulence and directly resolve the problem without any modelling. This approach is frequently limited by available resources requirements which are significantly higher than any other approach, but is by far the most accurate (Argyropoulos and Markatos, 2015).

2.1.3 Discretization

In order to be solved numerically, equations used in all RANS and LES approaches must be discretized for use on a computational mesh grid. These frequently take the form of Partial Differential Equations or PDE's in a matrix format.

Anderson et al. (1984) describes this process where variables in a continuous problem are assigned to discrete points and the differences result in a partial differential equation.

Each term is calculated at a further node away from the starting point at an increased time step, this value is then iterated for all surrounding areas using the newly calculated value (Roache, 1998). When discretizing a problem, there are a number of errors which can arise from the solving process. Anderson et al. (1984) covers several of these in detail, noting that the limitations of computing may

reduce the accuracy of the solution when dealing with a high number of decimal places as the solution may be rounded off. Discretization error is described in Anderson et al. (1984) as the error in equation solutions due to the difference between a discrete and continuous problem.

Grid independence is a crucial factor in the running of a successful CFD simulation. This refers to a scenario where the values for a calculated field do not change with an increase or reduction in individual cell size within the computational mesh.

Kodavasal et al. (2015) compares multiple grid cell sizes for an IC engine cylinder simulation ranging between 0.1 - 0.7 mm, noting both the effects on grid results along with the increase in computation time. Resulting in an end value of 0.175 mm minimum cell size to balance computation cost and accuracy for utilising the same grid for both RANS and LES methods, noting that significant differences were obtained for a cell size of 0.7 mm.

In addition, Xue et al. (2013) covers cell sizing when utilising an Eulerian-Lagrangian method for fuel spray modelling. Noting that RANS-based models were capable of producing good results from a 0.25 mm based grid, this was insufficient for LES to capture the spray characteristics and required a resolution of 0.0625 mm or better to predict accurate liquid penetration whilst vapour penetration required further refinement for RANS.

A study in Bianchi et al. (2001), modelling high pressure diesel sprays carried out a comprehensive review of the effect of grid resolution on several key spray quantities including the SMD, turbulent kinetic energy and spray structure. Using an established droplet breakup and atomization model, the results presented a high change in the spray prediction pattern, altering the jet penetration length and also noting that there was little change in the SMD. This suggested that the grid independence was most critical for determining the spray shape, particularly in high pressure condition. However it notes that an over-prediction of momentum exchange between phases may occur close to the nozzle orifice when using a Lagrangian-Eulerian approach (Bianchi et al., 2001). Two of the frequently used algorithms in CFD are:

PISO

Pressure-Implicit Split Operator (PISO). A method using multiple correction stages after an initial prediction for solving the time dependent Navier-Stokes equations in incompressible and compressible forms (Anderson et al., 1984). The equation variables for pressure, velocity and density are resolved to account for mass conservation throughout the system to satisfy the continuity equations over a number of steps.

The capability of PISO with multiple correction steps to satisfy the continuity equations makes it suitable for use with both RANS and LES methods, depending upon the type of filtered Navier-Stokes equations used. Correcting for the velocity repeatedly solving for pressure over multiple steps reduces the level of error in the field when run over multiple iterations (Anderson et al., 1984).

SIMPLE

SIMPLE: Standing for 'Semi-Implicit Methods Pressure-Linked Equations', this approach is described in Anderson et al. (1984) as a cyclic procedure based upon multiple iterative correction steps to solve the RANS equations. This approach is not suitable for non-steady state problems.

Another point of note is the differences between CFD solvers, despite the implementation of identical model. One such example is detailed in Karrholm et al. (2008). A case was conducted for the simulation of a 3D injected diesel spray using identical models and setup on two different CFD codes. Differences between the predictions note that there is a change in flame shapes, auto-ignition locations and lift-off predictions, this suggests that depending upon the software used for modelling, there may be key differences in the results data. A concise summary of the implementation of turbulence quantities into object-orientated programming can be found in Weller et al. (1998).

Wall Functions and y^+

In order to successfully model behaviour close to a domain wall, within a flows boundary layer where the equations used for free-stream flow calculation may not

be applicable due to friction, there are a number of options available depending upon the type of CFD simulation being conducted.

RANS models typically utilise wall functions, which are special boundary conditions which are used to predict the flow properties close to the wall. Application of these wall functions is to the first layer of cells on the face of the boundary, the influence on the main flow is dependent upon the size of this cell which can be evaluated by a quantity defined as y^+. For most the most accuracy this value should be as close to unity as possible to ensure the effect of the wall function outside of the cell layer is minimal, however it is also important to include an adequate number of cells to accurately model the jet boundary layer. In reality, a small y^+ can be sufficient provided the flow is not wall bound in order to balance accuracy against computational resources. Launder and Spalding (1972) gives one method for approximate calculation of y^+ as:

$$y^+ = y\frac{\sqrt{(\tau_s \rho)}}{\mu} \tag{2.29}$$

LES requires an even finer grid at the walls in order to capture small-scale flow features from the SGS model, however it is a commonly noted issue that LES has difficulty with near-wall behaviour - hence the ever-increasing application of hybrid methods to improve wall modelling whilst retaining the accuracy of an LES prediction outside of the boundary layers.

2.2 Jets in Cross Flow

2.2.1 Phenomena

The jet in cross flow consists of a a secondary jet, normal to a free-stream air flow at a 90 angle, meaning that this secondary flow will interact with the primary jet, causing a level of deflection proportional to the characteristics of the cross-flow including its velocity and density. The jet momentum ratio , q, is defined in Eq. (2.30) where 'a' refers to the cross flow air and 'j' to the jet properties.

$$q = \frac{\rho_j u_j^2}{\rho_a u_a^2} \tag{2.30}$$

Andreopoulos and Rodi (1984) identify from experiments that there are several key features which form regardless of the velocity ratio, including a very complex flow region immediately in front of the jet inlet which contains reverse flow and recirculation, close the domain floor. The second is formation of the counter-rotating vortex pair at the front of the jet, caused by the vorticity generated by the turbulent region, however this decays in the far downstream region due to the reduction in turbulent stress and energy (Andreopoulos and Rodi, 1984).

A comprehensive review of the basic jet structures for a single phase flow can be found in Karagozain (2010) where it is noted that the jet to cross-flow velocity ratio is responsible for the overall jet behaviour including the level of penetration into the cross-flow and the formation of the recirculation area.

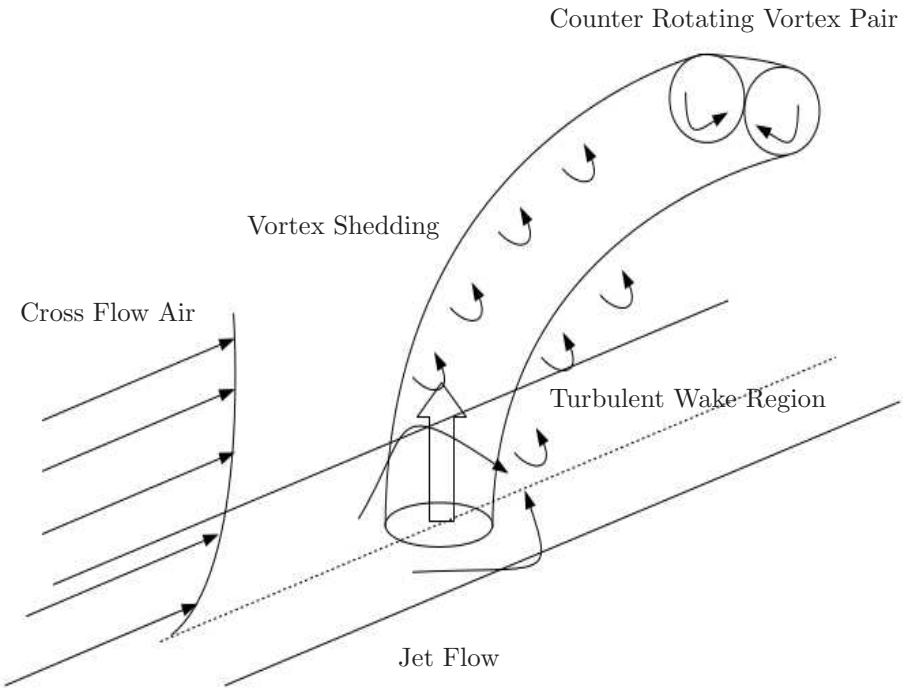

Figure 2.2: Typical aerodynamic structures of a jet in cross flow (after Kelso et al. (1996)).

Experiments conducted in Kelso et al. (1996) also identify the main aerodynamic structures of the flow, visible in Figure 2.2. Describing the Counter-rotating vortex pair (CRVP) as a global feature present in the far flow field, the study confirms that this phenomenon is an integral part of a jet in cross-flow and should be present in simulation predictions. Along with this is the presence of horseshoe vortices around the jet, suggesting these unsteady phenomena form from the wake of the jet (Kelso et al., 1996). As with Andreopoulos and Rodi (1984), it is noted that these features are prominent in flows consisting of high velocity ratios and Reynolds numbers. Supporting these statements are observations from Morton and Ibbetson (1996), who define a series of features associated with vortices in the flow field:

- A number of upstream ring vortices surrounding the jet shear layer.
- A Counter Rotating Vortex Pair.
- A turbulent wake in the jet-wise flow direction.
- Horseshoe vortices.

All these phenomena as observed in the experiments are validated in multiple texts examined throughout this chapter, confirming that each of these important features should be expected when performing a CFD simulation for a jet in cross flow.

2.2.2 Modelling of Single Phase Flow

Investigating the nature of a round jet in cross flow, Kim and Benson (1992), noted that there is a considerable effect in the downstream region from the interaction between cross-flow and jet closer to the injector, surmising that the downstream region of the flow needs a high grid resolution in order to fully capture the turbulence characteristics along with the region around the jet inlet.

Another key point was that the peak of the turbulent kinetic energy is located where the tangential velocity is at a minimum and the energy concentration closely represents the turbulence profiles (Kim and Benson, 1992).

Karagozain (2010) focuses on the importance of the vortex pair as the most dominant flow feature, whose formation location and size can influence the level of mixing between the jet and the cross-flow; also noting that the type of smaller vortexes which influence the flow structure differ when increasing the velocity ratio. Visual confirmation of jet deflection can be found in Karagozain (2010), illustrating both the deflected jet along with multiple breakup regimes.

Majander and Siikonen (2006) presents an LES study compared to the experimental data from Crabb et al. (1981) within a region close to the jet inlet using a Smagorinsky SGS closure with a variety of jet flow boundary conditions formed from a fully developed turbulent pipe flow. LES was found to present a good match to the jet penetration, predicting the evolution of the counter rotating vortex pair along with vortices within the shear layer. However the effect of inlet boundary conditions upon the turbulence close to the inlet and cell density close to the wall was noted, with a suggestion that a hybrid RANS-LES may be used for improved close-wall modelling.

Ivanova et al. (2012) evaluates a turbulent gas jet in cross-flow using both LES and RANS methods in an effort to compare the prediction accuracies. As with previous results in the subject, it was shown that issues with the RANS approach for such a scenario remain in the calculation of the velocity magnitude peak values. With the application of a modified k-ω–SST, improvements were made over the standard version due to the limit placed upon the shear stress magnitude (Ivanova et al., 2012). LES predictions for the flow and normal stresses proved superior to their RANS counterparts, with an additional evaluation of the turbulent Schmidt number, used for closure in turbulence models, concluding that a value of 0.5 or more is most appropriate to predict the high turbulence levels (Ivanova et al., 2012).

A study by Desantes et al. (2006) evaluated the deflection changes for gas jets over a range of injection velocities and obtained results consistent with expected jet in cross-flow structure with the corresponding increase in either cross-flow or jet velocity will affect the jet shape due to the varying influence of the aerodynamic drag. Also noted was the increase in jet diameter would reduce the level of deflection, however it is the variation in density which has the greatest effect (Desantes et al., 2006).

Galeazzo et al. (2010) performed a series of experiments and equivalent CFD comparisons using both RANS and LES to predict a jet in cross-flow scenario and evaluate the computational predictions when compared to experimental data. It was found that although there was a substantial difference between the two RANS models used, k-ε and k-ω-SST, despite the identical grid and setup conditions both average velocity peaks and troughs were under-predicted by k-ε; with both performing poorer than the LES predictions. This trend continued onto the predicted stresses where the increased turbulence predictions of the LES method result in a better match to the experimental data. (Galeazzo et al., 2010)

A range of RANS approaches including URANS, k-ω-SST and SST-SAS are presented in Ivanova et al. (2010), with findings showing that conventional RANS over-predicted the minimum peak velocity downstream from the inlet whilst the unsteady predictions of the URANS and SAS approaches allowed for improved turbulence modelling; it was concluded that URANS was the best overall approach out of this selection for modelling a jet in cross flow.

Boundary Layer

When a fluid flow moves parallel to a solid wall, the free-stream behaviour at the edge is altered due to the interaction with the boundary resulting in a change in structure as the velocity tends toward zero. This is known as the boundary layer and differs in behaviour and structure depending upon the type of flow in question. The boundary layer formed varies in height depending upon the flow velocity and continues until the flow is outside the influence of the wall effects, where it is assumed that the velocity is almost equal to the bulk velocity magnitude. Since this boundary layer largely affects wall-bounded flows, features prominent within the main stream far from this region are not applicable but this region must be accounted for; particularly within highly turbulent flows.

2.3 Breakup of Liquid Jets

The purpose of the atomization of a liquid jet is to form a spray, which can be used for multiple purposes; but most importantly increasing the available surface area

of the liquid. Lefebvre (1989) defines a liquid spray as a droplet system within ability continuous gas phase; noting that key quantities for the description of a spray include the mean droplet size and its corresponding size distribution.

The Weber number of a particular flow is a measure of the fluids inertia compared to its surface tension (Massey and Ward-Smith, 2006). The surface tension of a liquid is a property which represents its resistance to deformation by shear and can have a significant effect upon spray properties. A higher Weber number means a liquid far more prone to the various breakup effects and would correspondingly decrease the diameter of the droplets formed but increase their number. An overview of such effects is addressed in Desjardins and Pitsch (2010), with the formula given as:

$$We = \frac{\rho u^2 l}{\eta} \tag{2.31}$$

For very turbulent cases, which make up the majority of the work studied and performed within this text, the Weber number is expected to be very large along with the Reynolds number. This allows a number of assumptions to be made regarding the effects which the flow will experience, including the omission of laminar viscosity effects upon the liquid/gas interface, (Luret et al., 2010), and the increase of small-scale turbulence effects on droplet breakup due to the deformation of the gas/liquid interface (Desjardins and Pitsch, 2010). These effects are also commonly correlated with an observation of the type of breakup mechanism associated with the liquid, with the shear breakup mechanism dominant at higher Weber numbers (Lubarsky et al., 2010). An example of jet breakup can be found in (Rana and Herrmann, 2011).

In order to adequately describe a spray, multiple different diameters have been suggested, with one of the most commonly used as the Sauter Mean Diameter or D_{32} . This parameter produces a droplet diameter where the ratio of the droplet volume to surface area is equal to that of the entire spray (Lefebvre, 1989). In particular SMD has been noted to predict the quality of the atomization process, pertinent to cases involving combustion or vaporization. Williams (1989) notes that few atomisers produce a series of droplets of a single size and instead produce a spray which contains a variety of different droplet sizes.

2.3.1 Atomization

A liquid spray can be defined as a continuous gas phase containing a droplet system (Lefebvre, 1989). Noting that key quantities for the description of a spray include the mean droplet size and its corresponding size distribution.

Frequently atomisers are used in order to break up a liquid to form a spray. Lefebvre (1989) presents an overview of multiple different types of atomisers, depending upon the type of spray required. One of the more common types used include plain jet, where a liquid at pressure is passed through a narrow diameter into a gas. Depending upon the atomiser design, swirl in the flow may be induced before the liquid is passed through the exit of the injector into the domain. The atomiser type plays an important role in determining the boundary conditions used when simulating a liquid jet flow in CFD as it will affect the type of spray formed and the breakup mechanisms employed.

A comprehensive review of the liquid jet atomization process is covered in Lightfoot (2009). The phenomena of primary interest to a injection scenario for a jet in cross-flow are listed within this text as:

- Column breakup, the single jet column breaks into droplets on a scale similar to that of the original jet width. Occurs as result of large-scale fluctuations within the liquid.

- Bag breakup, where the stretched jet breaks up into multiple large components, or ligaments, downstream as a result of rupturing.

- Multi-mode, induced as there is not an instantaneous transition between one type of breakup to another, remaining that multiple different breakup types may occur within the same area, one particular case stated as a combination of bag and shear breakup (Lightfoot, 2009).

- Surface breakup, when liquid is sheared from a surface through aerodynamic forces while the centre of the ligament remains intact. The high range of droplet magnitudes produced by a jet breakup is a result of the combination of these various breakup regimes dependant upon the size and interaction of the jet width the cross-flow.

Primary atomization is used to describe the breakup processes which occur close to the liquid inlets where the scales of the droplets formed remain large and typically consists of the column and bag/multi breakup regimes with surface defined as secondary breakup due to the domination of the single breakup mechanism and significant reduction in scales from that of the primary region.

Beginning at the liquid jet inlet, the process by which the jet breaks up through various regimes in order beginning at the inlet is summarised in Lightfoot (2009) as column, followed by a combination of column and surface before moving to bag, multimode and finally shear (Lightfoot, 2009).

A similar study on the formation of droplets and jet breakup is presented in Lin and Reitz (1998) which presents visual confirmation and classifies the varying types of breakup regime into either first (primary) or secondary breakup regimes, dependent upon the size of the drop or ligament form. The Column breakup, as described in Lightfoot (2009) and Lin and Reitz (1998), is classified as Rayleigh breakup which can occur several diameters downstream of the nozzle. The bag breakup producing large diameter drops is classified as primary atomization with the surface breakup producing extremely small droplets being classed as secondary breakup (Lin and Reitz, 1998).

Experiments conducted in Birouk et al. (2007) examined the effect of viscosity in low velocity cross-flow liquid jet. Although studied for a low-velocity cross flow it was found that an increase in liquid viscosity did increase the jet penetration into the free-stream. This is in line with expected behaviour as an increase in viscosity would affect the resistance of the liquid surface to the effects of the aerodynamic shear caused by the interaction with the cross-flow.

Additional experiments conducted in Sankarakrishnan et al. (2005), cover experiments examining the effects of turbulence on jet breakup. Multiple liquid jets are visible with an increasing Reynolds number causing less deflection, despite the retention of a critical Weber number. The breakup regimes also alter, with the highest Reynolds flow exhibiting only surface breakup as opposed to a combination of regimes, previously mentioned in (Lightfoot, 2009).

An experimental study conducted for deflected liquid kerosene jets by (Ragucci et al., 2007) examined the effects of temperature and pressure conditions on atomization and SMD. Their conclusions drew a number of important point such as

the observation that SMD and atomization were largely affected by the momentum ratio between the jet and surrounding there with only a weak dependence upon the Weber number. A second important observation was noted regarding the possible correction required to the near-wall behaviour of the jet along the free-stream velocity at low temperatures as the breakup may be affected. (Ragucci et al., 2007). Such behaviour may be necessary to examine during the use of liquid modelling when considering a complex jet in cross-flow scenario with a high velocity free-stream flow.

Experiments conducted by Bai et al. (2009) used a water jet in a cross-flow and measured multiple injection angles under the assumption that a change may make the jet structure more complex due to increasing wall effects and turbulence. A reduction in angle was found to shift the location of the vortex pair and alter the dispersion of smaller droplets, resulting in a low gradient profile for the average SMD upstream. Although these experiments did not account for heat transfer within the system it covers the effect of an increasing cross-flow velocity shifting the location of the vortex pair downstream along with a decrease in size and their effect upon mixing and droplet distribution.

Focusing on the effect of low Weber number flows, Zheng and Marshall (2011) showed that for a value of less than 800, all liquid water jets exhibited column followed by 'bag' breakup modes, with the transition between the two mechanisms a result of increasing momentum ratio, which also increased the jet penetration. In contrast a higher gas Weber number increased the deflection whereas the change in breakup regimes from column to bag led to a reduction in the SMD droplet magnitude.

Secondary atomization occurs away from the liquid inlet and occurs on a scale much smaller than those mechanisms found in primary atomization, typically turbulence and instabilities causes liquid to be sheared off the surface of already small ligaments and droplets. The breakup of droplets in the downstream region is noted in Bayvel and Orzechowski (1993), where the aerodynamic forces exceed the surface tension forces and disintegration occurs.

Additional examination of the effect of the Weber number in Stenzler et al. (1990), a number of observations were made relating the jet penetration to the

Weber number, resulting in a conclusion which stated that an increasing Weber number reduced the average droplet size and thereby the total penetration. (Stenzler et al., 1990) This is consistent with the breakup regimes described earlier, with the surface breakup mechanism dominating the primary zone at high velocities. In relation to the study on viscosity by Birouk et al. (2007), (Stenzler et al., 1990) concludes that a large increase in jet viscosity caused a reduction in the level of jet penetration, causing a greater level of streamwise deflection.

Within gas turbines, high pressure fuel systems are frequently used which form a liquid spray of fine droplets (Cohen et al., 1996). Since a wide variety of designs are in use, this highlights the importance of the atomiser type and breakup mechanisms required when attempting CFD modelling. Lefebvre (1983) supports the importance of these requirements stating that without atomization to increase the available surface area, fuels in their normal state are not suitable for combustion due to the lack of vapour produced.

2.3.2 Vaporization

The process of vaporization is one where a liquid is heated beyond the fluids boiling point, at which time the liquid evaporates and is transferred to a gaseous state. Multiple processes can be responsible for evaporation, making modelling a complex issue due to the many factors involved. These can include the application to a gas turbine environment. Cohen et al. (1996) describes the involved processes including mixing between the fuel and air, vaporization, chemical reactions and molecular breakdown.

A liquids vapour pressure is that exerted by vapour above the liquid surface; a high value enables rapid fuel evaporation and is important to Combustion (Lefebvre, 1983).

The applied vapour pressure equation relates the pressure to the temperature between the vapour and liquid, and is used in modified form as the Antoine equation. Originally refined from the Clausius Clayperon relation, detailed in Reid et al. (1987), this term was found to over-predict when applied below the fluids boiling temperature. Modifications produced the Antoine equation. This new equation was found to improve predictions, but still only functioned in a narrow

temperature and pressure range; a concern when applied to a gas turbine environment traditionally consisting of high pressures and temperatures as detailed in Lefebvre (1983) and Cohen et al. (1996).

One early model for the vaporization of liquid droplet into a high temperature gas is presented in Abramzon and Sirignano (1989), detailing a proposed method for simplifying the vaporization process for liquid droplet applicable to spray combustion calculations. They surmise that changes in the thermophysical properties of the droplet including the specific heat and internal temperature profiles and heating within the droplet are an important consideration when retaining two separate phases, gas and droplet with interchange terms between them. Statements of particular relevance note of the importance of the internal heat transfer within a droplet are of particular importance (Abramzon and Sirignano, 1989).

Aggarwal and Peng (1995) presents a review of various approaches to model the dynamics of droplets and predict their vaporization, noting in particular that for a two-phase flow the difference in parameters between fluids can have an effect upon the aerodynamic forces exerted on the liquid droplets; affecting their structure along with other properties including drag. Most of the basic approaches to vaporization rely on the d^2 law of droplet size, which assumes that the diameter decreases at this rate with respect to time (Aggarwal and Peng, 1995).

Additional evaluations of vaporization in Sirignano (1983) also comment on the change in temperature gradient affecting the droplet surface tension, but regards the effect of this in comparison to other phenomena as small. The aspect of heat transfer from a hot gas to a cold liquid transfers some energy to the droplet interior once the latent heat of vaporization is overcome, with the internal temperature gradient gradually becoming uniform whereas that on the surface may approach the liquid boiling point depending upon the conditions outside the droplets (Sirignano, 1983). However this is not valid when given an assumption of short residence time in regions of high vaporization; one of the assumptions used with the Another important point made within this study regards the relationship for mass transfer between liquid and vapour, $ln(1 + B)$, where B is the Spalding mass transfer number, may be accurate for any unsteady environment as this relationship may be very high for a large Reynolds number flow whereas

this assumption predicts only a small variation even with a large increase in the magnitude of B (Sirignano, 1983).

2.4 Modelling of Two Phase Flows

When considering a gas/liquid setup, each separate fluid must be modelled through its own series of transport equations, taking into account factors such as the change in density, behaviour applicable to only one phase e.g. coalescence. The density between different phases is also an important factor and many transfer functions must be introduced in order to successfully model an interactions (Kleinstreuer, 2003). Normally each separate component is defined using its own set of transport equations solved through the local properties with additional terms accounting for the shear and heat/mass transfer between the separate components. The phase can also differ along with the material properties.

When considering particle modelling, there are two distinct approaches which can be applied to the problem. The first is the use of an Eulerian method - which calculates average quantities for a concentration of particles within a system, governed by the solving of transport equations. (Nerisson et al., 2011). Although more computationally efficient than Lagrangian methods, it cannot predict the properties of individual particles.

The second is to utilise a Lagrangian method which predicts the individual characteristics of every droplet rather than the averaged properties of a concentration. This requires a larger amount of computational resources than an Eulerian method, especially when dealing with a large number of particles - such as the breakup of a dense liquid surface.

2.4.1 Eulerian–Lagrangian

Each approach can be applied to both RANS and LES methods, Liu and Novoselac (2014) compares Lagrangian particle modelling coupled with RANS $k-\varepsilon$ and LES Smagorinsky approaches for indoor particle modelling, concluding that the LES paired with Lagrangian approach provides superior predictions in unstable flows areas for particle dispersion, however both approaches present good agreement

for concentrations far from the inlet region. However, only buoyancy and mixed ventilation particle distribution are considered and neither approach is exposed to high velocity gradients.

A similar study on particle dispersion, presented in Zhao et al. (2008), compares accuracy of multiple Eulerian models to the Lagrangian approach for very low speed particle dispersion, noting that the Lagrangian approach predicted greater accuracy with respect to particle concentration over the Eulerian models, the results for the deposition velocity were poor when stronger turbulence conditions were applied; suggesting that appropriate model selection when considering the turbulence intensity is extremely important.

Galeazzo et al. (2013) contains a number of simulations using a variety of modelling methods including URANS and LES to predict liquid phenomena close to an injector. A fine grid of 10 million elements over a small area predicted that although all methods showed a reasonable match regarding peak velocity regions compared to experimental data it was LES which was the most accurate whilst the successively reduced capability of URANS and RANS to predict turbulent structures led to consecutively worse predictions. The Schmidt number selection for RANS was also noted to have an effect on the steady-state solution.

Many investigations into the behaviour of liquid jets in crossflow have been conducted in recent years. Herrmann (2009) investigated the predictions of a Direct Numerical Simulation, coupled with Lagrangian particle tracking, on jet predictions.

This was followed up with Herrmann (2011) which expanded upon this simulation with an analysis of the density ratio. It was concluded that increasing the density ratio reduces jet bending and transverse spread with increasing liquid penetration (Herrmann et al., 2010). This was applicable in the primary atomization zone of the spray near the nozzle. This is an important note when considering a jet in cross-flow as the breakup can be affected by the change in cross-flow conditions, as either a result of pressure, velocity or density changes from either the free-stream or the liquid.

One such approach to calculating liquid jet atomization without using a column breakup model is detailed in Oda et al. (1994). These simulations were performed by specifying a droplet distribution at the injector and calculating

their trajectory and breakup. Results reported several important liquid breakup phenomena, in particular was the high decrease in SMD diameter for the droplets near the injector for a high free-stream velocity with a lower value merely causing the drops to be transported rather than broken up (Oda et al., 1994).

Application of liquid jet model to a combustion scenario also requires additional consideration of crucial parameters, including the droplet sizes produced from the atomization process and their mixing with the surrounding air; both of which can affect performance (Williams, 1989).

Recently, two-phase flow has been increasingly applied to LES CFD methods in an attempt to improve turbulence predictions due to the known issues with RANS. Xue et al. (2013) notes that although use of LES two phase is increasing there is still much in the way if development remaining, particularly with the SGS modelling in order to account for the more complex physics and grid refinements required for sprays.

Navarro-Martinez (2014) describes a novel method using an LES–PDF approach with Eulerian stochastic fields to predict spray atomization without the use of a Lagrangian approach. This solves an SGS-PDF for liquid surface and volume with a stochastic method and can account for SGS liquid structures in dilute and dense regions of the spray. Injecting a liquid spray into stationary air, the surface density (Σ) is shown to be extremely sensitive to the boundary and initial conditions, and can scale differently depending upon the spray region. The model was shown to be able to reproduce the surface density and liquid dispersion DNS results in its preliminary predictions and noted that SGS modelling was important in obtaining accurate results, particularly when considering the small scales involved in the secondary breakup regions.

Banerjee and Rutland (2015) presents a study on the importance of grid resolution when considering Eulerian/Lagrangian methods for use with LES and non-eddy viscosity model. RANS applications in this study suggested that the mixing is entirely the result of dissipation with LES also considering the effect of turbulent structure breakup scales. In addition, an efficient cell size for LES to capture the important flow features was determined as approximately 0.5mm to best capture the jet penetration and spray formation. It concludes noting that

small scale turbulence structures can affect the jet breakup in the secondary atomization region for spray induced flows, it is the large scale phenomena which primarily govern the liquid transport.

Another variation upon a liquid vaporization model is the coupling of an Eulerian framework with Lagrangian particle tracking. There are numerous examples of this coupling including Lebas et al. (2005) and Balasubramanyam and Chen (2008). These results highlighted several important aspects when dealing with a very high speed (supersonic) cross flow with evaporation. This includes the strong dependence on aero-thermal interaction between the liquid jet and cross-flow, the impact on droplet magnitude depending upon the variant of atomization model used and the importance of well-modelled gas flow dynamics to the predictions (Balasubramanyam and Chen, 2008).

An additional study documenting the application of a joint Eulerian–Lagrangian method to a liquid jet injection scenario was presented by (Ning et al., 2007) and (Ning et al., 2007). This implementation of a vapour model was successful in predicting liquid jet evaporation for a injection flow, citing the need for examination of the turbulent closure, obtained by gradient diffusion, used in order to improve liquid dispersion. Further evaporation predictions using DNS with regards to establishing the effect of turbulence on a spray are presented in Reveillon and Demoulin (2007).

More recent studies utilising DNS to improve primary breakup predictions with an ELSA approach close to the injector are presented in Duret et al. (2013) and Demoulin et al. (2013). The effect of DNS predictions against the Σ predictions accounted for only by turbulent phenomena as a function of the equilibrium Weber number was shown to have relatively good agreement for the interface density, noting that an equilibrium state was difficult to achieve for DNS due to time evolution (Duret et al., 2013). Demoulin et al. (2013) presented an approach also using DNS spray data against an LES ELSA implementation similar to that in Chesnel et al. (2011) for a normal injection. The issue regarding grid resolution upon minimum flow scales for LES was highlighted with additional context upon the energy between the resolved and modelled sections of the flow (Demoulin et al., 2013). This study also presented a good match with DNS close

to the injector, showing that the use of DNS to evaluate modelling approaches may see further use in the future.

Jones and Lettieri (2010) focuses on an LES simulation for the atomization of a liquid diesel spray into stationary air and cross flows using stochastic modelling for the droplet breakup, this applies the subgrid scale motions to the secondary breakup of the liquid droplets. Simulating diesel injection into stationary air for an atomization only scenario yields a good match to experimental data including the level of spray penetration. Application to a cross flow for multiple breakup regimes including bag and stretching/thinning with an increasing Weber number continued to present a good global match for the droplet size and distribution with the model being able to adapt to the Weber number. All cross flow cases used a roughly uniform droplet distribution at the liquid inlet and required the Lagrangian approach to account for individual particles. Small differences in the SMD distributions were accounted for by noting that the inclusion of evaporation or combustion would lead to a reduction with the droplet sizes. In addition, it was noted that the drag law simplification used could also account for some discrepancies, but concludes the model was capable of application to more complex geometries.

2.4.2 Gas Turbine Applications

Boileau et al. (2008) highlights a different concept to the Eulerian–Lagrangian approach by evaluating the performance of an LES Eulerian–Eulerian approach where the carrier (gas) and dispersed (liquid) phases are both calculated using an Eulerian framework with the separate equations for gas and liquid transport linked by coupling terms for heat and mass transfer. Unlike the Σ–Y_{liq} model covered in the following section the two phases are still separated with the conservation equations for dispersed and gas phases being of identical form. Multiple test cases including a laminar flame and turbulent dispersion in a swirl flow with co-axial injection both produced good agreement to experimental data regarding mean quantities, although RMS values for the swirl flow were shown to be underpredicted due to not accounting for particle random uncorrelated motion. The mass transfer for evaporating liquid is handled via a Spalding approach, similar to

that used within the Σ–Y_{liq} model, see Section 2.4.3. Application to a 3D aircraft combustion chamber with an injected monodisperse spray of droplets of 15 μm successfully predicted the formation of a turbulent flame from a two-phase flow; forming a central recirculation zone which influences evaporation and stabilises the hot gases. This result showed that an Eulerian–Eulerian method is a feasible approach for predicting two-phase combustion but can be influenced by the gas phase predictions.

Riber et al. (2009) follows this study by comparing Eulerian–Lagrangian predictions directly to those from an Eulerian–Eulerian method for a non-reacting, non-evaporating flow for a bluff body; reminiscent of the configuration of a reacting two-phase combustion chamber which is applicable to aeronautical applications. Initial evaluation of gas phase only predictions highlighted the impact of the selected numerical scheme which affected the predicted location of the recirculation zones; which in turn can influence the flame shape. In addition, the inlet boundary conditions were found to require velocity fluctuations to better predict the velocity around the inlet. Introducing monodisperse particles of 60 μm with co-axial injection showed that both Eulerian–Lagtangian and Eulerian–Eulerian methods predicted similar mean quantities and particle number densities within the stagnation regions. Under-prediction in the RMS values along with slightly reduced downstream presence was predicted for the Eulerian–Eulerian results, caused by the lack of random motion also highlighted in Boileau et al. (2008) and sensitivity to velocity inlet conditions respectively. This study concluded that the gas phase predictions heavily influenced the dispersed phase predictions and that both approaches captured the major flow features, showing that Eulerian only methods are viable for LES predictions.

An example of application to be complex geometries can be found in Jones et al. (2012), which applies the stochastic model described in Jones and Lettieri (2010) to a swirl-stabilized burner using a similar injection of monodisperse droplets but including evaporation along with droplet breakup. The grid sizing was found to have little effect upon the gas phase flow structure, provided the resolution was sufficient to capture the large turbulence scales. However the fragmentation of the droplets was found to be influenced by conditions within and

close to the atomizer. The global velocity profiles along with the SMD distribution and magnitude presented a good match to the experimental data, with the small difference in RMS values accounted for due to the use of the standard Smagorinsky SGS model. However the importance of correctly establishing the flow features was highlighted with the vortex core near the atomizer shown to have a significant effect upon the droplet distribution, which in turn affects the vaporization rate.

Pope (1994) presents a general overview of Lagrangian pdf methods along with an introduction to Eulerian pdf's, which refer to the statistical concept of fluid particles. An application of implementing LES with a pdf (probability density function) model designed to predict combustion characteristics in a gas turbine was presented in Sadasivuni et al. (2012). These results show that the flow predictions made, used with the dynamic Smagorinsky SGS model were capable of predicting the flame characteristics despite the elevated pressure and complex flow field.

2.4.3 The Σ–Y_{liq} Model

The Σ–Y_{liq} model for liquid jet prediction, outlined in Vallet et al. (2001) has been refined by multiple groups and presented in Lebas et al. (2005), Luret et al. (2010), Sidhu and Burluka (2008) and Beheshti et al. (2005) to include the such additions as vaporization and application from the original RANS form through to LES (Chesnel et al., 2011) and DNS (Demoulin et al., 2013). Applications of this model have ranged from engine modelling for diesel injection to pesticide atomization (De Luca et al., 2009).

The original purpose of the model was to provide a simplified method for predicting the atomization of a liquid spray from first principles, without the application of a pre-defined spray pattern. Unlike a typical two-phase approach the system is defined as a single continuum without assigning separate phases for liquid and gas. This continuum is defined using an average density, consisting of three different components, fuel in liquid form, fuel in vapour form and the remaining air component:

$$\bar{\rho} = \left[\frac{\tilde{Y}_{\text{liq}}}{\rho_{\text{liq}}} + \frac{\tilde{Y}_{\text{vap}}}{\rho_{\text{vap}}} + \frac{1 - \tilde{Y}_{\text{liq}} - \tilde{Y}_{\text{vap}}}{\rho_{\text{gas}}} \right]^{-1} \tag{2.32}$$

To calculate the mass fractions of the fuel in liquid and vapour form two Favre averaged transport equations are used, Eq. (2.33) and Eq. (2.34). Each of these follows the form of the the standard transport equation of a scalar quantity closed by gradient diffusion (Bird et al., 2002), with an additional source/sink term to represent the transfer of liquid into vapour.

$$\frac{\partial \bar{\rho} \widetilde{Y}_{\text{liq}}}{\partial t} + \frac{\partial \bar{\rho} \widetilde{u}_j \widetilde{Y}_{\text{liq}}}{\partial x_j} = \frac{\partial}{\partial x_j} \bar{\rho} \frac{D_T}{S_{c_{\text{liq}}}} \frac{\partial \widetilde{Y}_{\text{liq}}}{\partial x_j} - \dot{m}_{\text{vap}} \bar{\rho} \widetilde{\Sigma} \tag{2.33}$$

$$\frac{\partial \bar{\rho} \widetilde{Y}_{\text{vap}}}{\partial t} + \frac{\partial \bar{\rho} \widetilde{u}_j \widetilde{Y}_{\text{vap}}}{\partial x_j} = \frac{\partial}{\partial x_j} \bar{\rho} \frac{D_T}{S_{c_{\text{liq}}}} \frac{\partial \widetilde{Y}_{\text{vap}}}{\partial x_j} + \dot{m}_{\text{vap}} \bar{\rho} \widetilde{\Sigma} \tag{2.34}$$

Instead of defining an individual drop size through a inlet profile, such as the Rosin–Rammler distribution, the flow is characterised by the average droplet surface area per unit mass, Eq. (2.35) where τ_c represents the characteristic time of destruction based upon the turbulent properties of the flow, such that an increase in kinetic energy leads to a decreased destruction time and an increase in surface area production.

$$\frac{\partial \bar{\rho} \widetilde{\Sigma}}{\partial t} + \frac{\partial \bar{\rho} \widetilde{u}_j \widetilde{\Sigma}}{\partial x_j} = \frac{\partial}{\partial x_j} \bar{\rho} \frac{D_T}{S_{c_{\text{liq}}}} \frac{\partial \widetilde{\Sigma}}{\partial x_j} + \frac{\bar{\rho} \widetilde{\Sigma}}{\tau_c} \left[1 - \frac{\widetilde{\Sigma}}{\Sigma_{eq}} \right] + S_{\tilde{\Sigma}_{\text{vap}}} \tag{2.35}$$

$$\tau_c = 4.35 \frac{\tilde{k}}{\tilde{\epsilon}} \tag{2.36}$$

In Eq. (2.37) Σ_{eq} denotes the droplet surface area per unit mass for an equilibrium state, assuming that the spray will tend toward this state over a given time (Sidhu and Burluka, 2008). This depends on the surface tension of the fuel along with the rate of turbulent energy dissipation and is calculated via an equilibrium radius value for a droplet, Eq. (2.38).

$$\Sigma_{eq} = \frac{3 \widetilde{Y}_{\text{liq}}}{\rho_{\text{liq}} r_{eq}} \tag{2.37}$$

$$r_{eq} = C_r \left(\frac{\bar{\rho}\widetilde{Y}_{\text{liq}}}{\rho_{\text{liq}}} \right)^{\frac{2}{15}} \frac{\eta^{\frac{3}{5}}}{\widetilde{\epsilon}^{\frac{2}{5}} \rho_{\text{liq}}^{\frac{3}{5}}} \tag{2.38}$$

When the average density, liquid mass fraction and surface area per unit mass are all known, Eq. (2.39) can be used to predict the droplet Sauter Mean Diameter, giving an indication of the quality of the atomization.

$$D_{32} = \frac{6\widetilde{Y}_{\text{liq}}}{\bar{\rho}_{\text{liq}}\widetilde{\Sigma}} \tag{2.39}$$

For a cold flow, (i.e. no vaporization accounted for), Eq. (2.33) and Eq. (2.35) represent the core of the model with the focus being on the breakup of the liquid jet in the dense area of the spray close to the injection region. Bayvel and Orzechowski (1993) highlights a number of crucial factors relevant to liquid breakup including the viscosity and surface tension of the liquid, stating that higher density liquids develop smaller droplets due to higher kinetic energy.

These observations are important when considering the required setup conditions for the various model quantities, as Eq. (2.32) is highly variable and depends on Favre averaged properties. The high density ratio between liquid and gas along with the high shear gradient close to the inlet mean that the most catastrophic breakup of the liquid will occur in this region, accompanied by the largest change in droplet diameter. In order to specify the initial liquid surface area per unit mass, three quantities must be known. The density of the liquid, the density of the surrounding air (with the assumption that no liquid vapour exists under the initial injection conditions (Sidhu and Burluka, 2008)), and the dimension of the inlet and the corresponding domain cell sizes immediately above.

Another version of the model has been presented in in Lebas et al. (2005), accounting for atomization within the dense part of the spray. Lagrangian particle modelling was implemented to define the spray in the regions far from the injector, but the dependence upon the interface between the Eulerian region close to the injector from the Lagrangian regions was suggested to have an effect upon the model predictions. However, the liquid penetration was well represented for

multiple gas densities along with the expected effects from increasing pressure accountable on the spray formation.

The Eulerian–Lagrangian Spray atomization (ELSA) model detailed in Luret et al. (2010) attributes each separate droplet interaction phenomena to a separate source term, accounting for all phenomena at all regions of the spray rather than the simplification used in Eq. (2.35) to determine all phenomena based on the global turbulence. Rather than relying on an entirely Eulerian framework, this model is also coupled with Lagrangian particle tracking to determine the spray characteristics in the dilute region of the spray (Luret et al., 2010). A high dependence upon the interface method chosen was also accounted for, as with Lebas et al. (2005) along with the the choice of droplet collision mechanism having a significant effect upon the source terms; particularly in the region close to the injector.

Both examples in Luret et al. (2010) and Lebas et al. (2005) make a similar assumption to the Σ-Y_{liq} model covered here, in such that laminar viscosity and surface tension forces acting upon the droplets are not represented in the calculation due to high Weber and Reynolds numbers (Luret et al., 2010). However, the ELSA model was applied to normal jets rather than those deflected for a high speed cross-flow. This may affect initial predictions due to the increased velocity gradients in and around the jet inlet when considering the breakup from a solid liquid core modelled at the jet inlet.

Another approach utilising the single-phase Eulerian approach applicable to pressure-swirl atomization was conducted by Belhadef et al. (2012), as an extension of the work carried out in Vallet et al. (2001). Utilising the Eulerian framework and the same Y_{liq}, Σ and SMD fields covered in equations (2.33),(2.35) and (2.39) with minor changes to the additional terms; this successfully predicts the formation of a hollow-cone spray from a solid liquid core. The overall analysis suggested good liquid axial velocity agreement, but fell short in peak magnitudes for the radial profiles, a good SMD prediction was obtained with the clear separation of large and small droplets within the liquid profile; however this was from a liquid core injected into a static air profile rather than a moving flow (Belhadef et al., 2012).

Application of a modified ELSA model in Demoulin et al. (2007) considers the application of a liquid mass flux to the initial conditions rather than a gradient diffusion to model the liquid dispersal for a co-axial injector in addition to coupling with Lagrangian particle tracking for the dispersed droplets. Noting the importance of turbulence model selection, it was deemed that the standard k–ε could not fully capture the expected level of jet penetration. In addition the number of cells over the face of the injector was found to be important with a number required to capture both the turbulent length scale and adequate jet penetration.

An LES version of the ELSA approach was presented in Chesnel et al. (2011), establishing closure based upon the SGS model from a modified LES base. Since the scales are smaller for LES due to the need for SGS modelling, the grid size was found to be even more important in affecting the results - with the smallest cell sizes determining the minimum scale. When compared to DNS data, this limiting dependence was found to influence the surface density results - citing the need for an SGS closure for both velocity and surface density to improve results along with the critical Weber number. As with the other methods coupled with Lagrangian tracking, the interface method was shown to have a significant impact with the volume of fluid method used effectively being restricted by the mesh size, despite good agreement close to the injector in the dense spray region.

Vaporization Submodel

The process of vaporization in the Σ-Y_{liq} model is handled with the inclusion of Eq. (2.46) as a source term into Eqs. (2.33) and (2.34). This term represents the rate of vaporization per unit mass of liquid, (Sidhu and Burluka, 2008), and accounts for the loss of liquid fuel and the corresponding generation of fuel vapour at an identical rate. Hence these two equations are identical other than the sign of the source term. A further source term, Eq. 2.47, is necessary to account for the loss in liquid surface determined by the rate of vaporization in Eq. 2.35. Mass transfer is accounted for by the Spalding number, covered in detail in Sirignano (2010). Since the assumption of very low residence time for a droplet in a given domain due to high Reynolds number is made in Sidhu and Burluka (2008)

there is no assumed internal temperature gradient formation inside a droplet. Eqs. (2.40) to (2.44) cover the requirements in order to produce a value for the liquid fraction at the surface of the droplet using only basic fuel information along with temperature and vapour mass fraction data.

The latent heat of vaporization is first calculated for the fluid and used to evaluate the relationship between mass fraction and temperature based upon iterating the input temperature, T_∞, to obtain a value of Y_s.

$$L_{vap} = L^0_{\text{vap}} \left(\frac{T_{cr} - T_s}{T_{cr} - T_b} \right)^{0.38} \tag{2.40}$$

$$\frac{1 - Y_\infty}{1 - Y_s} = \left(\frac{c_{p-\text{vap}} T_\infty - L_{\text{vap}}}{c_{p-\text{vap}} T_s - L_{\text{vap}}} \right)^{\left(\frac{c_{p-\text{vap}}}{c_{p-g}} \frac{k}{D_{\text{vap}}} \right)} \tag{2.41}$$

The vapour pressure of the liquid can be calculated based upon available thermodynamic data for the fuel and used to provide an additional value for liquid mass fraction at the surface.

$$\ln P_{\text{vap}} = A - \frac{B}{T} \tag{2.42}$$

$$Y_s = pR_w exp \left(A - \frac{B}{T_s + C} \right) \tag{2.43}$$

The Spalding transfer number can be calculated once a final value for Y_s has been obtained.

$$B = \frac{Y_s - Y_\infty}{1 - Y_s} \tag{2.44}$$

$$u'_d = u' \left(\frac{d}{l_t} \right)^{\frac{1}{3}} \tag{2.45}$$

An average vaporization rate is then evaluated based upon the Spalding number and substituted into the source terms for the transport equations to account

for the loss in liquid mass fraction and corresponding surface area due to vapour formation.

$$\dot{m}_{\text{vap}} = C_{\text{vap}} \rho_{\text{vap}} u'_d \ln(1 + B) \tag{2.46}$$

$$S_{\Sigma\text{vap}} = C_s \dot{m}_{\text{vap}} \frac{\widetilde{\sigma}^2}{\widetilde{Y}_{\text{liq}}} \tag{2.47}$$

The closure problem for the vapour has been resolved by utilising an iterative approach to obtain a simultaneous solution to the equations for Y_s. It is important to note that in Sirignano (2010), observations are made regarding the use of the $\log(1 + B)$, suggesting that it is suitable for vapour phase predictions providing that fast chemistry occurs along with a constant specific heat. Since the average vaporization rate detailed in Sidhu and Burluka (2008) comments upon these assumptions, their effects have been considered. However, when considering the possibility of unsteady effects occurring, such as the horseshoe vortices and vortex shedding in the wake of the jet, there may be additional complications within the calculations. Sirignano (2010) further comments that despite the function $\log(1 + B)$ having only a small variation in a combustion environment, it may not be suitable with the unsteady effects at high Reynolds number due to the increase in liquid vaporization rate as a result of the velocity.

An earlier study without the inclusion of Eq. (2.47) can be found in Beheshti et al. (2007) where the importance of turbulence model selection to establish the important flow features including recirculation, however it was the importance of correct inlet profile conditions for velocity which governed the primary atomization as a result of the affected turbulence. Without fully profiled pipe velocities at the inlet for a gas co-flow it was found that the liquid core did not break up sufficiently quickly, however the type of injector used would also govern the necessary velocity profile.

Updated Vapour Modelling

In order to fully utilise liquid modelling capability, the phenomena of liquid vaporization into gas at high temperatures must be considered. Frequently in com-

bustion systems the temperatures can exceed the boiling point of the fuel and this phase change must be accounted for. Coupling this phenomena with atomization requires additional terms to be added to those equations used previously to account for the change in available liquid surface due to vaporization. With the source term magnitude between Eqs. (2.33) and (2.34) identical, it is assumed that all vaporized liquid fuel is converted directly into vapour with no reversible phase condition enabled regardless of the local temperature. It is important to note that Eq. (2.47) is considered to be a 'sink' term and therefore negative for this study which considers a monodisperse spray, the sign may actually change for a polydisperse spray, in turn the phase change is assumed to be one way and does not take into account any formation of liquid from vapour (Sidhu and Burluka, 2008).

A key quantity in determining mass transfer between liquid and gas phases is the Spalding number and this is calculated from the liquid surface mass fraction. Previously the Antoine equation was used for vapour calculation in Sidhu and Burluka (2008), however when considering the availability of thermodynamic data this expression can be replaced with a polynomial fit obtained from Reid et al. (1987), see Eq. (2.48).

Equations (2.42) and (2.43) can been replaced with the following terms to determine the liquid mass fraction at the surface via vapour pressure:

$$ln\frac{P_{vap}}{P_c} = (1-x)^{-1}[Ax + Bx^{1.5} + Cx^3 + Dx^6] \tag{2.48}$$

$$X_s = \frac{P_{vap}}{P_{ref}} \tag{2.49}$$

$$Y_s = \left(1 + \frac{W_a}{W_v}(\frac{P_{ref}}{P_{vap}} - 1)\right)^{-1} \tag{2.50}$$

With this addition, two solutions for Y_s, Eq. (2.41) and Eq. (2.50) can be solved simultaneously to calculate the solution when the input temperature is iterated. It is the intersection point of these two relationships from which the surface temperature is obtained and the liquid surface mass fraction solved, see Figure 2.3.

Table 2.1: Thermodynamic properties of Jet-A and DF-2.

Fuel	L^0_{vap} (kJ/kg)	T_b (K)	T_s (K)
Jet-A	266.5	447.3	617.7
DF-2	254.0	536.4	725.9

The increase in liquid vapour presence shifts the entire prediction curve for Y_s toward higher surface temperatures and hence a greater level of mass transfer. This has the effect of increasing the average vaporization rate rate, see Eq. (2.46), with the Y_s - T_s gradient resulting in a greater evaporation rate for higher average temperatures. With the additional requirement of species molecular weights, these formation curves will differ for every individual fuel considered but remain valid over an extremely high average temperature range.

New Σ Boundary Conditions.

As defined by Beheshti et al. (2007), the boundary condition for Σ at the liquid jet inlet references a value of Δr over which the condition is applied. However, Eq. (2.51) contains a product of the average density in a region assumed to be occupied by a liquid core. Given the assumption of primary breakup from a liquid mass fraction of 1 and a very small cell height needed to capture the jet to avoid under-resolution; this approach may not be sufficient. In addition, it can be considered that in the centre of a liquid jet there is no surface area produced and hence Σ should be zero. A value should then only be prescribed to the outer region of the jet - which would consist of a product of the average density rather than liquid only.

Therefore it was considered that the liquid jet boundary should be altered and split into 3 separate regions, as outlined in Figure 2.4. Within the three separate regions, the value for $Y_{\text{liq}} = 1$ is only prescribed on the inner and first outer ring whereas the second outer ring is assumed to contain only air due to its placement outside the fuel surface. Σ is then calculated from the first and second outer rings, allowing for an average density of air and fuel to be used and set to zero in the inner-most region. The width of of the first and second outer rings is kept

identical and defined by the quantity, Δr. This quantity in Beheshti et al. (2007) refers to a characteristic cell size over the entire inlet region, but the definition has been changed here to represent the width of the outer inlet regions as per Figure 2.4. To determine if the magnitude of Δr was important to the sensitivity of the SMD downstream, multiple meshes were constructed which halved the magnitude of Δr, already a function of the inlet radius. This effectively checked the grid independence of Eq. (2.51).

$$\Sigma_0 = \frac{2}{(\rho_g + \rho_l)\Delta r} \tag{2.51}$$

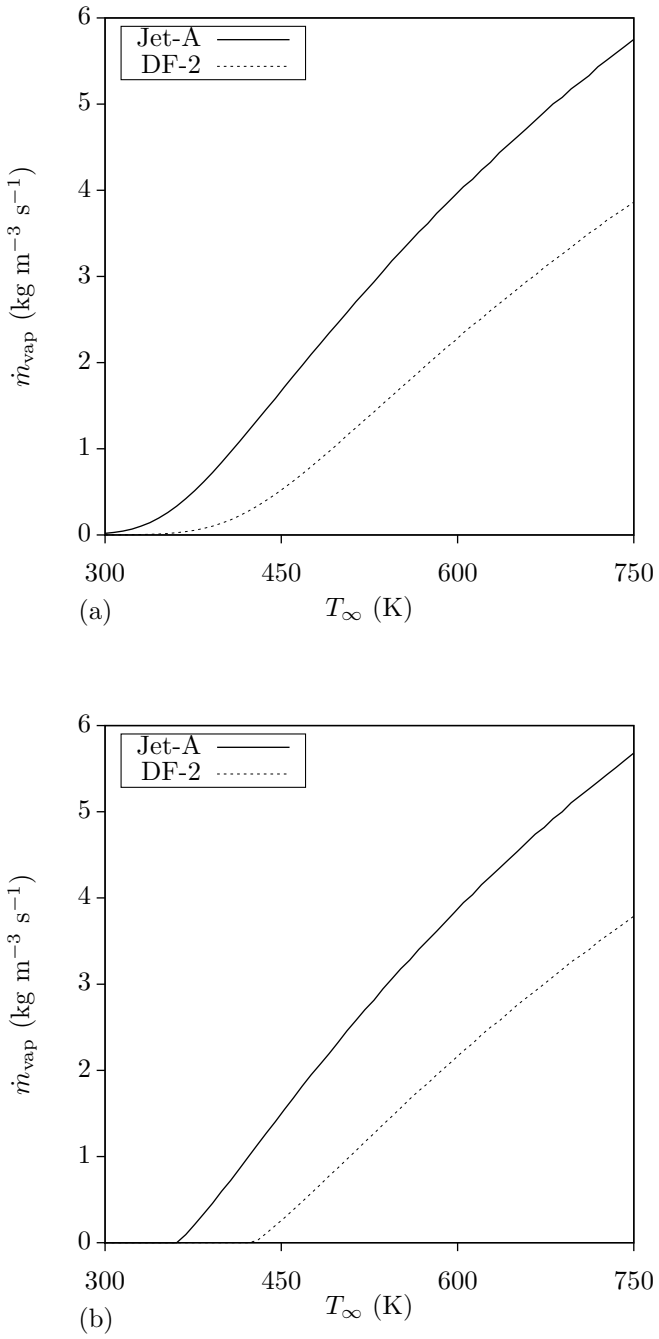

Figure 2.3: Average vaporization rate of kerosene (Jet-A) and diesel (DF-2) versus free stream temperature: (a) $Y_\infty = 0$, (b) $Y_\infty = 0.05$.

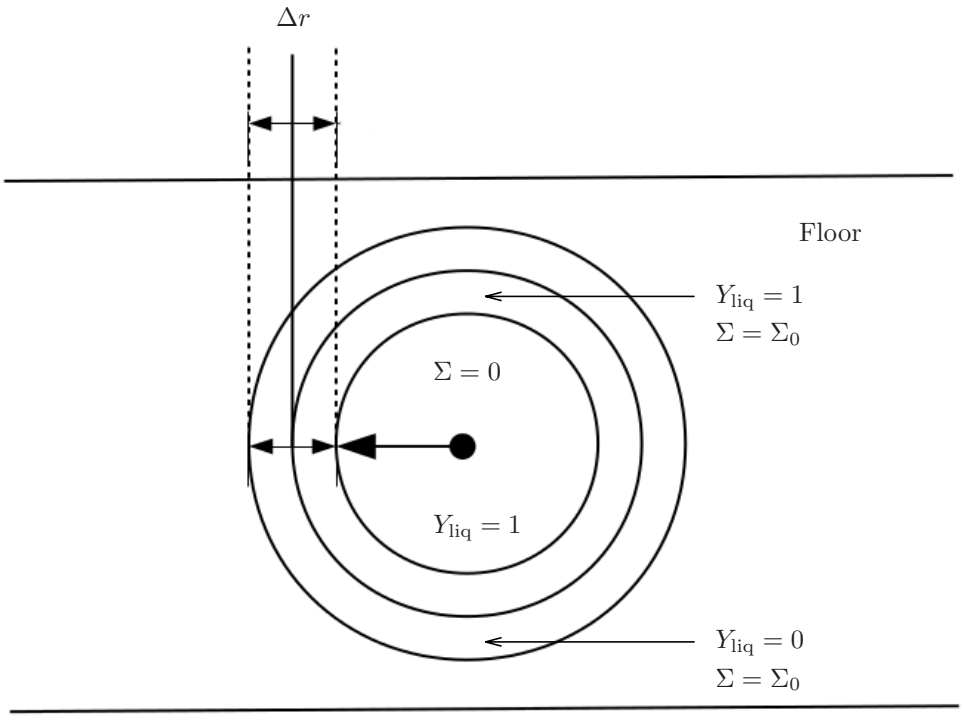

Figure 2.4: Top view of boundary conditions for Σ and Y_{liq} at the jet inlet.

Chapter 3

Simulation of a Gas Jet in Cross Flow

In order to examine the effectiveness of the CFD prediction of a jet in cross-flow, an initial comparison against experimental data was carried out using two different modelling methods. The experimental setup, presented in Crabb et al. (1981), consisted of a gas jet with a circular inlet presented normal to a cross flow of air. Both RANS and LES modelling approaches were evaluated, initially against experimental data followed by a study on the effects of changing the jet momentum ratio.

3.1 Numerical Setup

Figure 3.1 presents a schematic diagram of the computational domain used in the simulations presented within this chapter.

The original experimental results were obtained using Laser-Doppler Anemometry in regions of high turbulence close to the jet inlet. Hot-Wire Anemometry was used further downstream where both the turbulence and shear rate was lower. Both average velocities and RMS stresses in the x and z directions were calculated and were used as a measure of accuracy for the predictions.

The initial step was to establish the various computational domains for the RANS and LES cases against experimental data. These simulations were based

around the data presented in (Crabb et al., 1981). The experiments were conducted in a wind-tunnel type domain at atmospheric pressure with a single circular jet inlet placed on the domain floor normal to the free-stream air flow measuring 25.4 mm in diameter, 0.15 m downstream from the cross flow air inlet.

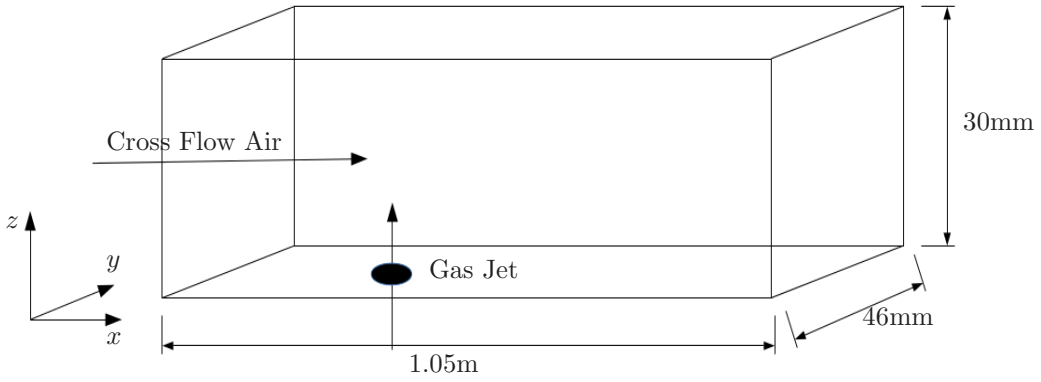

Figure 3.1: Computational Domain for gas jet simulations.

Depending upon the type of simulation performed, either RANS or LES, there are a number of factors which must be taken into account when setting the boundary conditions. Inlets for RANS are of the steady-state type which means the value set at this face does not change with time, with a single velocity magnitude which can be assigned to each direction. However, as the LES cases are not steady-state, this condition is not suitable and so a boundary condition which varied the velocity magnitude was required.

This involved application of a condition which fluctuated around a set mean velocity value by a user-specified percentage; this specific boundary type present in OpenFOAM: turbulentInlet generates a random velocity fluctuation at the inlet from a specified turbulent intensity, set at 5%.

The outlet is specified as a pressure outlet for both simulation types and only requires a single value for the static pressure. For these cases the pressure differences occurred only around the jet inlet with no predicted gradient over the rest of the domain.

Solid walls for RANS need to be used in conjunction with the wall functions which calculate a models behaviour close to the domain wall. However, this

Table 3.1: Locations of LDA measurements by Crabb et al. (1981).

Location	y (mm)	z (mm)	y/D	z/D
1	0	6.35	0	0.25
2	0	19.07	0	0.75
3	0	34.29	0	1.35
4	0	63.50	0	2.5
5	6.35	6.35	0.25	0.25
6	12.7	19.07	0.5	0.75
7	12.7	34.29	0.5	1.35
8	12.7	63.50	0.5	2.5
9	12.7	6.350	0.5	0.25
10	25.4	19.07	1.0	0.75
11	38.1	34.29	1.5	1.35
12	38.1	63.50	1.5	2.5

Table 3.2: Additional monitoring locations (c.f. Table 3.1).

Location	y (mm)	z (mm)	y/D	z/D
5	12.7	6.35	0.5	0.25
9	25.4	6.35	1.0	0.25

can cause issues with regards to turbulence. Of particular relevance are the two-equation models which revolve around the laminar transport equation for a quantity. In these cases, an incorrect velocity prediction may alter the level of turbulent kinetic energy at the walls, affecting the source terms within the model; see Section 2.1.2. This may lead to issues including poor boundary layer formation or excessive turbulence.

To prevent these issues, a special set of boundary conditions are required. Each of these functions is designed to apply to the first layer of cells above the domain floor and correct the behaviour of the simulation within this region to prevent any of the issues described above. LES simulations do not require wall

functions in the same form as their RANS counterparts. This is due to the direct calculation of the turbulent eddies above a set filter size. They instead rely on the sub grid scale model to calculate the small eddies rather than the use of wall functions. This filter is applied over the entire computational domain and all turbulence phenomena above this grid size is fully calculated through the transport equations. Unlike the steady-state nature of RANS simulations this will be constantly changing. A second model is used to predict the formation of small-scale turbulence phenomena, details of which can be found in Section 2.1.2.

The following table presents the boundary conditions for each location in the computational domain for comparison to the experimental data, with the jet to cross flow momentum ratio defined in Eq. (2.30):

Table 3.3: Inlet boundary conditions: (a) validation case q = 2.3, (b) double cross flow velocity q = 1.3, (c) double jet velocity q = 21.

Momentum Ratio	Location	Velocity (m/s)	k	ε
2.3	Air Inlet	12.3	0.567	0.234
2.3	Jet Inlet	27.6	2.857	31.234
1.3	Air Inlet	24.6	2.269	1.872
1.3	Jet Inlet	27.3	2.795	30.2839
21	Air Inlet	12.3	0.567	0.3
21	Jet Inlet	54.6	11.179	1444.8

zeroGradient is a boundary condition that refers to zero flux across the boundary layer for a given quantity. This condition was applied at the domain outlet for velocity, turbulent kinetic energy and dissipation profiles.

Pressure was set to zero at the outlet due to the lack of a pressure gradient across the test area (Crabb et al., 1981). Fluid reference conditions were set at at 1 bar and the flow assumed to be incompressible maintaining a density of 1.2 kg/m^3.

Non-slip boundary conditions were applied at the walls for velocity and a small value of 1 $\times 10^{-15}$ for k and ε to ensure a non-zero solution.

The k–ε turbulence model was chosen for the RANS simulations due well documented records of its behaviour. Whilst earlier tests utilised the k-ω-SST model, see Moffat and Burluka (2013), the dissipation predictions will prove valuable in determining the effectiveness in predicting the case specific turbulence phenomena that may be encountered in the simulations carried out in Chapter 4.

The LES simulations were set up using the standard Smagorinsky SGS model with default values of $C_k = 0.094$ and $C_e = 1.048$ leading to a value of $C_s = 0.0398$, see Section 2.1.2, along with the cube root volume method for determining the filter size. This takes the existing dimensions of the cells and takes the cube root for each dimension, with the existing grid refinements as shown in Figure 3.2, the resultant size is sufficiently small to ensure the capture of the small-scale eddies.

The use of 5% turbulence intensity for both the free-stream and gas jet flow, is carried throughout all simulations. Chosen during the early stages of OpenFOAM testing, this figure presents a medium level of fluid turbulence which was deemed appropriate for inlet air situations during reviews of Crabb et al. (1981).

This turbulent intensity was deemed suitable for both LES and RANS as it allowed for a moderate level of turbulence at the inlet to be accounted for by the two-equation turbulence model. Higher levels of turbulence were not considered as the this was outside of the expected 5 % range.

The only remaining consideration for the domain is the mesh independence, i.e. level of grid refinement required to adequately capture the flow features.

The importance of mesh independence is due to the fact that the data presented in Crabb et al. (1981) concentrated upon measurement regions very close to the symmetry plane, with a maximum deviation of 1.5 inches in the y-direction. The total number of cells was chosen based upon several test iterations performed using various resolution meshes until the change in average velocity and turbulent kinetic energy was minimal.

To ensure mesh independence for each of the simulations, two extremely refined grids were created upon examining results from earlier simulations with much larger cell sizes in both RANS and LES cases. Originally grids containing 2.08 and 4.8 million cells were evaluated against previous predictions presented in Moffat and Burluka (2013). However with an established boundary layer value

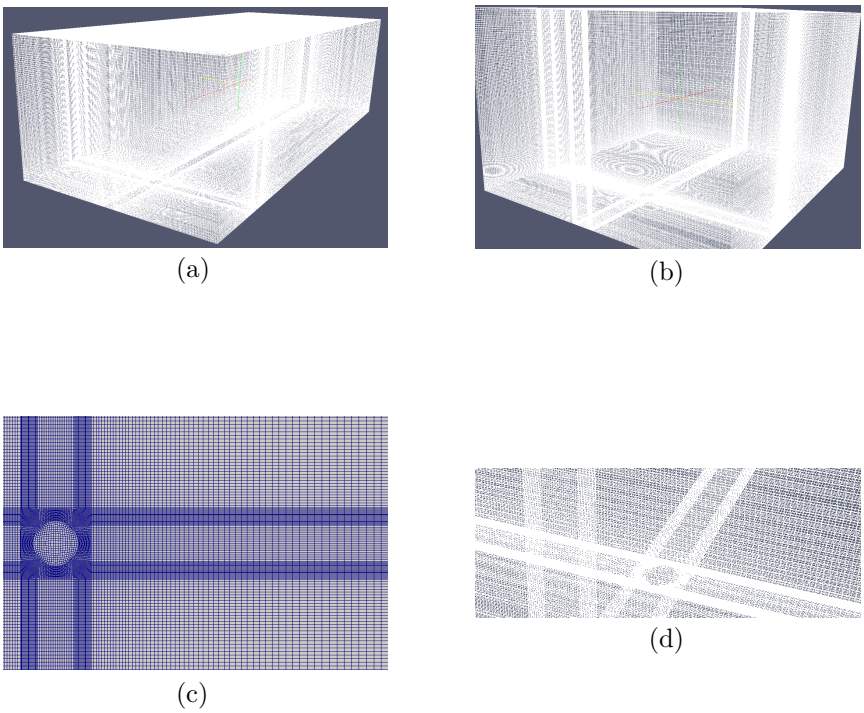

Figure 3.2: CFD Meshes:(a,c) RANS; (b,d) LES.

of 6 mm, (Crabb et al., 1981), the near-wall behaviour presented a poor match, see Figure 3.3, and as a result the cell concentration near the walls was improved.

Due to the nature of the LES simulation, which models all turbulent eddy phenomena above a certain pre-set filter size, the computational domain needed to be far more refined that that for RANS in order to better capture key features in and around the jet inlet. Having too great an aspect ratio, see Section 2.1.3, between cells in this region will lead to a non-uniform mesh which can experience poor prediction; especially in highly turbulent simulations with large flow fluctuations.

The grid resolution aimed for the inclusion of a minimum number of cells required to fully resolve the flow boundary layer at the domain floor. As opposed to previous coarser grids, a ratio was chosen to provide 8 cells for RANS and 12 for LES for the 6 mm boundary layer in the z-direction with the minimum

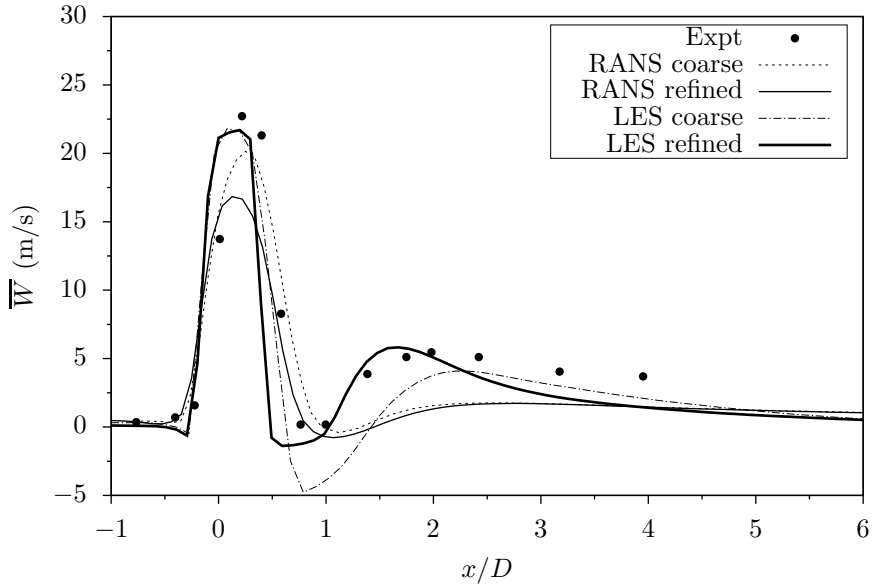

Figure 3.3: Predicted z-component of velocity at Loc. 6 for coarse and fine meshes.

boundary layer cell sizes 0.75 mm and 0.5 mm respectively. These values ensure that the wall functions should not interfere with the main flow whilst providing sufficient resolution over the flow boundary layer.

This refined grid served to both capture all the small-scale features such as vortex shedding on the underside and rear of the jet, crucial in determining the flow pattern close to the inlet in the region of very high turbulence. This region is located in front of the jet inlet close to the domain floor. A well-designed mesh will also reduce the computational load with the reduced cell count in areas that are not of direct interest to the measurements; examples of which are the solid walls at the y-direction boundaries.

In addition, the total length in the x direction for LES was reduced from 1.05m down to 0.5 m to shift the cell concentration upstream in order to better capture turbulence phenomena and increase the grid resolution. The SIMPLE algorithm was used for conducting the RANS simulations whilst LES utilised PISO.

Each simulation required a low physical timescale in order to adequately capture the flow structure in the turbulent region. Ascribing too high a step and this would cause multiple issues including very poor resolution if the flow crossed

Table 3.4: Cell count of CFD meshes used in the grid-independence study.

Domain	Total Cell Count
RANS coarse	2.08 million
RANS refined	5.9 million
LES coarse	4.8 million
LES refined	9.36 million

too many cell boundaries and the possible failure of the solver calculation. LES required a lower timescale compared to the RANS simulations due to the need to adequately capture the small turbulence phenomena on the refined mesh.

The physical timescale used for the RANS simulations was 1×10^{-5} s whereas LES used a time step of 1×10^{-6} s.

Finally, the use of a profiled velocity as opposed to a single Cartesian component used in the previous tests was considered. A velocity profile was applied based upon the $1/7^{\text{th}}$ power law from Masri et al. (2000), see Eq. (3.1). Since there was available experimental data for the jet inlet profile from Crabb et al. (1981), this velocity profile equation was modified to provide a closer fit and takes the form of Eq. (3.2) where U_{avg} is the jet velocity listed in Table 3.3, r is the radial distance from the centre of the inlet and R_j is the inlet radius.

$$U_{inlet} = 1.218 U_{avg} (1 - \frac{r}{1.01 R_j})^{\frac{1}{7}} \tag{3.1}$$

$$U_{inlet} = 1.12 U_{avg} [1 - (\frac{|r|}{1.3 R_j})^{6.5}] \tag{3.2}$$

3.2 Results

CFD results are presented for a software comparison between an open-source code and commercial solver alongside multiple RANS and LES simulations for comparison against experimental data and varying jet to cross-flow momentum ratios. Quantities of interest include the averaged velocity profiles and turbulent kinetic energy predictions close to the jet inlet.

3.2.1 Comparison of CFD Software Packages

A comparison between an open-source package OpenFOAM (Vuorinen et al., 2015) and a commercial code, Ansys CFX, has been made using a simple coarse mesh RANS simulation. The main interest here is to ensure that similar results are reproduced over a variety of platforms to ensure that the important features of turbulence modelling for a jet in cross flow are predicted regardless of the software used. A coarse grid of 1.97 million cells was constructed and set-up in both CFD software packages, a turbulence intensity of 5 % was specified and the k–ω–SST turbulence model used for closure. A total time of 0.1 s for OpenFOAM and 0.025 s for CFX was required to achieve convergence for each simulation with both using an identical physical timescale of 1×10^5 s.

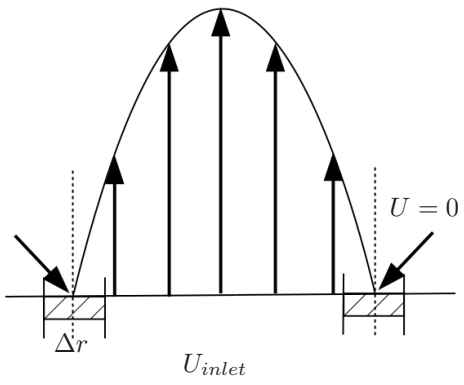

Figure 3.4: Profiled jet inlet velocity, see Eqs. (3.1) and (3.2).

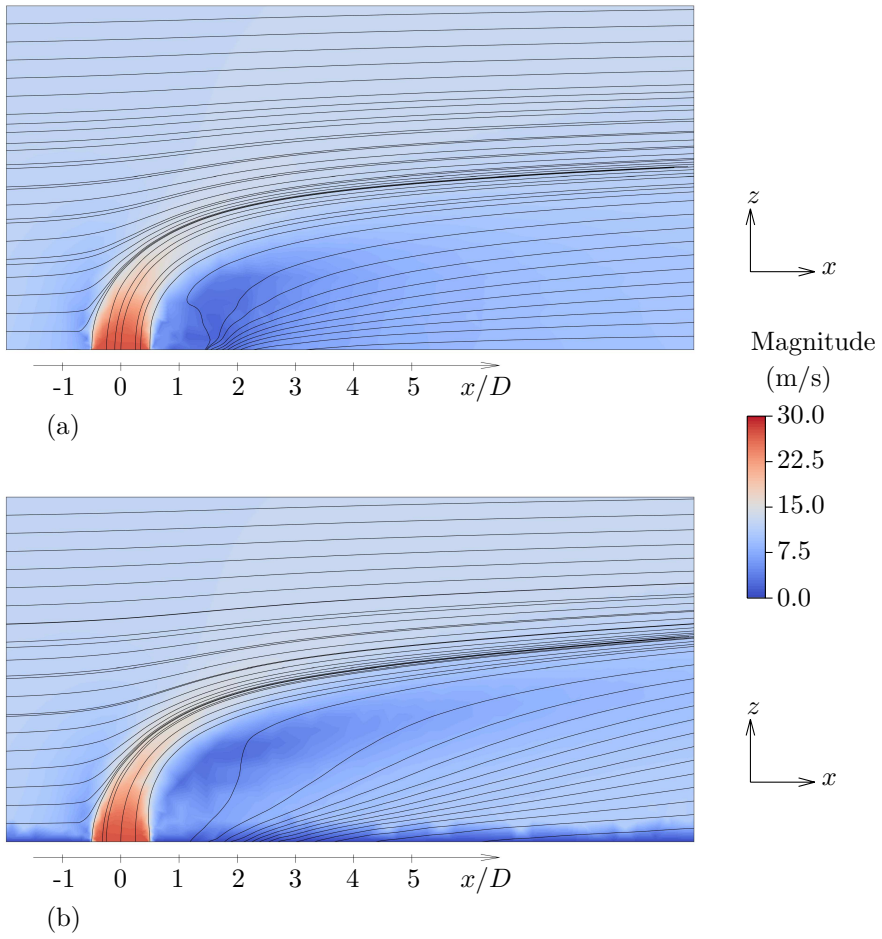

Figure 3.5: Average flow field predicted by RANS in the central plane: (a) Ansys CFX, (b) OpenFOAM.

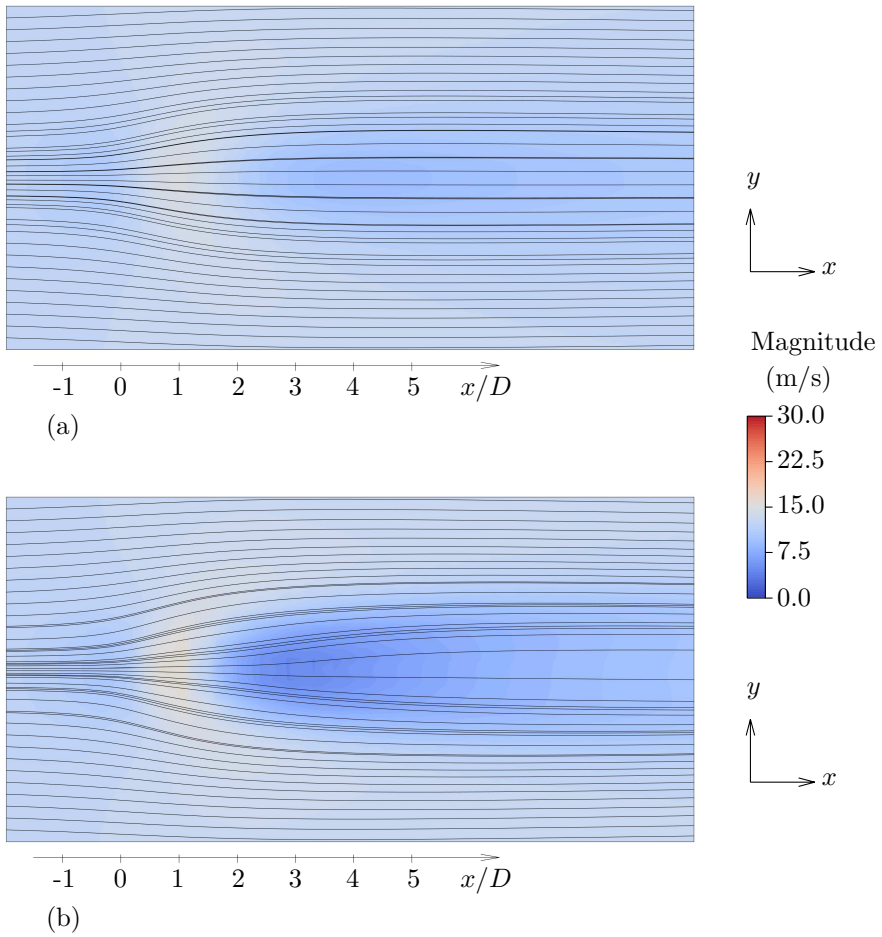

Figure 3.6: Top view of the average flow field predicted by RANS at $z = 5$ mm ($z/D = 0.2$): (a) Ansys CFX, (b) OpenFOAM.

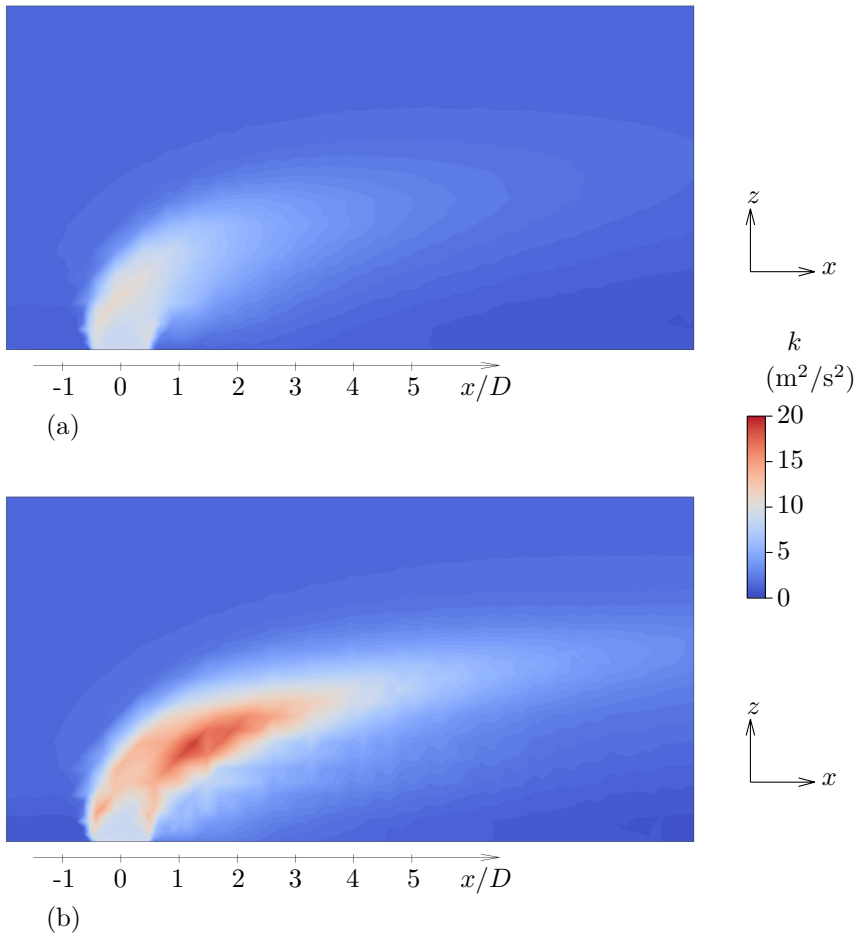

Figure 3.7: Turbulence Kinetic Energy predicted by RANS in the central plane: (a) Ansys CFX, (b) OpenFOAM.

Figure 3.5 shows a shift in the prediction of the low velocity recirculation region between packages with OpenFOAM predicting the region slightly higher above the floor, attached the jet underside up to a greater height; this accounts for the lower velocity predictions downstream as the streamlines illustrate visible greater flow deflection whilst CFX predicts a return to free stream gradient by five diameters downstream. Behind the jet both packages predict the same sudden The xy-plane at $z = 5$ mm in Figure 3.6 also shows the difference in recirculation zone prediction with a noticeably lower downstream magnitude for OpenFOAM between two and five diameters downstream along with greater visible deflection on the flow streamlines compared to CFX.

Velocity prediction differences for the x direction for both CFD packages predict a downstream shift in maximum peak location as the jet is deflected by the free-stream air before the flow returns to free-stream value downstream. Between the two packages it is OpenFOAM which predicts the lowest magnitude downstream for u. There is an improved prediction between software packages for the z-component of velocity with the maximum peak magnitude above the jet inlet showing less than a 10 % difference.

Turbulent kinetic energy predictions close to the domain floor, see Figure 3.7, show an increase in both magnitude and downstream location for OpenFOAM, more than double that predicted by CFX. Whilst both packages show the same magnitude and pattern prediction immediately above the jet inlet, OpenFOAm predicts a further increase in the flow energy between 1 and 3 diameters before it begins to dissipate whereas CFX predicts a constant energy dissipation within this region. This difference may account for the increased flow turbulence present in the OpenFOAM velocity predictions within the underside of the jet. Despite this the overall jet penetration is unaffected as the conditions at the boundary and immediately above the inlet, visible in the lower difference between w velocity components between packages than the u velocity.

Overall the differences between software packages for a simple gas jet in cross-flow simulation are most pronounced in the turbulence model predictions. The major flow features present for a RANS simulation are predicted by both packages with the average velocities differing mostly in the downstream region due to the turbulent kinetic energy. Both the recirculation zone location and vortex pair

are products of the downstream turbulence predictions which can be affected by the turbulence fields whilst jet penetration predictions remain almost identical regardless of software used. These differences can likely be attributed to differences within the versions of the k–ω–SST model implemented between packages such as model constants and internal solver settings; this indicates that accurate RANS modelling between software packages is possible but that attention should be turned to the turbulence modelling constants and individual solver settings to ensure they are suitable for the flow under examination.

3.2.2 Validation of RANS and LES Predictions

Multiple CFD simulations were carried out to examine the accuracy for two different computational modelling approaches, RANS and LES, at predicting the flow features and turbulence characteristics for a typical jet in cross flow. Velocities and RMS stresses for the x and z directions were used as the comparison to experimental data obtained from Crabb et al. (1981). An additional simulation using a profiled velocity inlet modelled after the experimental results was also carried out using RANS and compared to the other 'flat' profile results having run for a total of 15 ms.

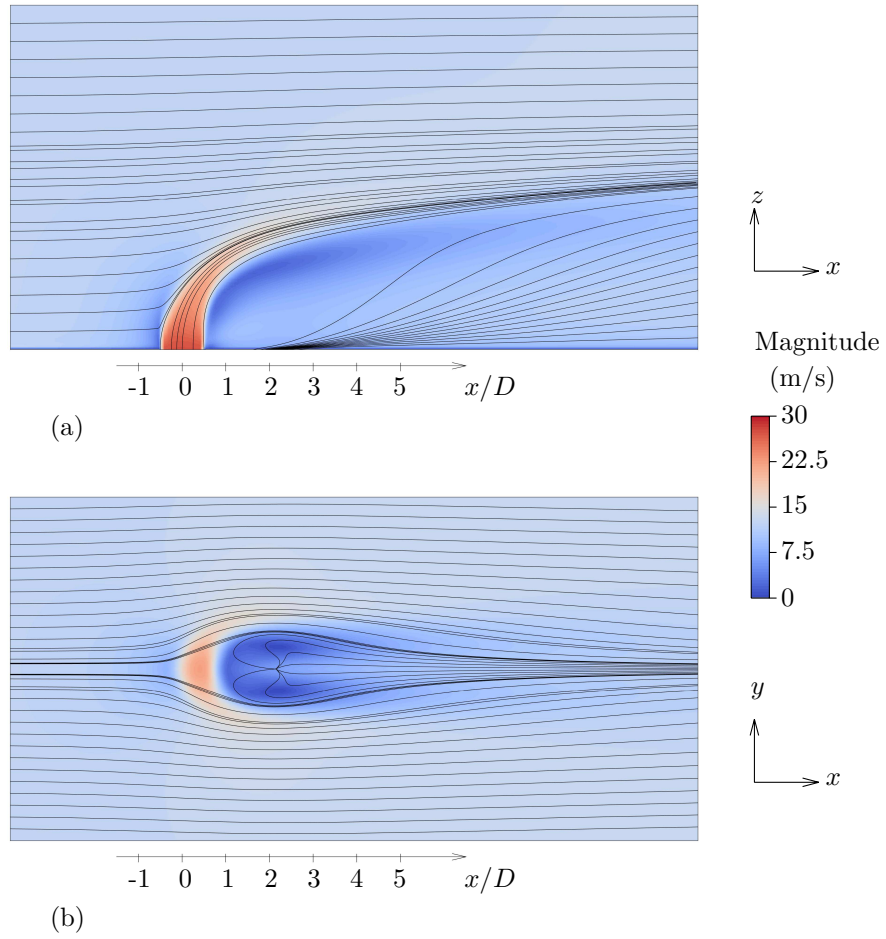

Figure 3.8: Average flow field predicted by RANS for a jet with uniform inlet velocity: (a) side view of the central plane, (b) top view at $z = 5$ mm ($z/D = 0.2$).

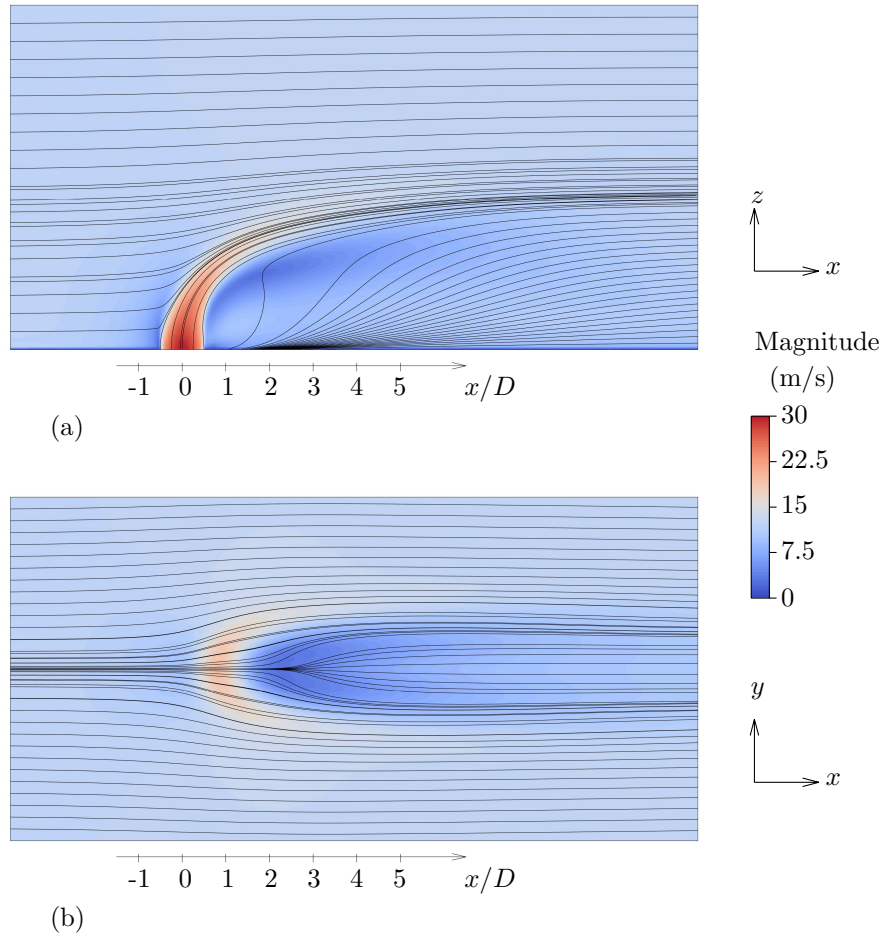

Figure 3.9: Average flow field predicted by RANS for a jet with profiled inlet velocity: (a) side view of the central plane, (b) top view at $z = 5$ mm ($z/D = 0.2$).

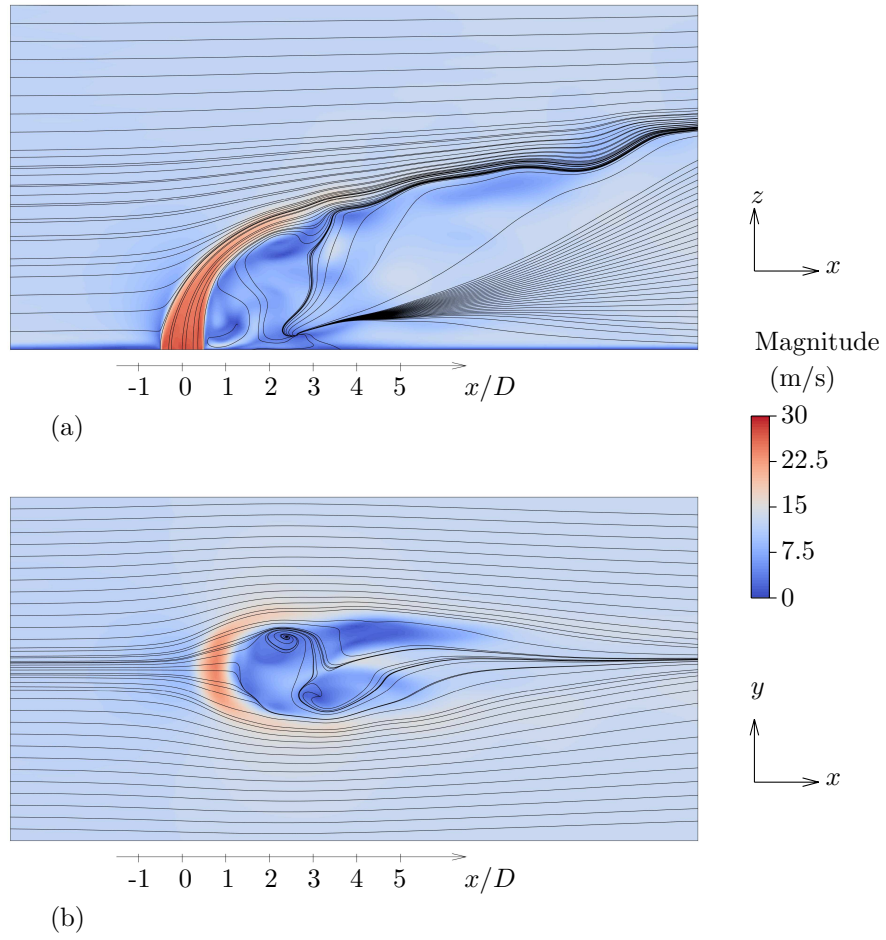

Figure 3.10: Instantaneous flow field predicted by LES for a jet with uniform inlet velocity: (a) side view of the central plane, (b) top view at $z = 5$ mm ($z/D = 0.2$).

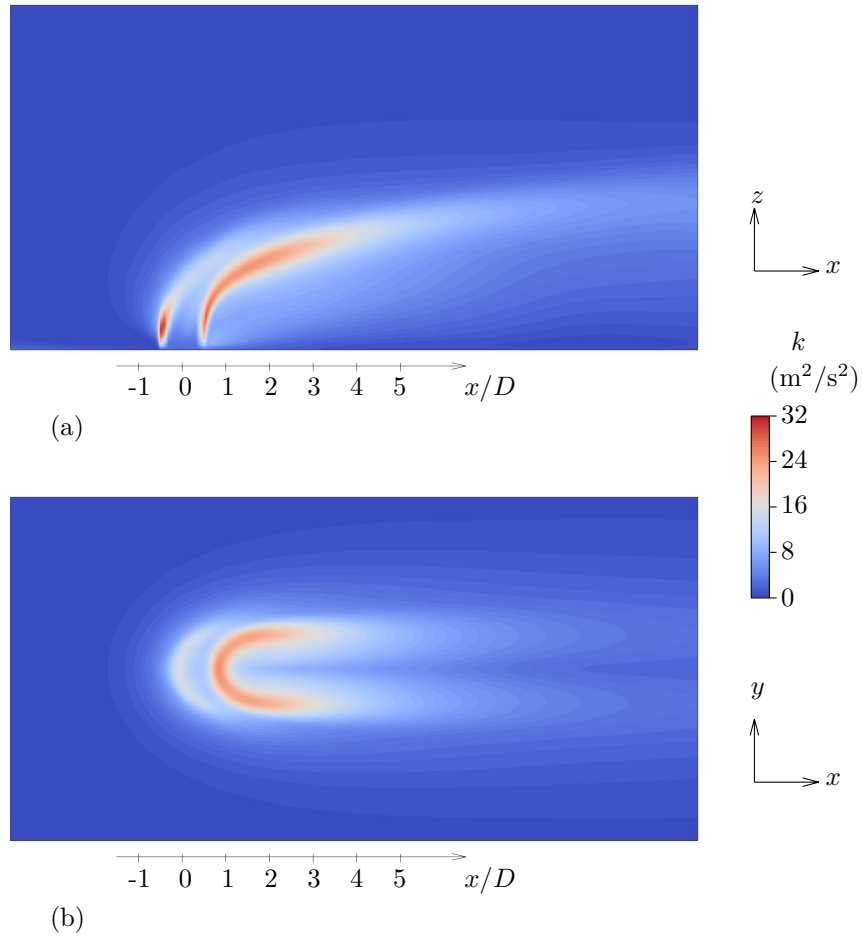

Figure 3.11: RANS Turbulent Kinetic Energy predictions for comparison against experimental data: (a) side view of the central plane, (b) top view at $z = 5$ mm ($z/D = 0.2$).

Figure 3.12: Predicted and measured averages of the x-component of velocity at Locations 1 to 12.

Figure 3.13: Predicted and measured RMS fluctuations of the x-component of velocity at Locations 1 to 12.

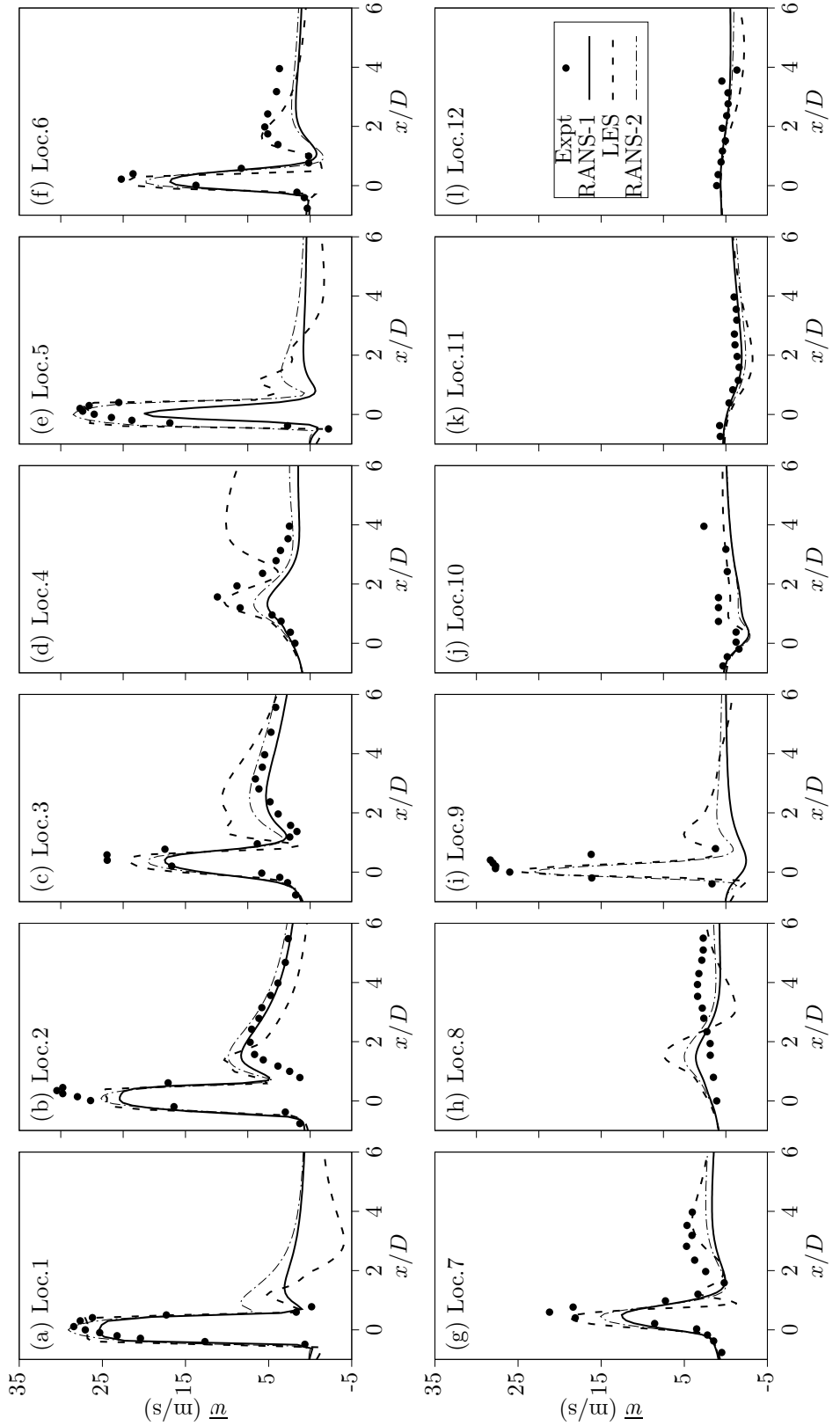

Figure 3.14: Predicted and measured averages of the z-component of velocity at Locations 1 to 12.

Figure 3.15: Predicted and measured RMS fluctuations of the z-component of velocity at Locations 1 to 12.

Examining the simulation results, it is clear that both methods appear to capture the major aspects of the flow, including the typically observed features for a jet in cross-flow; visible in Figure 2.2.

The average u predictions close to the jet inlet in Figure 3.12 highlight some of the key features of the expected jet in cross flow profile, including the large negative value troughs indicating the presence of a recirculation zone and the gradual gradient decline when moving away from domain centreline. Locations 3 – 4 under predict the peak magnitudes for RANS-1 by up to 50 % at $x/D = 0.5$, but exhibits all the correct peak locations present within the experimental data. In particular the large peak predicted at the rear of the jet, indicating acceleration of the flow as it is deflected, is generally absent over the entire measurement range with only a small peak present. Directly comparing to the experimental data, the average u predictions maintain an average correlation of over 0.735 throughout these Locations, which improves with distance from the symmetry plane in the y direction. Predictions for the kinetic energy within this region, see Figure 3.11, predict areas of high magnitude either side of the jet inlet. However this is not reflected in an identical peak in the u velocity predictions alone. Considering the restrictions within RANS turbulence modelling listed in Section 2.1.2, it is not assumed that individual RMS velocity components are equal and the highly turbulent region can quickly change both sign and magnitude. With the jet having been deflected very heavily by Location 4, the majority of the flow component tends toward the x direction rather than the z direction. A likely cause of the steep gradients close to the floor is the deflection of the free-stream flow by the normal jet, with the increase in flow speed in the y direction and high level of shear present generates the additional turbulence lower toward the floor, with the refined grid reducing any interference from the wall functions assigned to the k–ε turbulence model. Each LES result for the average values of u on the symmetry plane demonstrate a superior prediction capability for peak magnitudes over RANS. Location 3 predicts the correct minimum peak magnitude after the jet inlet but also under-predicts the first peak magnitude at the same value as RANS. Another significant difference is visible at Location 4 where a steep gradient decrease is predicted at $x/D = 1.5$ where the velocity tends to 0 before slowly increasing toward the free-stream value, this is unexpected as neither RANS

prediction nor experiment data predicts this level of turbulence on the upper surface of the jet. Dropping to less than zero with a maximum difference of 10 m/s from the RANS predictions, the average correlation to the experimental data drops significantly down to 0.52 which indicates a very poor match for almost half the measured region compared to Location 2 and 3 which are 0.83 and 0.71 respectively. A profiled jet inlet velocity for RANS-2 does not show significant change from the conventional RANS i profile except in the prediction of peak magnitudes where it is either equal to or superior in matching the experimental data. In particular the minimum peak at Location 3 at $x/D = 1.5$ where RANS-1 over-predicts by 5 m/s, RANS-2 profiles almost identically to LES, reducing the difference between profiles by 50 % at the peak. However the large under-prediction at Location 2 between $x/D = 0.5$ remains, regardless of the CFD method used.

Mid-distance from the jet inlet between Locations 6 – 8 there is a better overall match between the experiments and peak magnitudes with the average correlation for RANS-1 rising to 0.825, but with a continuing under prediction of the peak velocity due to flow deflection at $x/D = 0.5$ by up to 30 % at Location 7. Despite the peak difference, all axial peak locations are correct up to Location 8 where the experimental data exhibits a downstream peak shift due to increased jet penetration over RANS predictions. This trend continues through to the LES predictions at Locations 6 to 7 onto the outer edges of the jet with a continuous improvement in peak magnitude predictions over RANS, however close to the domain floor at locations 1, 5 and 9 large fluctuations appear in regions of high turbulence and shear. These predictions suggest that the flow on the edge of the boundary layer (6 mm) may be extremely turbulent; visible in Figure 3.10. However the drop in average correlation from 0.88 at Location 6 to 0.64 by Location 8 shows that the flow behaviour on the upper surface of the jet for LES is extremely turbulent beyond $x/D = 2$ with the same behaviour predicted at Location 4. The separation between RANS-1 and RANS-2 is most evident close to the floor at Location 5 with the RANS-2 predictions more in common with LES than RANS-1, tending to 0 at the centre of the jet inlet. This difference reduces from 10 m/s down to less than 3 m/s by Location 8, largely

due to a reduction in downstream velocity predictions beyond $x/D = 4$ whilst retaining all peak magnitude locations and upstream patterns.

When moving to the outer measurement regions in 9 - 12, the lower level of turbulence present sees a drop in the level of under- prediction between the RANS-1 case and the experimental data with only the single peak several diameters downstream from the inlet, indicating the presence of the flow accelerating as the counter-rotating vortex pair is formed. The under-prediction by several m/s can be traced to the low kinetic energy within this region with average correlation values remaining relatively constant between 0.87 - 0.9, indicating that it is the free-stream conditions which primarily affect flow behaviour in this region. The RANS-2 results show little change from RANS-1 due to the low kinetic energy and lack of effect by the z component of velocity. LES predictions within this outer region show an improved match to the experimental data with the average correlation 0.925 or better. This improvement shows that the turbulence calculation for LES is superior to that of RANS within this region, suggesting that it is the smaller scale phenomena within the free-stream which RANS is unable to predict that influence the flow.

Examination of the RMS stresses for the x component of velocity within these regions in Figure 3.13 support the predictions shown in Figure 3.12 with upstream peak values decreasing with increasing height along with a lower magnitude downstream away from the turbulent recirculation zone. Locations 1 – 3 for RANS-1 do not predict the single large peak present in the experiments at $x/D = 1.0$ but instead exhibit a twin-peak more expected in the w predictions as this suggests a more even velocity distribution around the inlet. However the reduction in magnitude means that the average correlation remains good at Location 3 at 0.90 but with the under-prediction for almost the entire downstream region at Location 4 this decreases. Since this phenomena is located along the domain centreline rather than the outer edges, it is likely that this is the prediction of the additional jet in cross flow features on the upper edge including the horseshoe vortices and vortex shedding. Although not physically visible the fluctuations indicate the presence of turbulence phenomena within this region. The remaining RANS-1 predictions present a reasonable match to the experimental data, particularly for the furthest regions in Locations 10 – 12 beyond $x/D = 2$, confirming the capability of RANS

to model the RMS stresses in the lower turbulence regions and also managing to predict the major peaks in more turbulent regions. RANS-2 RMS stresses remain very similar to that of RANS-1 due to the similar velocity gradients throughout the measurement regions with the total difference always less than 3 m/s. The general trend exhibiting under-prediction close to the floor until $x/D = 3$ before increasing with z, better matching the experimental data beyond $x/D = 2$ for Locations 3,4,7 and 8. However the same over-prediction trends upstream from the inlet still apply, indicating that although the profiled velocity presents an improvement downstream it is the RANS method in general which accounts for the major differences between experiment and simulation rather than boundary conditions. LES RMS stresses for u show that the majority of profiles are under-predicted compared to both RANS and experiments, the average values present a far superior match. This is particularly notable at locations 1 to 4 where no predictive value exceeds 4 m/s. Only by Location 8 in the regions of lower turbulence on the edges of the jet does the magnitude begin to match to within 5 m/s of the experiments, resulting in an average correlation less than 0.45. Even in the outer region between Locations 10 – 12, the LES simulations still under predict the experiments and RANS equivalents, remaining below 2 m/s and suggesting that the shear between the free-stream and jet flow is under-predicted on the upper surface.

The average w predictions in Figure 3.14 for RANS-1 initially present a similar pattern to u with under-prediction in the peak magnitudes but predicting all the correct peak locations. Along the domain centreline for Locations 2 – 3 the secondary peak predictions at $x/D = 1$ in front of the inlet match the experimental peak locations well, exhibiting a reduction in intensity with an increase in z and an average correlation greater than 0.75. This continual drop indicates that the level of jet penetration predicted is less than the experiment, but a change in the flow structure is not observed along the symmetry plane as all peaks retain their positions. Moving further from the symmetry plane between Locations 5 – 7 the primary peak is consistently under-predicted by up to 8 m/s, indicating a deficiency in the predicted jet penetration throughout the domain for RANS-1. The lack of a peak prediction in Location 9 along with low magnitudes beyond this region indicate that the flow has become heavily influenced by the

free stream component by this point with the turbulent energy dissipation reducing the velocity magnitude in the outer jet region. LES z velocity component predictions illustrate an improvement in peak magnitude predictions over RANS, often capturing the correct jet penetration above the inlet. This is most noticeable at Locations 1, 5 and 9 which correctly capture the primary peak height in addition to the correct magnitude and position at the downstream peak for Locations 6 and 7. One important observation is visible at Location 4 with a large over-prediction of downstream velocity beyond $x/D = 2$. When considering a large under-prediction for the same location in Figure 3.12 this suggests the presence of an extremely turbulent downstream wake beyond the expected location of the recirculation area. The presence of vortexes underneath the jet is an expected phenomena, see Section 2.2, but is not predicted by the RANS simulations. A similar phenomena is visible at Location 8 with Locations 5 – 7 showing a minimum of a 20 % increase in primary peak magnitude over RANS-1. The low magnitude predictions in the far regions are within several m/s of RANS over the entire measurement range, indicating that both simulation types consider the free stream velocity component to be the primary influence within this area as any major effect from the jet inlet velocity has dissipated by this point. Overall LES provides an improved prediction to RANS-1, particularly in peak magnitudes upstream whereas both predictions are very similar to each other at the outer jet edges. The downside is that LES seems to over-predict downstream magnitudes beyond the recirculation zone at x/D = 2, notable at locations 3, 4 and 8. This is likely due to the extreme wake turbulence downstream. RANS-2 predicts a notable increase in jet peak velocity over RANS-1 and closely matches LES with frequently less than a 5 m/s peak separation between Locations 1 – 8 as opposed to the greater gap of up to 10 m/s for RANS-1. Once consequence of this appears to be the over prediction of the secondary peak at $x/D = 1.0$ in a similar trend to LES, however the velocity gradients afterward tend to match that of RANS-1, reaching a free-stream value within 1 m/s by $x/D = 6$. Locations 4 and 8 only show a small improvement over RANS-1 with a general magnitude increase of approximately 15 % beyond $x/D = 1.5$ but still presenting a poor peak magnitude match. The biggest change between RANS-1 and RANS-2 is the large jet peak at Location 9 which was not predicted at all by RANS-1 whereas

RANS-2 predicts a peak magnitude within 3 m/s of LES but still more than 15 % lower than the experimental data points. Differences between RANS simulations beyond Location 9 are extremely small as the flow is largely influenced by the free stream x component of velocity within this region.

RMS stresses for w are a function of the turbulence kinetic energy as with the u RMS stresses,albeit with a lower magnitude for any RANS simulation; see Eq. (2.18). As with the RANS-1 u RMS stresses, the peak magnitudes are under-predicted over the entire measurement range compared to the experimental data, but all profiles accurately predict the major peak locations with the exceptions of Locations 4 and 9. The decrease in the velocity gradient as the values return to their free-stream magnitudes beyond $x/D = 2$ corresponds to the increasing diffusivity for the turbulent energy over Locations 1 – 8 with the regions of lowest turbulence from 9 – 12 presenting the best match. The higher peaks upstream occur either side of the jet inlet, this corresponds to the points of highest shear in the flow as the free-stream is deflected by the gas jet and forms the wake. LES RMS stresses for w generally under-predict the experimental data by $x/D = 2$ diameters between Locations 1 – 7 as with the u RMS stress components - but also have large peaks which begin over the jet inlet and gradually move downstream with an increase in z. These locations correspond to the region of the recirculation zone where high shear can occur and suggest the presence of turbulence phenomena not captured by RANS modelling such as the vortex shedding on the underside of the jet which would account for the reduction in intensity and movement upstream as the flow is deflected. By Location 10 at the jet edge, predictions are similar those from the RANS method but never exceed 1 m/s whilst RANS-2 peaks at 2.5, indicating a difference between approaches in regions of lower turbulence despite the improved capability of LES to capture small scale turbulence phenomena. RANS-2 w RMS stresses differ in the predictions to the RANS-1 counterparts due to the improved jet penetration which accounts for greater turbulent kinetic energy around the jet inlet and hence a higher peak magnitude despite being a function of k as with the u RMS component. This leads to an increase in magnitude over the RANS-1 equivalent beyond $x/D = 1$ for profiles close to the floor and over the entire distance further away from the floor - bringing the match closer to the experimental data. However the general

comparison is still relatively poor with peak magnitudes less than 50% of the experimental data in the upstream region prior to Location 8. With a large reduction in the maximum value for experimental data, the match improves as the overall magnitude is still higher than that of RANS-1 until Location 11 where there is a general over prediction before $x/D = 2$; indicating an over-estimation of the upstream RMS stresses - likely as a result of the limitations of RANS presented in Section 2.1.2. Regardless of computational approach, all methods appear to under-predict the RMS stresses for w until the outer edges of the jet.

Despite these differences to the experimental results, the RANS simulations provide a good prediction of a jet in cross flow, particularly in predicting the location of the major flow features despite the under-prediction of peak-magnitude. The addition of a profiled velocity inlet to the jet improved peak predictions for the w and improved RMS predictions. Unlike LES where each velocity component is calculated individually, the restrictions on RANS modelling mean that it is the calculation of the turbulent kinetic energy which has the greatest impact on these results, however all computational methods were found to under-predict the RMS stresses - in particular on the upper edge of the jet surface at Locations 4 and 8. LES presents the best jet penetration predictions and more accurately models the downstream flow phenomena such as the secondary velocity peak at Locations 6 and 7 along with the peak at Location 9 which is absent from RANS-1 entirely. However the increased turbulence on the outer edges at Locations 4 and 8 with 10–12 reduced the prediction accuracy and made all computational approaches predict comparable results.

Majander and Siikonen (2006) presents the results of an LES simulation compared to the experimental results in Crabb et al. (1981) which provides a superior match against the LES simulation conducted within this study. In particular the region in front of the jet inlet close to the wall between $x/D = 2$ and $x/D = 6$ the z and u predictions do not exhibit the same fluctuations on the central plane as the LES averages in Figures 3.12 and 3.14. The RMS values also do not under-predict the z-component results to the same degree as highlighted in Figure 3.15, which indicates that the introduction of the jet pipe to the liquid inlet alters the flow sufficiently to improve the match to the experimental data. However it is noted that the close wall modelling still remains an issue and requires extremely

refined cells; indicating that both a profiled inlet velocity and very low y^+ are required to obtain a reasonable agreement for LES.

Overall it is the LES approach which provides superior average velocity predictions for the turbulent flow profile, able to capture more features including the small scale vortices but at the cost of computer time and grid size. Both methods capture the large scale major flow aspects including the vortex pair and recirculation zone, but RANS is incapable of predicting certain phenomena due to its steady state nature - but with a sufficiently refined grid and profiled inlet velocity, relatively accurate results can be obtained for both average velocities and RMS stresses - indicating that RANS is a suitable method for determining jet in cross flow quantities with a lower computational cost than LES.

3.2.3 Effect of Changing Momentum Ratio

With the comparison to experimental data showing the accuracy of the different modelling methods, attention was shifted to the change in flow behaviour with the variation of the inlet velocities. Using the same mesh grids as described in Section 3.1 the inlet parameters were changed to produce simulations with jet to cross-flow momentum ratios of 1.3 and 21.3 respectively. These predictions were compared to the experimental simulations and patterns established on the changes in the predictions.

All RANS simulations were run for a duration of 50 ms to ensure low residuals and an adequate averaging over a suitable number of results files, all physical timescales and discretization settings were unchanged from the original simulations to order to ensure that only the inlet parameters are varied to present the most accurate comparison possible. The boundary conditions for the two cases are listed in Table 3.3.

RANS Results

All figures are generated from individual time scale results files with all graphical data appropriately time averaged, see Section 2.1.2 for details.

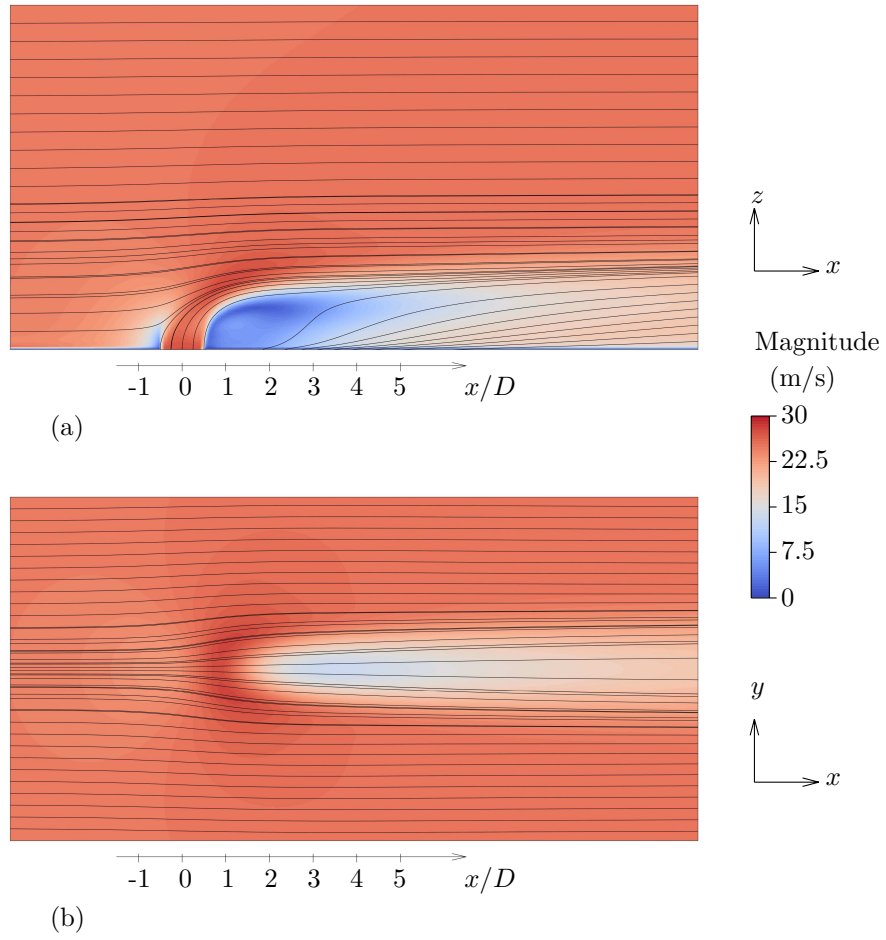

Figure 3.16: Averaged flow field predicted by RANS for reduced jet momentum ratio, $q = 1.3$: (a) side view of the central plane, (b) top view at $z = 5$ mm ($z/D = 0.2$).

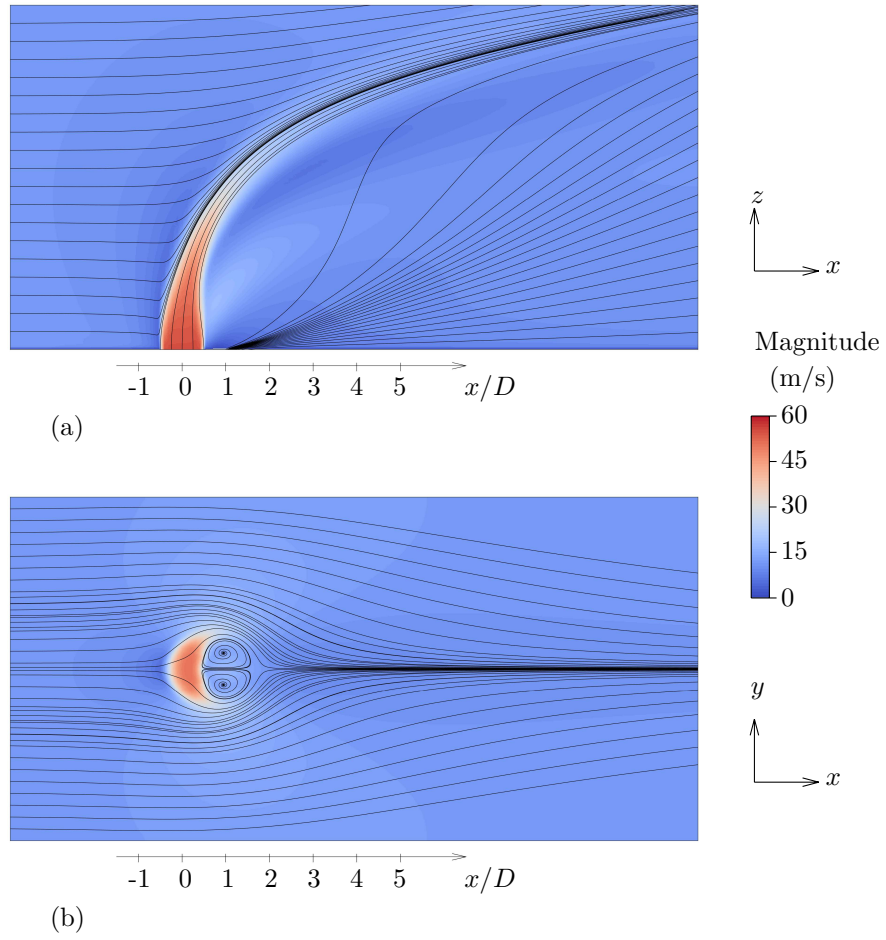

Figure 3.17: Averaged flow field predicted by RANS for increased jet momentum ratio, $q = 21$: (a) side view of the central plane, (b) top view at $z = 5$ mm ($z/D = 0.2$).

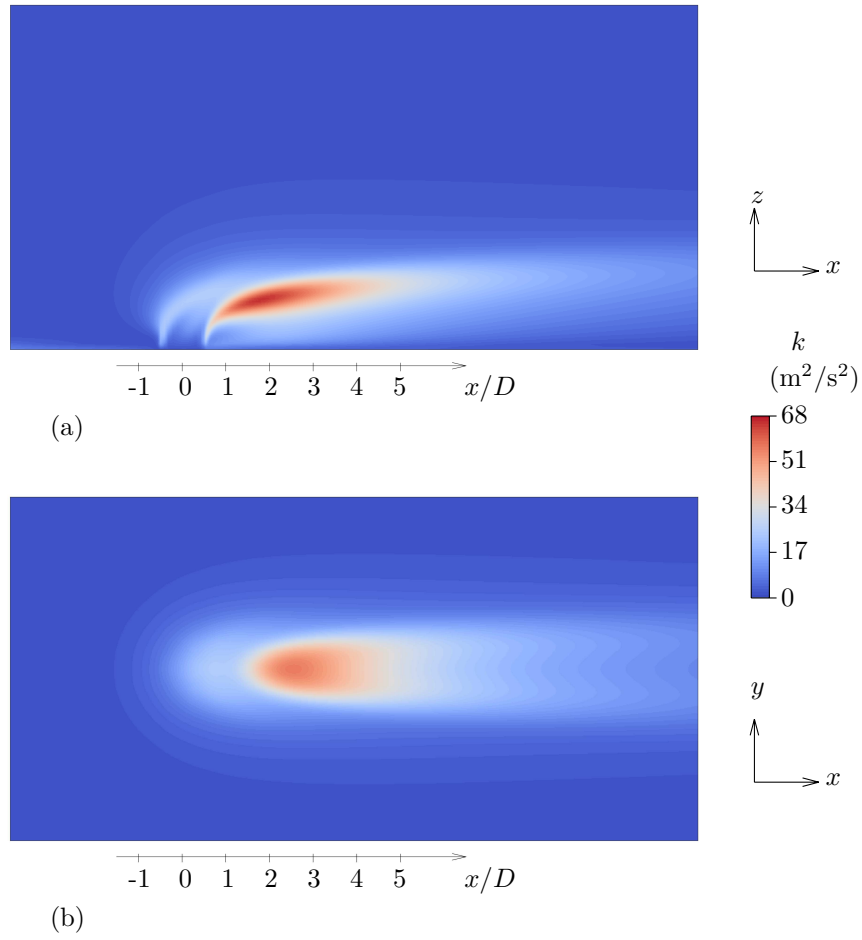

Figure 3.18: Turbulence kinetic energy predicted by RANS for reduced jet momentum ratio, $q = 1.3$: (a) side view of the central plane, (b) top view at $z = 5$ mm ($z/D = 0.2$).

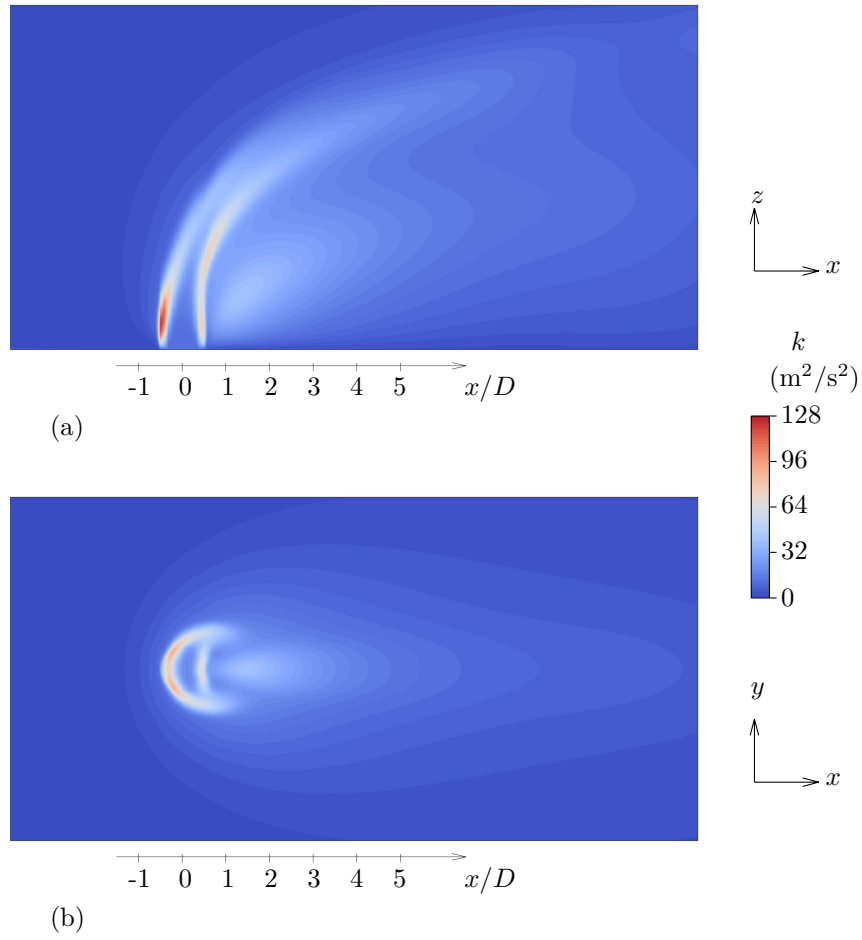

Figure 3.19: Turbulence kinetic energy predicted by RANS for increased jet momentum ratio, $q = 21$: (a) side view of the central plane, (b) top view at $z = 5$ mm ($z/D = 0.2$).

Figure 3.20: Effect of changing momentum ratio on the average x-component of velocity predicted by RANS.

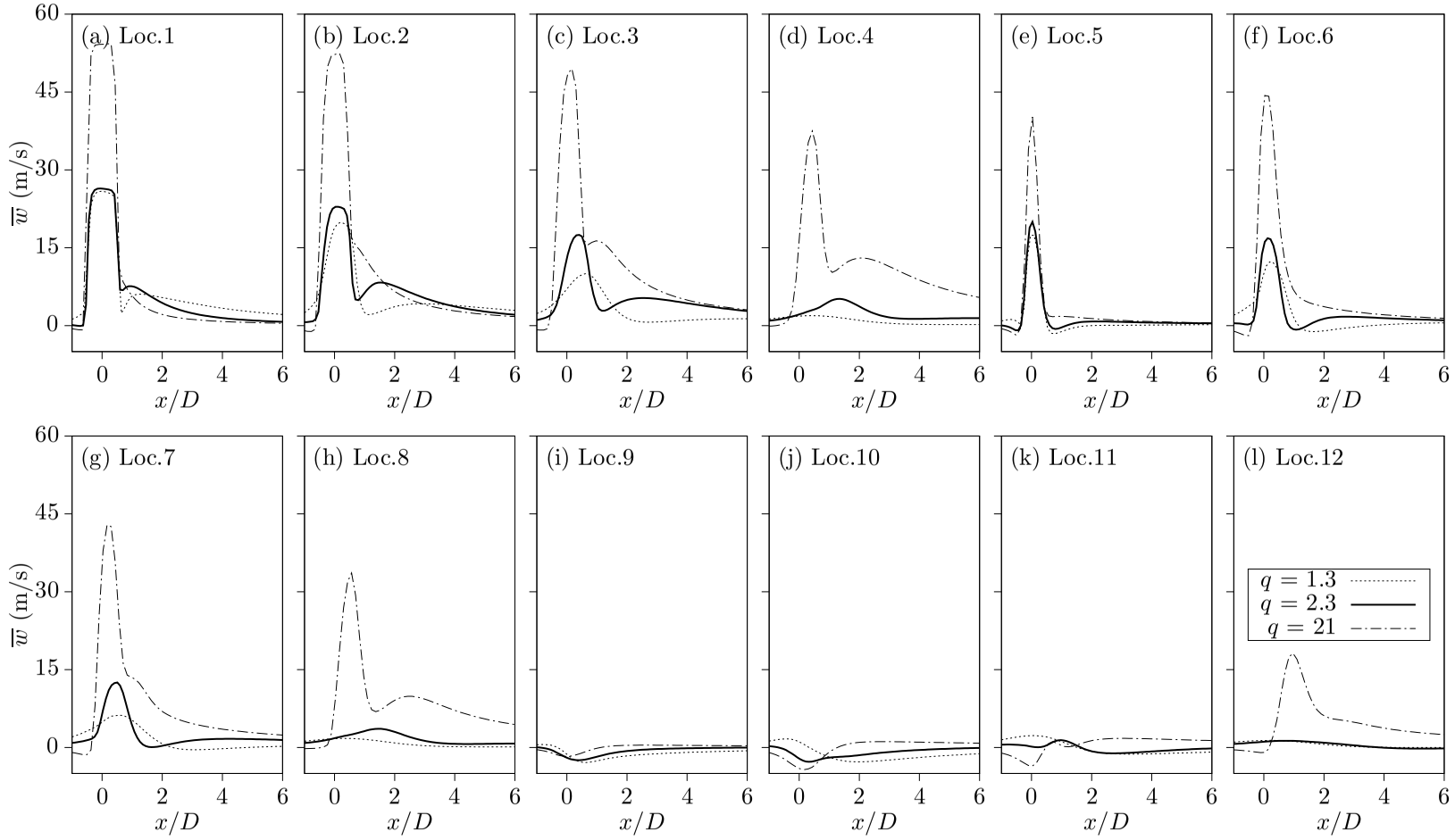

Figure 3.21: Effect of changing momentum ratio on the average z-component of velocity predicted by RANS.

Changing the jet to cross flow momentum ratio produces a visibly different flow structure with a reduction in jet deflection, increased penetration into the cross flow and change in size and magnitude of the recirculation zone. Figures 3.16 and 3.17 also show the differences in jet wake formed by increasing the momentum ratio. The wake size increases in width owing to the increased jet momentum and corresponding change in recirculation zone structure which reduces in length downstream as it attaches to the underside of the jet and is lifted away from the domain floor. This change also affects the turbulence kinetic energy predictions, visible in Figures 3.18 to 3.19, which show the highest energy concentration shifted from underneath the gas jet downstream of the inlet at the top of the recirculation zone toward the rear of the jet. The increased momentum causes an increase in the shear between the cross-flow and jet flow and increases the turbulent energy at the rear of the jet at the point of deflection. This increased intensity does not reduce the intensity of the moved recirculation zone but drastically increases the energy produced by the flow shear leading to steeper velocity gradients and higher peak magnitudes close to the jet inlet.

An increase in the momentum ratio shows several important trends throughout the velocity predictions. The average x component of velocity direction in Figure 3.20 continually predicts the same key features present in the original simulations against the experiments. Notably, the predictions at Location 1 close to the domain floor show all three momentum ratio cases forming the same pattern of a single minimum peak immediately in front of the jet inlet followed by a gradual return to free-stream values. These predictions diverge with an increase in z over Locations 1 – 4 with the 1.3 momentum ratio becoming less distinguishable from the free-stream flow characteristics due to the increased jet deflection. A momentum ratio of 21 shows increasingly turbulent behaviour from Location 3 with higher intensity recirculation along with a rise prior to the inlet upstream. This is a result of the shift in location of the recirculation zone from the lower momentum ratio cases, see Figures 3.16 and 3.17, from close to the floor to remaining attached to the underside of the jet.

The separation between predictions at the floor is more evident from Location 5 onward with a ratio of 1.3 remaining close to the free-stream velocities whereas higher intensity minimum peaks are predicted for q = 21 with a marginal shift

upstream from the original ratio of 2.3 predictions. More than a 50% reduction in magnitude between q = 1.3 and q = 21 is visible at Location 5 far upstream with the difference downstream beyond $x/D = 4$ actually reducing between 6 – 7, owing to the increased downstream presence of the recirculation zone affecting flow velocities. By the outer edges of the flow at Locations 9 – 12 both ratios of 2.3 and 21 continue to exhibit upstream peaks located between $x/D = 0$ to $x/D = 2$, indicating a reducing effect of the gas jet on the outer edges of the flow with 1.3 becoming almost indistinguishable from the free-stream flow by location 12.

The most obvious difference in the average w predictions in Figure 3.21 is the large increase in primary and secondary peak magnitudes for a momentum of ratio of 21 of more than double those of the lower momentum ratios. Whilst the primary peak locations remain upstream between Locations 1 – 8 at $x/D = -0.5$ to $x/D = 0.5$, predictions for momentum ratios of 2.3 and 1.3 remain close together due to an identical jet inlet velocity profile but the lowest ratio of 1.3 shows reducing penetration from a velocity peak drop by up to 40 % from 2.3 at Location 3 along with a downstream shift in it's peak predictions up to $x/D = 0.5$ at locations 3 – 4 and 7 – 8. In addition there is no secondary peak predicted beyond Location 2 due to the recirculation presence close to the floor as a result of increased jet deflection. By the outer edges of the jet at Locations 9 – 11 the effect of the jet on the average flow velocities has reduced substantially and all momentum ratio predictions remain close together, with less than a 3 m/s difference between any profile at at any given distance. Only at location 12 is there a separation by a single large peak for the highest momentum ratio, indicative of the presence of the vortex pair on the outer edges of jet jet flow.

Overall RANS predictions for an increasing jet to cross-flow momentum ratio show a change in flow structure with increasing jet penetration causing a shift in the location of major flow phenomena, moving the recirculation zone higher in the z direction and reducing length which brings the vortex pair further upstream and increasing shear at the rear of the jet inlet due to the increased jet momentum. The greatest kinetic energy concentration also shifts toward the rear of the jet from the recirculation zone at low momentum ratios and peak magnitudes become more pronounced for all velocity components, however the steady-state nature of

the calculations prevents analysis of the remaining small scale turbulent flow phenomena.

LES Results

All figures are generated from instantaneous time step results files with all graphical data appropriately time averaged, see Section 2.1.2 for details.

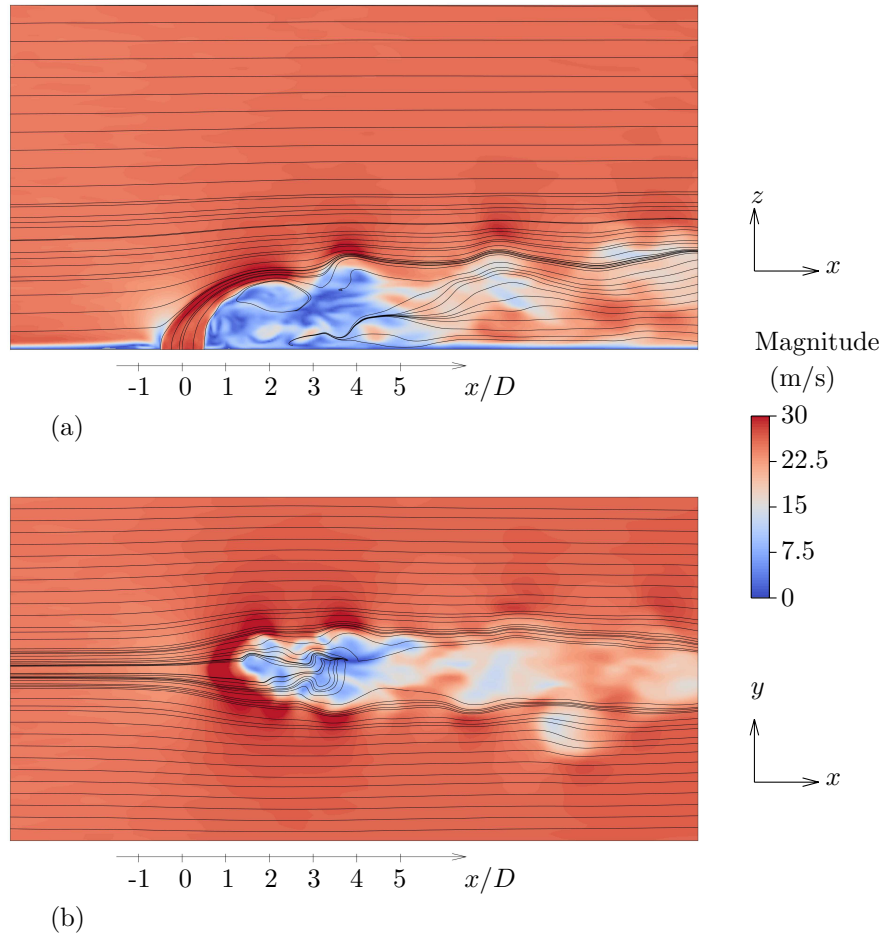

Figure 3.22: Instantaneous flow field predicted by LES for reduced momentum ratio, $q = 1.3$: (a) side view of central plane, (b) top view at $z = 5$ mm ($z/D = 0.2$).

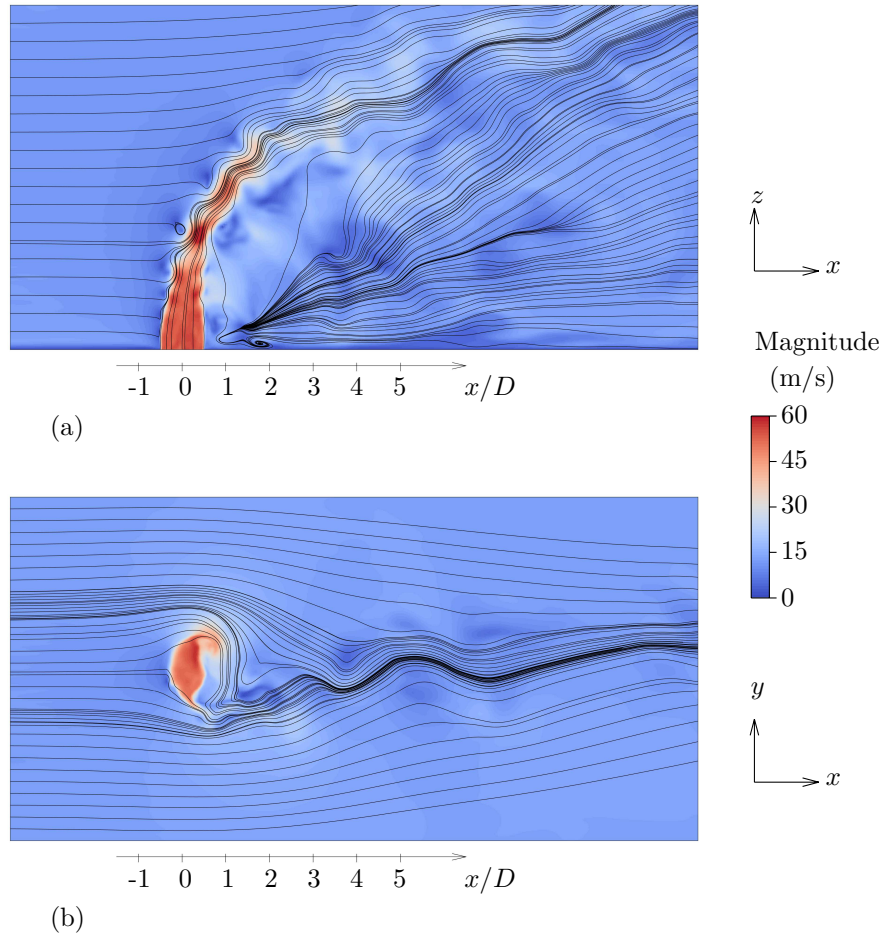

Figure 3.23: Instantaneous flow field predicted by LES for increased momentum ratio, $q = 21$: (a) side view of central plane, (b) top view at $z = 5$ mm ($z/D = 0.2$).

Figure 3.24: Effect of changing momentum ratio on the average x-component of velocity predicted by LES.

Figure 3.25: Effect of changing momentum ratio on the average z-component of velocity predicted by LES.

LES analysis of an increasing jet to cross-flow momentum ratio presents a number of similarities to the RANS equivalent analysis, but are also able to account for additional turbulence effects due to the dependence on time. Figures 3.22 and 3.23 illustrate an increase in the turbulent nature of the flow and retaining the major features predicted in the RANS simulations. The streamlines given an indication of the most turbulent regions of the flow being $x/D = 1$ to $x/D = 5$ for the lowest momentum ratio whilst this shifts further downstream for the highest ratio with the turbulence underneath the jet still affecting the velocity predictions up to $x/D = 10$ by which point the lower ratio flow characteristics are comparable to that of the free-stream flow. Despite this, the region very close to the domain floor remains largely unaffected beyond $x/D = 3$. This is visible in the wake profiles for both momentum ratios where the downstream streamline gradients are much lower than those predicted immediately around the jet inlet with relatively little deflection for both cases despite the differences in flow profiles.

The average LES u predictions in Figure 3.24 are most turbulent at the domain symmetry plane, inferred by the increased number of small peaks near the jet inlet not present in the RANS predictions. An increase in momentum ratio shifts the maximum peak locations upstream by $x/D = 0.5$ from the lowest ratio of 1.3 to 21 due to the alteration in jet structure visible in Figures 3.22 and 3.23. With the turbulent wake shifting from close to the ground to the underside of the jet, this region still retains a high level of turbulence until $x/D = 0.4$ where the majority of predictions resume close to the free-stream values. At the rear of the jet inlet there is a predicted velocity increase before the steep gradient reduction which is not predicted for any of the RANS simulations - but was present for the experimental data in Section 3.2.2; this remains present until Location 8 for the higher momentum ratios. As with RANS the lowest momentum ratio becomes dominated by the free-stream flow beyond a certain height, predicting very low gradient changes across the measurement regions but also predicting the highest upstream peak magnitudes close to the floor along with the steepest profile gradients as the magnitude tends to the free-stream value. Another difference between the RANS and LES predictions are the notable peaks present on the outer measurement regions between Locations 9 – 12 for all momentum ratios,

indicating the presence of small-scale turbulence on the outer edge of the jet, likely to correspond to the small horseshoe vortexes which are not predicted by RANS.

An expected peak rise at the highest momentum ratios for w is repeated in the LES predictions in Figure 3.25 along with the secondary downstream peak formation at $x/D = 1.0$. However the separation between low momentum ratio predictions increases over RANS with 1.3 moving more than a full diameter downstream in peak position by Location 3. Each secondary peak retains a magnitude of less than 10 m/s along with a reduction in minimum peak value with an increasing momentum ratio due to the shift in recirculation area. Although broadly similar to the RANS predictions and less turbulent than Locations 1 – 4, the predictions in Locations 5 – 8 all indicate an increase in downstream turbulence between $x/D = 2$ to $x/D = 4$ with large increases in velocity gradients associated with greater turbulent energy. As with the u predictions, the vortex pair formation is presented at Location 12 with a peak magnitude and gradient increase with the lower momentum ratios remaining close to 0 due to the influence of the free-stream flow. However the differences between momentum ratio predictions are greater than that of RANS with up to 5 m/s between Locations 10 – 11 at peak separation along with the primary peak predicted at Location 9, accounted for in the previous Section.

The main difference as a result of method change from RANS to LES is the effect of the superior turbulence predictions on the velocity gradients, particularly close to the domain floor and the upper jet surface where the small scale turbulence flow features exhibit the greatest effect. These predictions signifying that small scale turbulent flow features may have a significant effect on the predictions even at the outer edges of the jet; however they may be for different phenomena as only the highest momentum ratio exhibits evidence of the vortex pair although both lower ratios may predict turbulence accounted for by vortex shedding. Differences in the jet penetration are also present, with LES predicting an increase over the RANS simulations up to Location 9; although this is most significant between Locations 5 – 7 with up to a 10 m/s increase.

It is possible to conclude that for an increasing jet to cross-flow momentum ratio there are a number of similarities between prediction methods which re-

flect the changing flow structure. With increasing momentum the jet penetrates further into the free-stream, reducing the deflection and increasing the z RMS stresses around the jet inlet. This is accompanied by the upstream shift of the average velocity peaks owing to the change in recirculation zone structure as it reduces in length and moves off the floor as it remains attached to the underside of the gas jet. With this comes an increase in the resulting shear at the rear of the jet which in turn shifts the greatest concentration of turbulent kinetic energy within the domain from the recirculation zone to the rear of the gas jet as the cross-flow is deflected and the wake begins to form as visible in Figures 3.22 and 3.23. However as with the modelling against experimental data in the previous section it is LES which provides the superior turbulence prediction with increased gradients indicating the presence of vortex pair and vortex shedding which RANS is unable to predict.

3.3 Summary

Simulation results show that RANS predictions obtained using OpenFOAM and Ansys CFX with standard settings are very similar for a jet in cross flow, with the only differences occurring in the turbulence kinetic energy. This shows that both packages are capable of handling the prediction of a jet in cross flow, which is one of the canonical test cases for turbulence models.

Comparison with experimental data using multiple CFD methods provides a reasonable match, concluding that when using a 'flat' velocity profile it is the LES approach which provides the superior match with greater jet penetration but performed less well than expected given the higher grid resolution with under-predicted RMS stresses. The accurate capturing of the jet inlet velocity, either (as here) by imposing the measured inlet profile or by simulating the flow inside the jet upstream of the inlet (as Majander and Siikonen (2006)) is shown to improve the RANS predictions with better jet penetration over the original 'flat' profile. LES predictions would likely improve with the addition of a profiled inlet velocity.

Changing the jet to cross flow momentum ratio leads to a significant change in the flow structure. An increase in jet penetration leads to reduced jet deflection and a shift in kinetic energy concentration due to increasing shear. Lower

momentum ratios exhibit steep velocity gradients close to the domain floor but are influenced heavily by the cross flow on the upper edge of the jet which reduces the turbulence. Higher momentum ratios shift the locations of the large scale flow features, shifting the vortex pair downstream and increasing the shear at the rear of the jet inlet. Both RANS and LES predicted the same large scale flow features and exhibited similar peak locations for all momentum ratios but the LES approach also suggested small-scale turbulence having an effect on the flow within the recirculation zone.

The RANS approach is less accurate than LES but requires fewer computational resources and is still capable of predicting the major features of a jet in cross flow, particularly with the application of a profiled inlet velocity. Therefore RANS provides a sufficient basis to continue with the application of atomization and vaporization modelling in the next chapter.

Chapter 4

Σ–Y_{liq} Simulation of a Liquid Jet in Cross Flow

Following on from the gas jet simulations presented in Chapter 3, the Σ–Y_{liq} model was implemented into a commercial CFD package, ANSYS CFX, and used to predict the droplet SMD for a liquid jet in cross-flow. A range of cross-flow and liquid jet velocities are tested and the effects of cross-flow velocity and momentum ratio are examined along with the ability to predict an average vaporization rate at both high and low gas temperatures.

4.1 Numerical Setup

The experimental data was obtained from Becker (2004) in which the liquid droplet SMD was measured 80mm downstream of a circular liquid jet inlet, normal to an air cross-flow in a rectangular channel using Laser Doppler Anemometry (LDA).

The biggest change from the RANS domain in the gas jet simulations was the diameter of the liquid inlet, now changed to better represent an industrial liquid injector with a 0.225 mm radius. A tetrahedral mesh was chosen to better represent the volumetric propagation of a jet around the liquid inlet. This region is refined by specifying a set of high density cell volumes, as shown in Figure 4.1, and multiplying the cell density. In order to obtain a suitable grid resolution to ensure independence from the cell size, multiple regions were refined with an

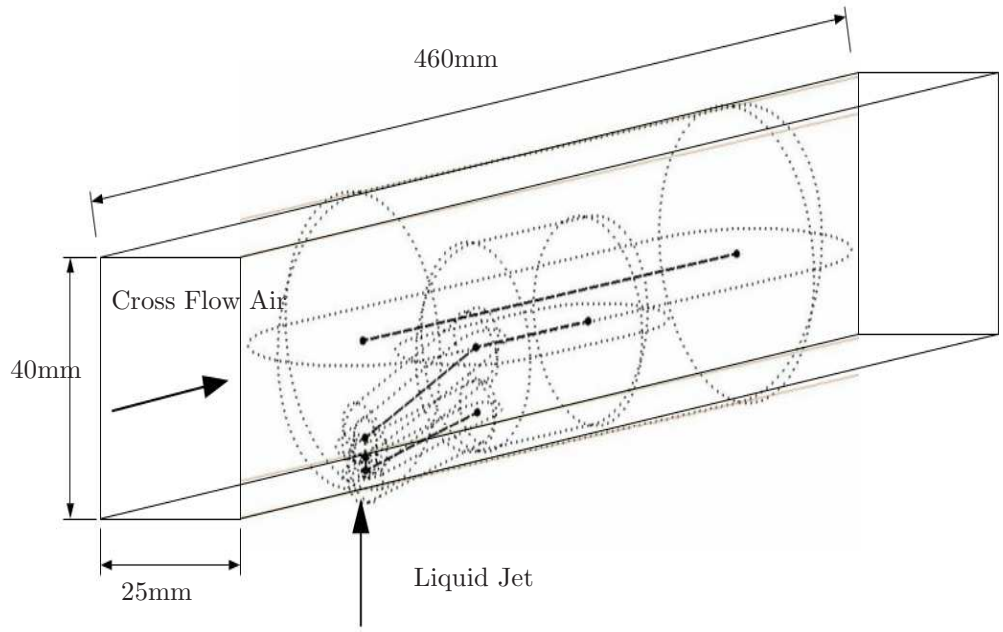

Figure 4.1: Computational domain for liquid jet simulations.

increased density ratio over the standard cell size. Typical cell sizes ranged from 0.85 - 0.36 mm in the less refined areas further downstream beyond $x = 80$ mm and a magnitude of 0.22 mm in the refined central region. Minimum cell sizes were present close to the liquid jet inlet with a value of 0.0225 mm.

The measurement points from the original experimental data in Becker (2004) were only at a single location, 80 mm downstream from the liquid jet inlet. To better reflect the development of the jet due to its formation and evolution from a single boundary condition rather than a pre-defined spray pattern from liquid lance data, a number of additional measurement locations are specified between the centre of the jet inlet and the maximum downstream measurement point at $x = 0$ mm, 20 mm and 40 mm.

In addition to these measurement points, contour plots of the various results fields are taken to give an overview of the key jet features away from the domain centreline.

Four different cases are studied, two different cross-flow velocities are used with four different jet speeds, depending upon the chosen momentum ratio. All simulations are conducted with a liquid density of 780 kg/m^3 and a gas density of 7.2 kg/m^3. This represents Jet-A in liquid and vapour forms. Only a small temperature difference is assigned between the liquid and gas, which is at 298K.

The case I.D. in Table 4.1 consists of 3 parts, 'U' refers to the cross flow velocity in m/s, 'P' the pressure, all of which were 6 bar and 'Q' to the jet to cross flow momentum ratio; defined in Eq. (2.30).

Table 4.1: Liquid jet cases studied by Becker (2004).

Case I.D.	Air Inlet (m/s)	Fuel Inlet (m/s)
U75P6Q2	75	10.7
U75P6Q6	75	18.6
U100P6Q6	100	24.8
U100P6Q2	100	14.3

Experiments were conducted at an operating pressure of 6 bar. The k–ω–SST model was chosen to model turbulence due to its increased ability to predict in regions of very high shear, in particular for this case, including the area in front of the jet inlet. Turbulence intensity is set at 5 % to ensure a reasonable representation of turbulence within the flow.

The nature of the conditions required for the model, regardless of the individual case conditions, is always identical as Σ is dependant upon the geometry, whereas Y_{liq} and Y_{vap} are set at 1 and 0 at the liquid inlet, respectively. The assumption being that a solid liquid jet was occupying the entire inlet area and any fuel vapour formed would do so due to the heat transfer, only once the liquid had entered the domain and not in the fuel supply itself. At all other locations these values were set to 0 whereas the solid walls are modelled using a no-flux condition.

The first value of Σ for the liquid jet boundary was calculated at 30 m^2/kg and is only applicable to Section 4.2.1 after which the new assumptions in Section 2.4.3 and Eqn. 2.51 were used and a new value of 55 m^2/kg was assigned for all

future tests. The following table lists the total CPU hours and individual CPU s/itr/core for all simulations presented within this Chapter:

Table 4.2: CPU hours and individual CPU s/itr/core.

Case	CPU s/itr/core	CPU hours
Boundary - original	3.12	23.2
Boundary - large annulus	18.9	48.2
Boundary - small annulus	9.21	25.4
Boundary - profiled	21.7	48.1
U75P6Q2	5.71	89.3
U75P6Q6	5.83	113.3
U100P6Q6*	7.84	71.3
U100P6Q2	5.81	75.2
Vapour - 300K	6.98	118.8
Vapour - 650K	7.13	46.1

* U100P6Q6 results are identical to Boundary - profiled but the table values take into account the CPU time of the initial solution used to obtain this result.

Table 4.2 shows that the time penalty for the addition of the vaporization mechanism to the model on an identical mesh is of the order of 20 % with the average CPU s/itr/core rising from approximately 6 to 7 s; this is a relatively small increase considering the number of additional terms which are required.

4.2 Atomization

Initially an atomization only version of the Σ–Y_{liq} model was utilised as the experimental data was from a 'cold flow' where no vaporization occurred and the average temperature was well below the fuel boiling point. The atomization-only version differs from the full version as the transport equations for fuel contain no source terms as it is assumed that no vapour is produced regardless of the temperature. The minimum numerical bounding for the presence of fuel in a cell (Y_{liq}) was 1 $\times 10^{-5}$, ensuring that no artificial behaviour was produced from the manipulation of small numerical values. In addition, the upper boundary for SMD was set at 0.45 mm to ensure that no excessive numerical values were produced immediately above the jet inlet. The success of the model is determined by the accuracy of the SMD prediction downstream, provided that no abnormal behaviour was present in the predictions.

4.2.1 Sensitivity to Σ Boundary Condition

In order to test the boundary assumptions described in Section 2.4.3 a series of simulations were conducted using the setup conditions listed in Table 4.1 corresponding to U100P6Q6 with the liquid inlet structure altered, see Figure 2.4, and compared the original approach to those using the new boundary condition assumptions.

Table 4.3: Inlet boundary conditions for Σ.

	Δr (mm)	Σ_0 (m^2/kg)
Original	0.225	30
Large Annulus	0.045	55
Small Annulus	0.0225	110

The following results illustrate the effect of each of the previously described sets of boundary conditions set up using the conditions listed in Table 4.1. Each was compared to a baseline case using the original boundary assumptions detailed in Sidhu and Burluka (2008).

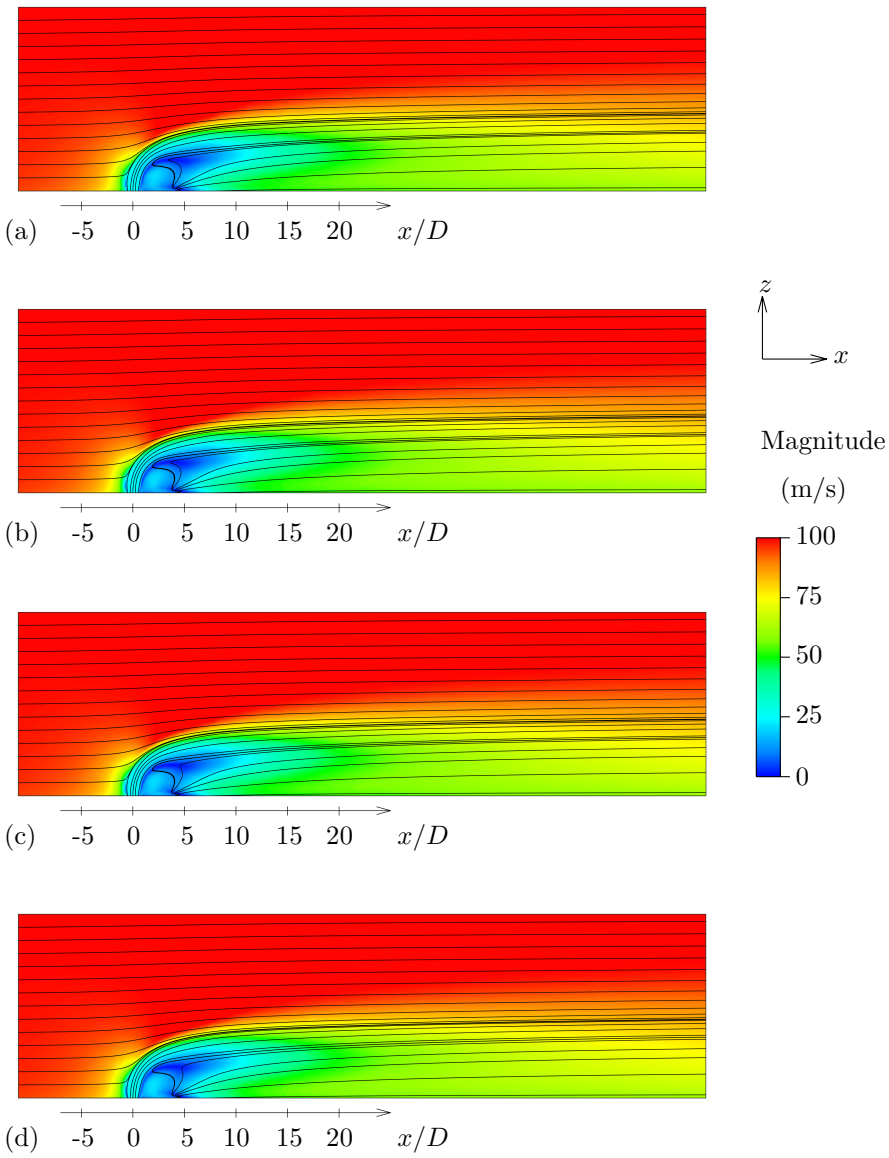

Figure 4.2: Average flow field in the central plane for U100P6Q6: (a) original Σ boundary condition, (b) large annulus, (c) small annulus, (d) large annulus with profiled jet velocity.

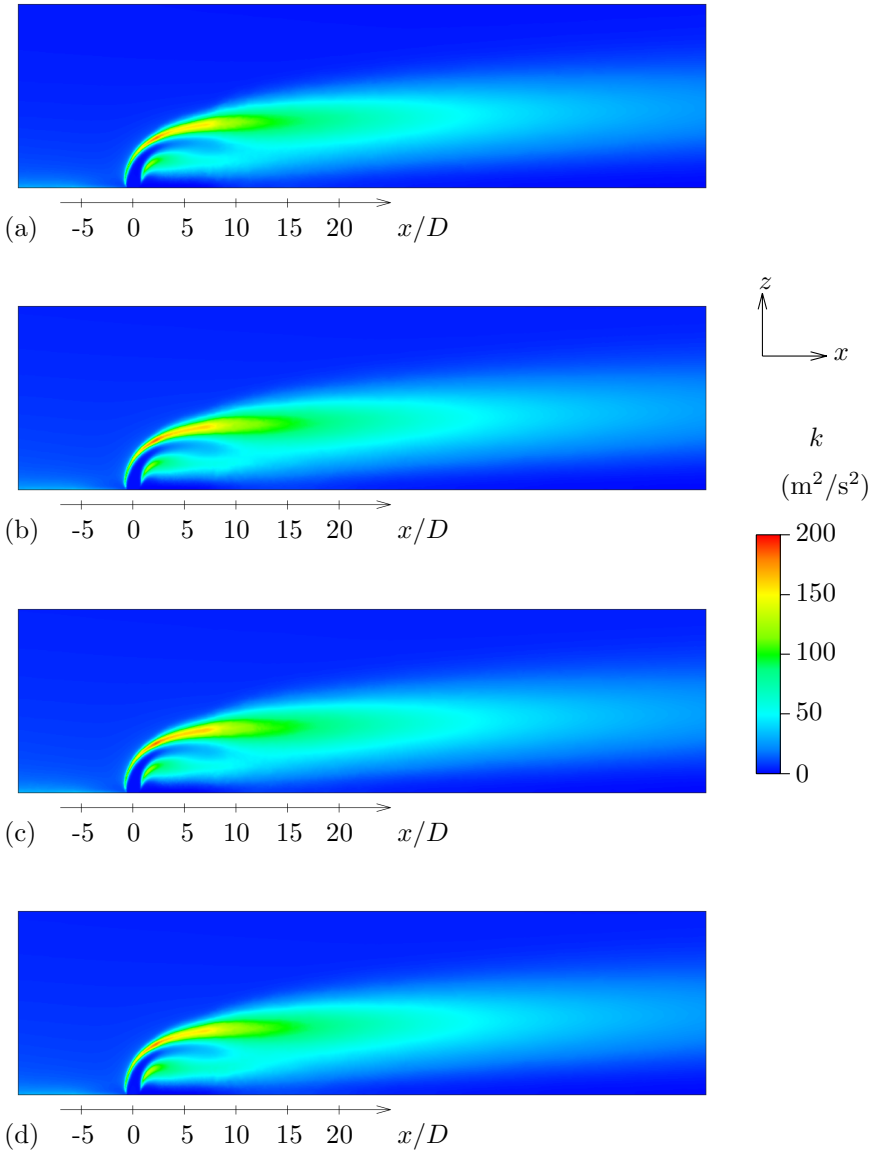

Figure 4.3: Turbulence kinetic energy in the central plane for U100P6Q6: (a) original Σ boundary condition, (b) large annulus, (c) small annulus, (d) large annulus with profiled jet velocity.

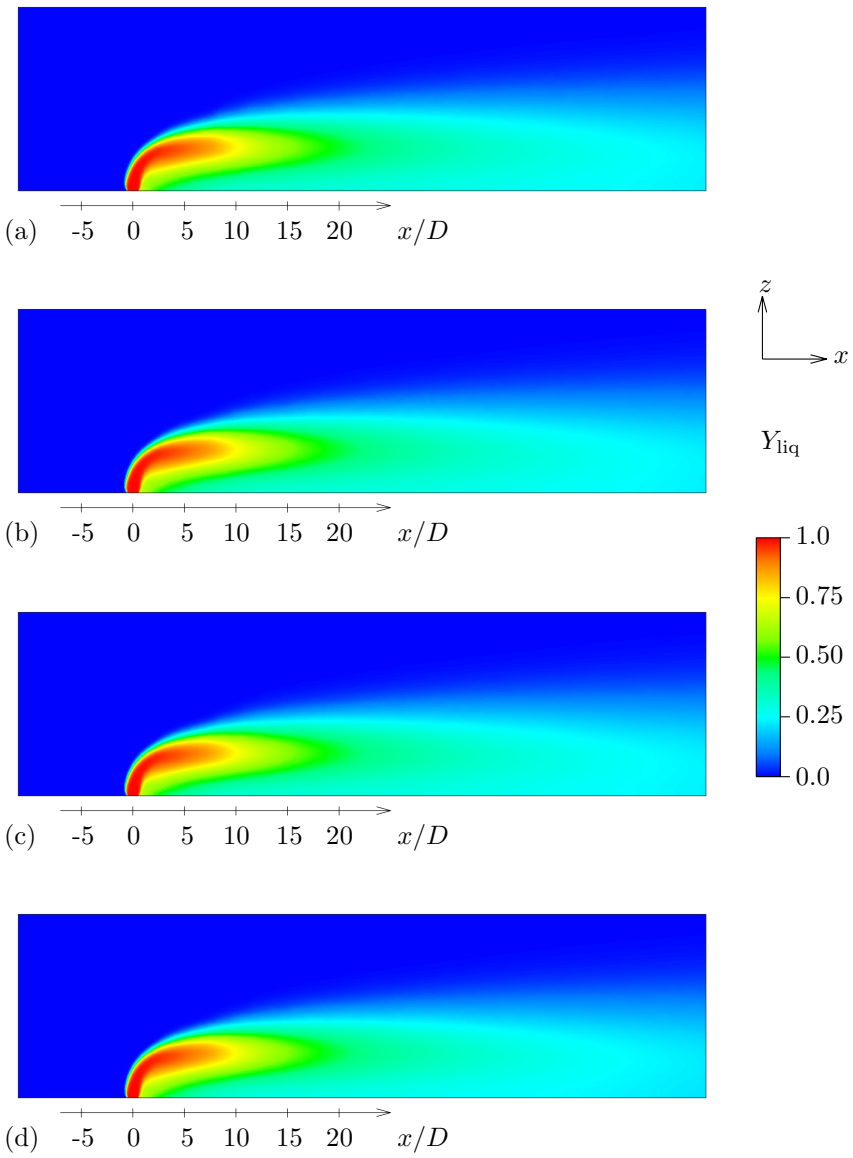

Figure 4.4: Average mass fraction of liquid in the central plane for U100P6Q6: (a) original Σ boundary condition, (b) large annulus, (c) small annulus, (d) large annulus with profiled jet velocity.

The various inlet parameters ranging from the velocity to the average surface area per unit mass are displayed in Figures 4.2 to 4.8. With no change in the velocity boundary characteristics between the original approach and first fuel ring test, the velocity magnitude and turbulence kinetic energy predictions in Figures 4.2 and 4.3 remain almost identical. Although the Σ predictions have altered, it is the liquid mass fraction which affects the average density; independent of Σ for atomization due to the absence of any source terms. Initially the shift from the original calculation for Σ at the boundary to the new 'fuel ring' assumption shows a significant reduction in the peak value in the presence of Σ immediately above the jet inlet. This is due to the removal of the assigned inlet value across the majority of the fuel surface and instead only represents the diffusion present on the outside of the inlet, see Figure 4.6.

The effect of this change upon SMD ,which is dependent on both Y_{liq} and Σ, was notable with the maximum magnitude above the jet inlet increasing, reaching orders of magnitude above the original values for a few cells; visible in Figure 4.7. This finding resulted in a numerical bounding condition being applied for all subsequent simulations, limiting the maximum value of SMD to the diameter of the liquid inlet with the assumption that the liquid jet would only reduce in diameter due to breakup immediately outside of the inlet boundary. An additional separation between SMD predictions in the downstream region is also predicted from this change with the newer assumptions predicting up to 75 microns above the original at 20 mm, gradually falling to approximately 10 microns at a distance of 80 mm. This is likely due to the reduction in Σ concentration downstream beyond $x/D = 10$, with the reducing of liquid concentration from the centre effectively reducing presence close to the floor - which would increase in the droplet SMD.

The reduction in Δr illustrated in (c) of each result plot predicts very little change to any of the quantity fields from (b), the only notable difference is the formation of a small group of larger diameter droplets in the SMD, visible in Fig 4.7, on the rear of the jet; a result of the decrease in inlet cell size which predicts additional droplet presence at the jet edge due to a reduction in velocity magnitude which limits the turbulence and therefore reduces breakup. However this has little effect on the downstream field predictions with the difference in

SMD less than 5 microns by $x/D = 80$ mm, resulting in a very similar prediction to the larger annulus cell size.

This cell size reduction did not have an effect on the velocity or turbulence fields, nor on the fuel distribution around the inlet. However the Σ predictions show a small change above the inlet with an increase in high magnitude concentration between $x/D = 0.5$ and 3. The appearance of a small peak at $x/D =$ -0.5 is also a result of the reduced cell size which increases the initial boundary value of Σ but decays at the same rate as the velocity profile over the inlet remains identical to (b) and the primary breakup mechanism is dependent upon flow turbulence. This lack of effect on the SMD demonstrates that Eq.2.51 is independent of the boundary cell size used to determine the dimensions of the fuel rings, therefore it is acceptable to use a size best suited for mesh quality, ideally of a similar dimension to those on the liquid surface, without having to compromise mesh surface structure due to extremely small cell sizes.

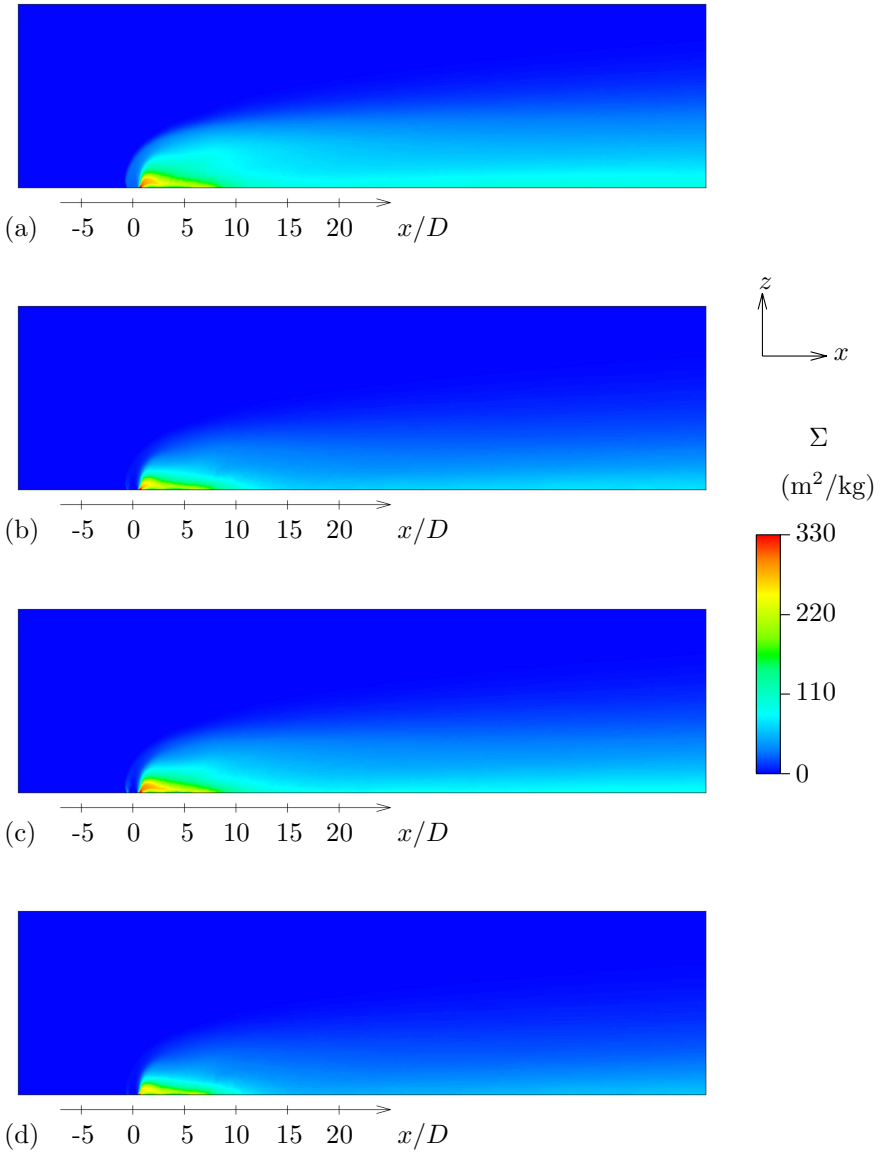

Figure 4.5: Average Σ in the central plane for U100P6Q6: (a) original Σ boundary condition, (b) large annulus, (c) small annulus, (d) large annulus with profiled jet velocity.

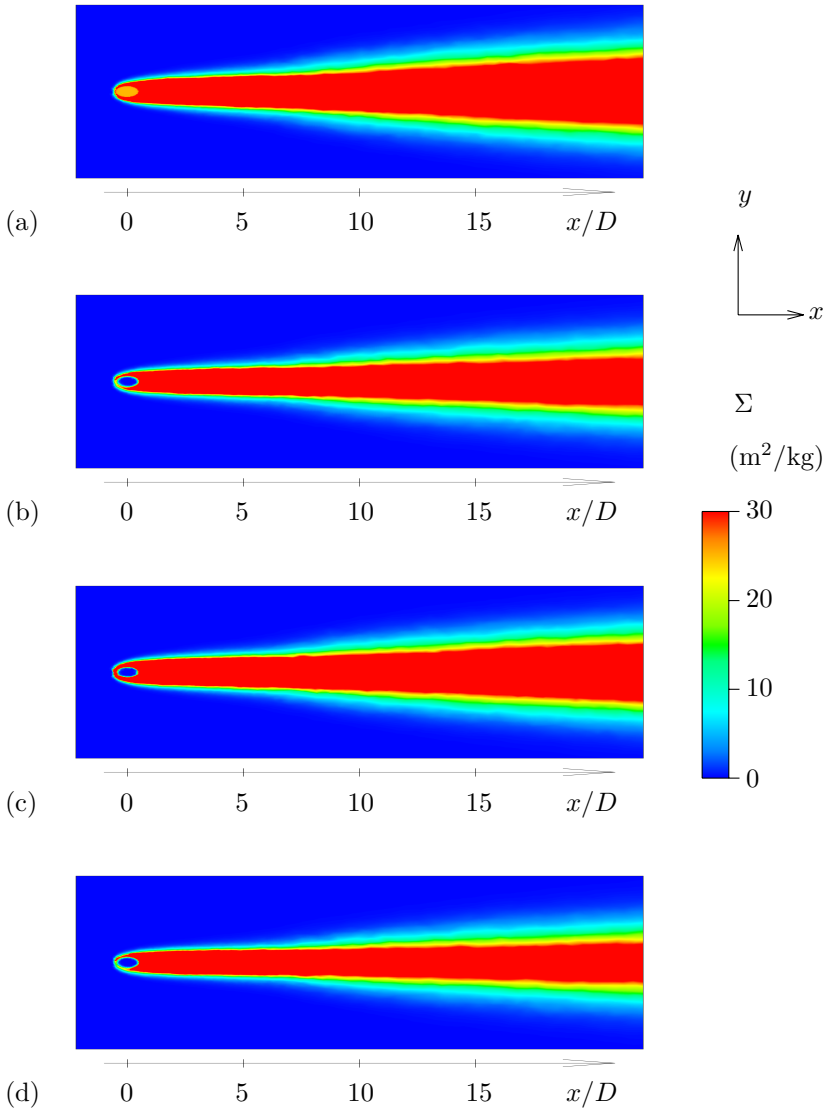

Figure 4.6: Top view of average Σ immediately above the jet inlet for U100P6Q6: (a) original Σ boundary condition, (b) large annulus, (c) small annulus, (d) large annulus with profiled jet velocity.

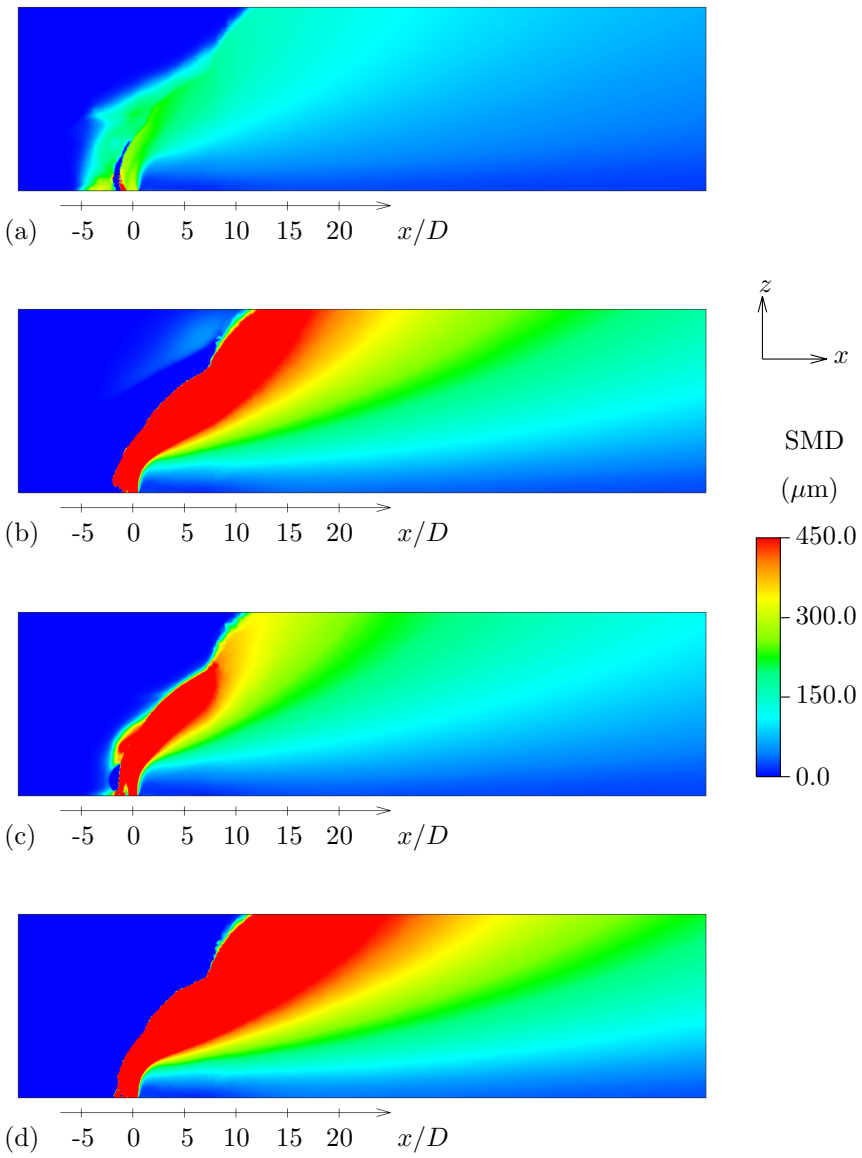

Figure 4.7: Predicted SMD of droplets in the central plane for U100P6Q6: (a) original Σ boundary condition, (b) large annulus, (c) small annulus, (d) large annulus with profiled jet velocity.

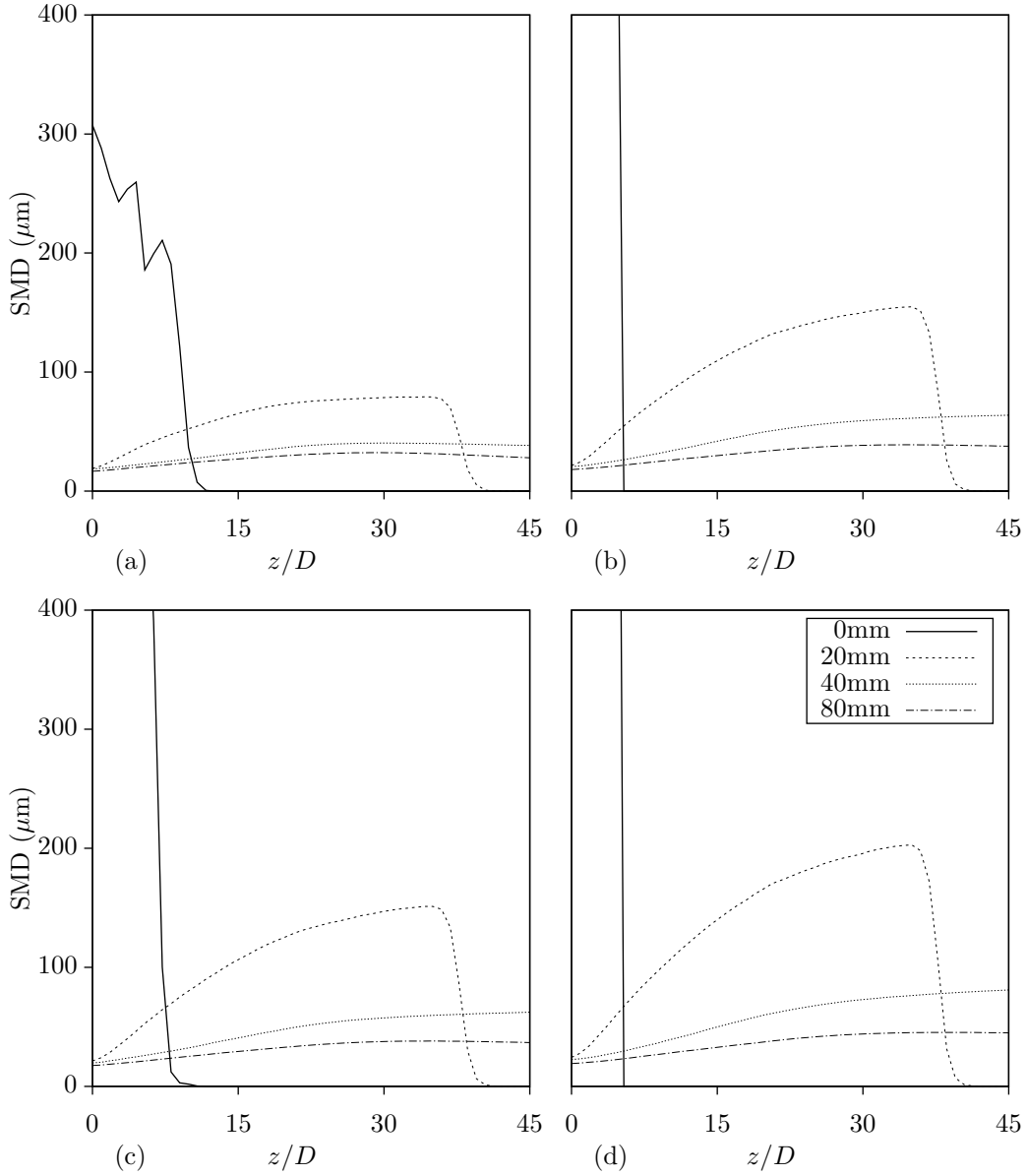

Figure 4.8: Predicted SMD of droplets in the central between $x = 0 - 80$ mm for U100P6Q6: (a) original Σ boundary condition, (b) large annulus, (c) small annulus, (d) large annulus with profiled jet velocity.

Profiling the velocity components to resemble a turbulent pipe flow upon entry to the domain alongside the new assumption for Σ resulted in a number of key differences which had an effect on both the fuel distribution and SMD values. Both the velocity and turbulent kinetic energy predictions increase at the centre of the liquid inlet, causing a slight shift in the recirculation zone structure, visible in the streamlines in Figure 4.2 between $x/D = 3$ to 5, although the turbulence profile still predicts the highest energy concentration on the upper surface of the jet due to the shear against the cross flow air. However the effect on the Σ distribution is a result of the lower velocities predicted at the inner and outer fuel rings due to the assumed 'pipe' flow profile, in turn the average surface area decreases due to the majority of the surface area predictions now being present at the front of the jet rather than evenly distributed combined with the lower velocity and reduced turbulence energy - shifting the highest concentration closer to the domain floor in a pattern reminiscent of that predicted for (b). The biggest difference is the increased region size of the largest droplets, see Figure 4.7, which shifts the entire concentration further into the domain, suggesting the presence of groups of larger droplets penetrating further into the free-stream at the inlet, resulting in a further increase in downstream SMD up to 45 microns by 80 mm.

The spread between each of the SMD predictions at the measurement positions also increases, with the upstream predictions for location 2 in Figure 4.8 more than double those predicted by the original boundary condition. By 80mm downstream the magnitude has reduced significantly and well within the expected values provided by the experimental data (discussed in Chapter 4.2.2). This trend is also present in the Σ predictions where location 2 differs from previous simulations with a reduced peak magnitude and a steeper gradient as the field tends to zero, but is a close match to the other boundary methods further downstream.

From these results it was possible to conclude that the application of a profiled velocity was particularly important to the liquid concentration predictions of the average droplet surface area. The profiled velocity boundary at the liquid inlet provided a more realistic profiling of the flow, in addition the larger droplets SMD are observed closer to the floor than the original assumption along with an increased jet penetration for larger droplets but which did not have a significant effect on the total liquid mass fraction distribution. These predictions better

represent some of the expected flow features for a liquid jet in cross-flow than the original predictions, see Section 2.2, as a result the application of a profiled velocity and new Σ boundary conditions were used for all forthcoming liquid simulations.

4.2.2 Validation

The change in free-stream velocity and its effect on SMD is tested in the first half of this section, where two different momentum ratios are tested for each cross flow air velocity. The aim of this is to determine the effect of the momentum ratio on the model predictions independently of the change in cross-flow air velocity. A total of four separate simulations were carried out, two at the previous momentum ratio of $q = 6$ and two with a reduced momentum ratio of $q = 2$. Table 4.1 contains notations and conditions for each case tested.

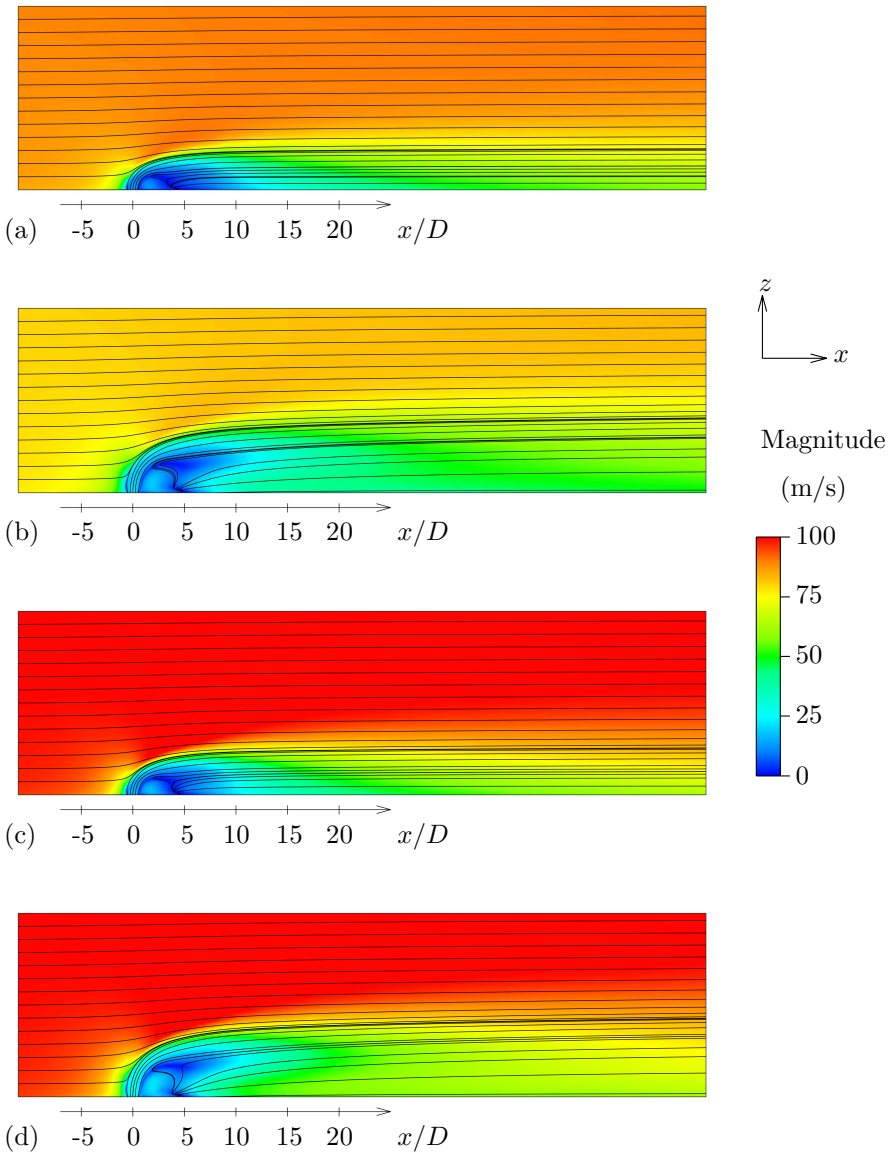

Figure 4.9: Average flow field in the central plane: (a)U75P6Q2, (b)U75P6Q6, (c)U100P6Q2, (d)U100P6Q6.

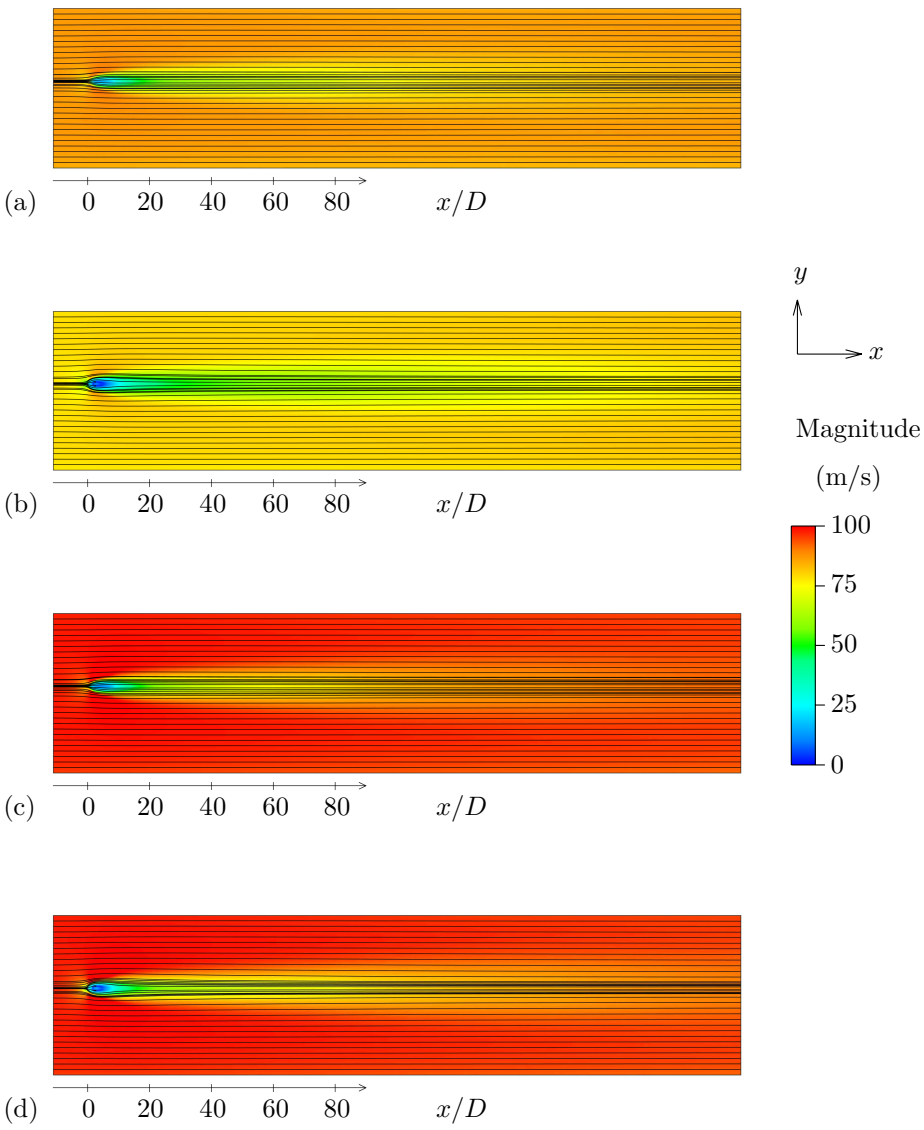

Figure 4.10: Top view of the average flow field at $z = 1$ mm ($z/D = 2.2$): (a)U75P6Q2, (b)U75P6Q6, (c)U100P6Q2, (d)U100P6Q6.

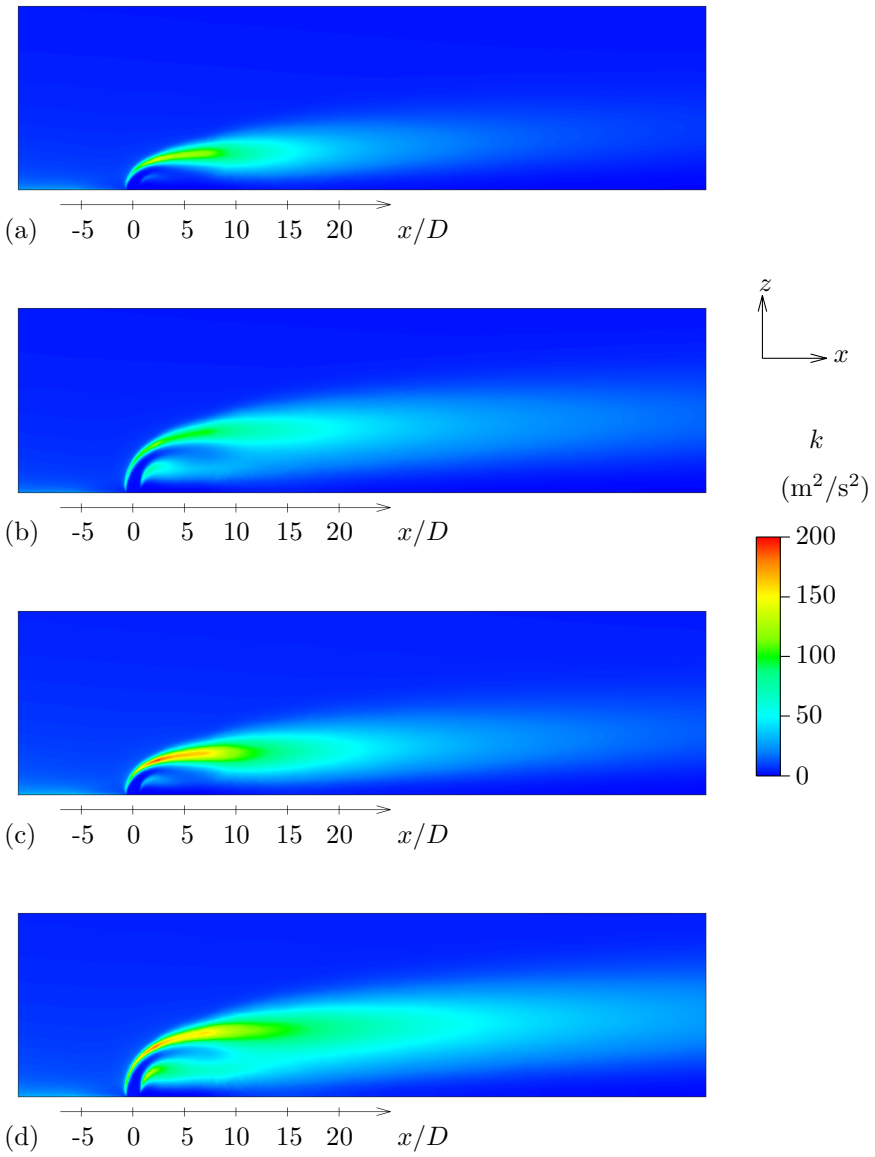

Figure 4.11: Turbulence kinetic energy in the central plane: (a)U75P6Q2, (b)U75P6Q6, (c)U100P6Q2, (d)U100P6Q6.

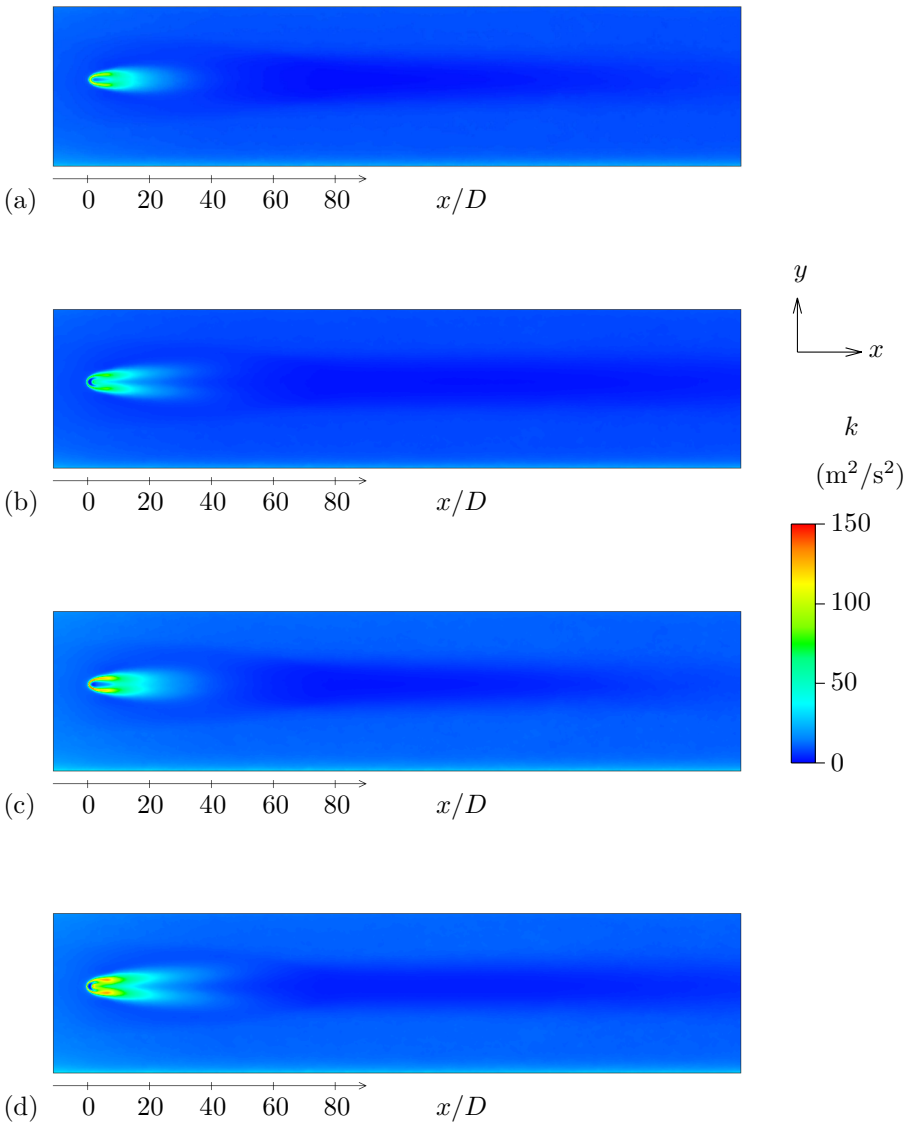

Figure 4.12: Top view of the turbulence kinetic energy at $z = 1$ mm ($z/D = 2.2$): (a)U75P6Q2, (b)U75P6Q6, (c)U100P6Q2, (d)U100P6Q6.

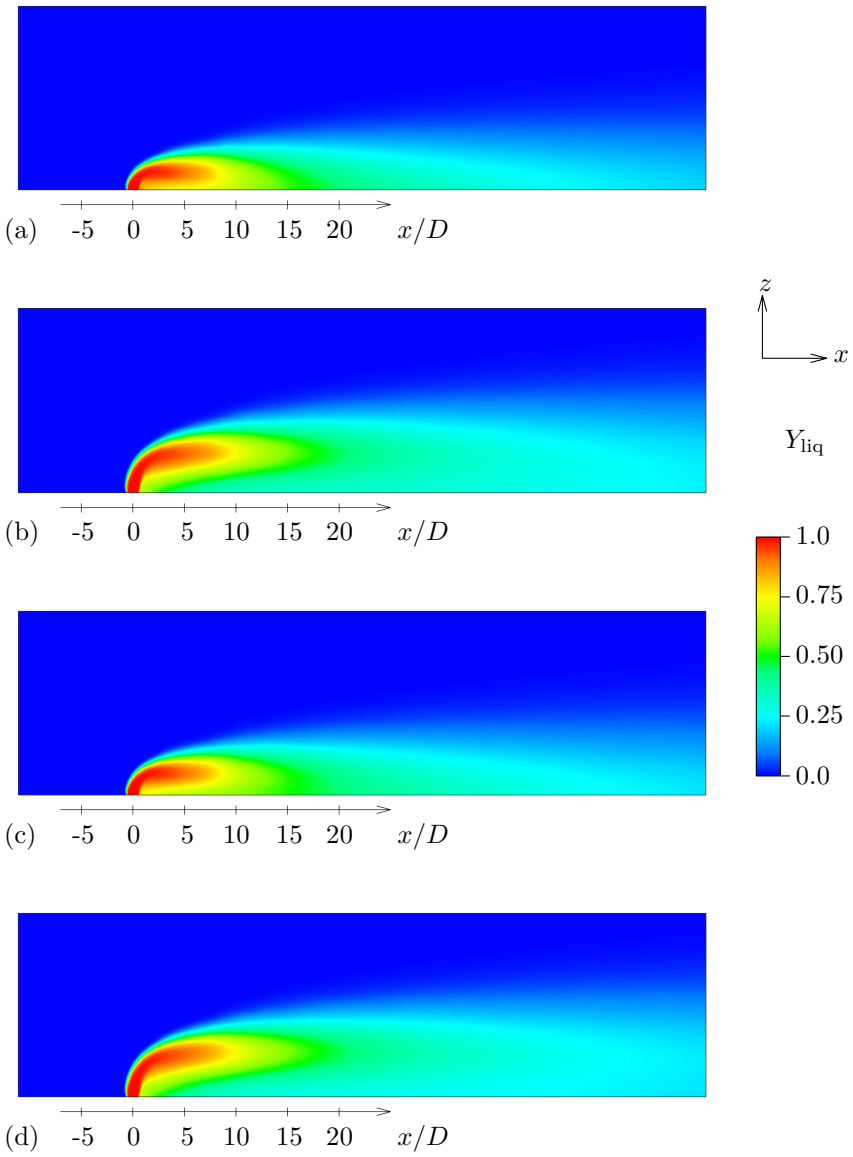

Figure 4.13: Average liquid mass fraction in the central plane: (a)U75P6Q2, (b)U75P6Q6, (c)U100P6Q2, (d)U100P6Q6.

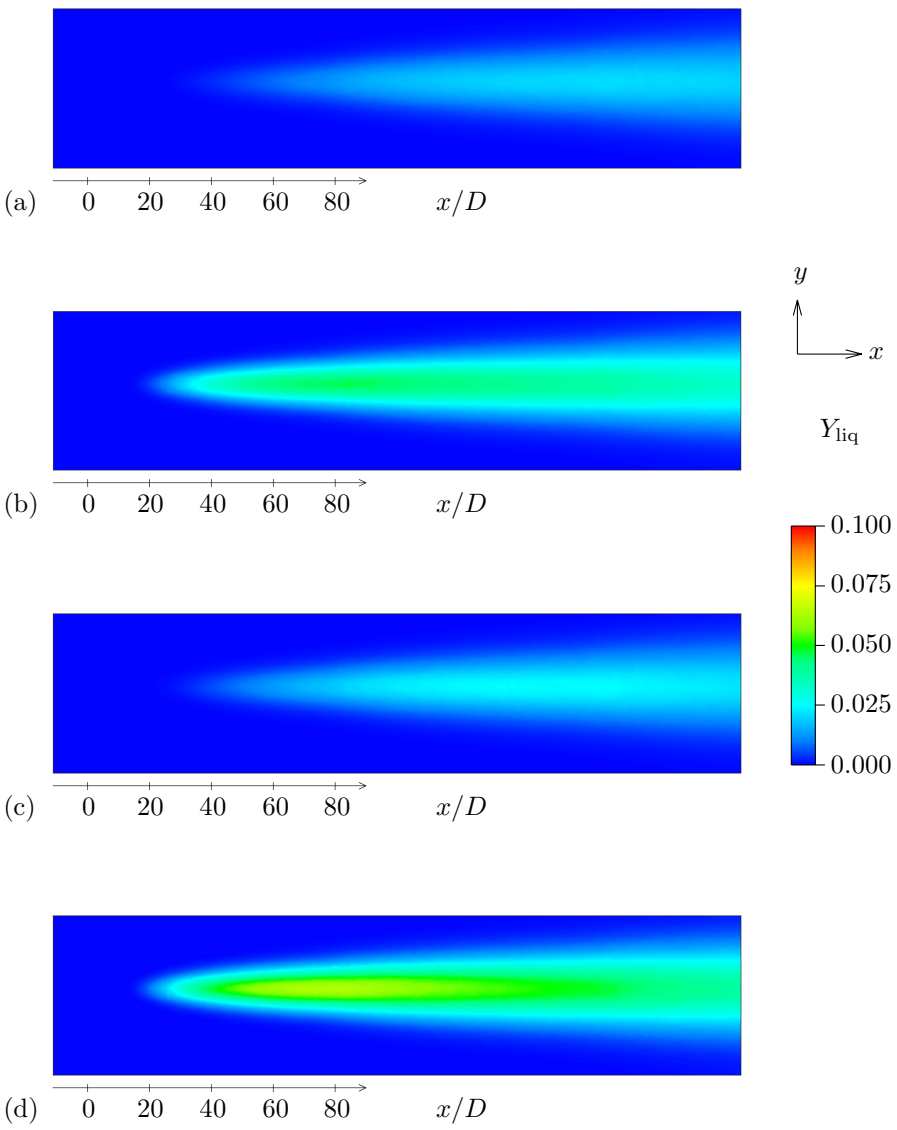

Figure 4.14: Top view of the average liquid mass fraction at $z = 5$ mm ($z/D = 2.2$): (a)U75P6Q2, (b)U75P6Q6, (c)U100P6Q2, (d)U100P6Q6.

The examination of increasing momentum ratio for two different cross-flow velocities enables a range of comparisons to be made regarding the flow characteristics and the corresponding velocity field prediction changes. Reasonable changes can be observed in the velocity magnitude in Fig 4.9 with the low momentum ratios for both velocities in (a) and (c) predicting a large increase in jet deflection from the cross flow, reducing the penetration, as the jet velocity is reduced. Another important feature is the presence of the recirculation zone, characterised by a region of low or negative velocity in front of the jet inlet close to the domain floor. The higher momentum ratio cases predict a slight increase in size of this region in the z direction over the lower momentum ratio cases along with a lower velocity magnitude on the underside of the liquid jet. In addition, the streamlines show that the higher momentum ratio cases also take longer to resume the free-stream values beyond the recirculation zone. Despite these small differences, the overall deflection of the jet caused by the free-stream remains very similar, depending upon the momentum ratio, with the liquid jet acting as barrier, forming a wake downstream of the jet. This is visible in Figure 4.10 which illustrates these wakes, where the width of the wake is dependent upon the cross-flow velocity and momentum ratio. An increased jet velocity reduces the wake width closer to the floor as the flow structure moves in the z direction but it is mainly the increase in cross flow velocity which reduces the width at the same momentum ratio; increased flow acceleration is also visible either side of the liquid inlet where the bulk flow is deflected by the liquid.

The turbulent kinetic energy predictions, shown in Figure 4.11, are split into two regions for the low momentum ratios in (a) and (c) with high magnitude regions only on the upper side of the jet whilst both higher momentum ratios exhibit regions of high kinetic energy within the recirculation zone as well. The cross flow velocities in (c) and (d) increase the turbulent kinetic energy on the upper surface of the jet as a result of the increased shear close to the jet inlet, downstream beyond $x/D = 20$ the difference in peak magnitudes is reduced which suggest that when the jet is aligned with the free stream due to deflection the shear between the two flows is reduced.

The predictions in the xy-plane close to the flow in Figure 4.12 support these predictions with (a) and (b) exhibiting lower peak magnitudes and the high mag-

nitude 'U' shape only visible in (c) and (d) around the rear and sides of the inlet due to the shear increase between the two flows. Despite this, patterns dependent upon the momentum ratios are still present with the concentration separating into 2 components either side of the symmetry plane for (b) and (d) whilst the concentrations remains in a single area between $x/D = 0$ to 20.

These predictions from the continuity and turbulence equations have a subsequent effect on the liquid mass fraction predictions by the Σ–Y_{liq} model in Figure 4.13. The liquid fuel mass fraction, Y_{liq}, predicts a solid central core immediately above the inlet which is gradually deflected by the free-stream, the liquid breakup accounts for the high reduction in magnitude by $x/D = 10$ to less than 0.5 in Figure 4.13. The difference in momentum ratio accounts for both the increase in jet height downstream and penetration with the high momentum ratios in (b) and (d) retaining a higher concentration of fuel further downstream than the low ratio predictions. Since this field is heavily dependant upon the flow velocity, it is expected that the fuel jet predictions will be closely matched to those of the profiles in Figure 4.9 close to the jet inlet whilst diffusion accounts for the higher liquid spread far downstream.

Figure 4.14 illustrates this in the xy-plane where (b) and (d) show magnitudes almost twice that of the lower momentum ratios in (a) and (c) despite an almost identical width in the y direction. This is due to the difference in jet penetration shifting the jet central axis in the z direction, having the effect of increasing the downstream concentration above the floor, however beyond $x/D = 20$ the overall magnitude of the mass fraction within this region is less than 0.1; indicating significant breakup by this point. In addition, the increasing cross flow velocity appears to have little effect on the total width of the jet, but does increase the peak magnitude between $x/D = 40$ to 80 for (d), however it is the momentum ratio which is primarily responsible for the liquid jet behaviour when not considering vaporization.

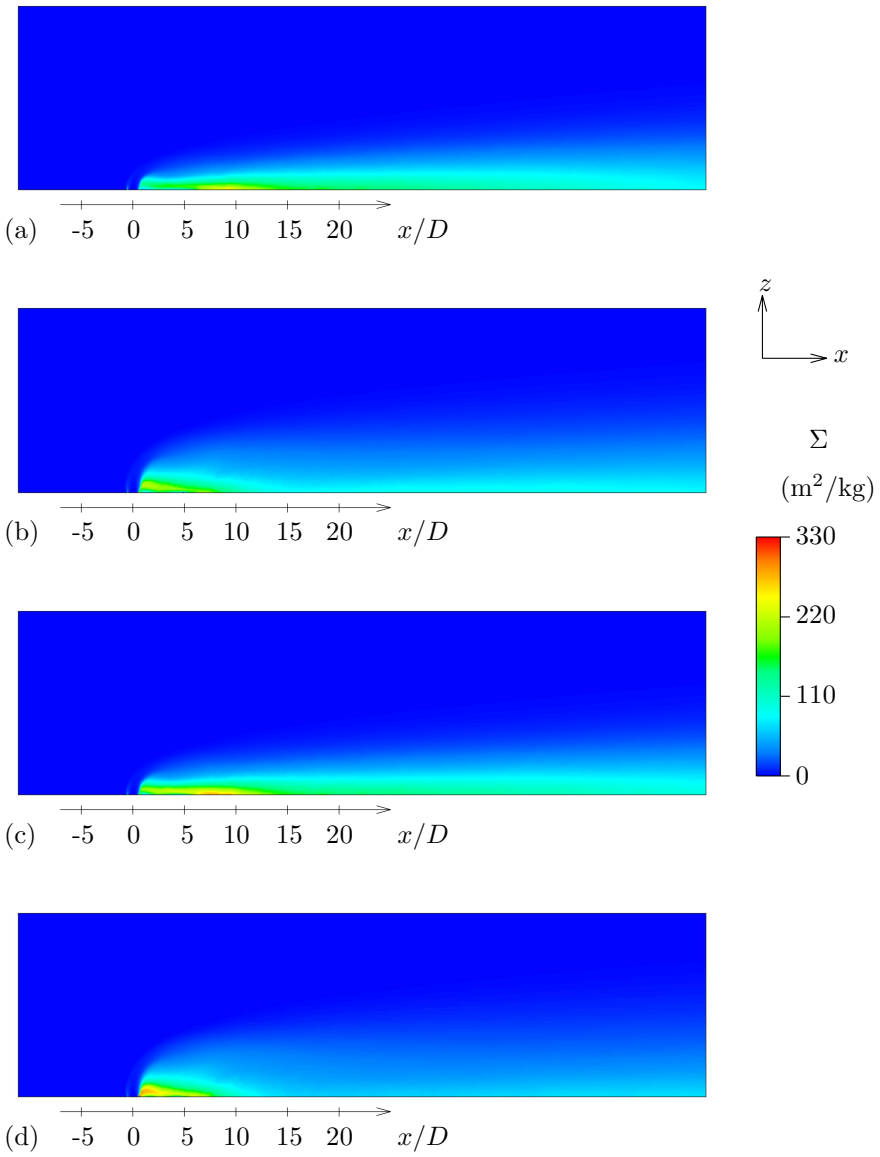

Figure 4.15: Average Σ in the central plane: (a)U75P6Q2, (b)U75P6Q6, (c)U100P6Q2, (d)U100P6Q6.

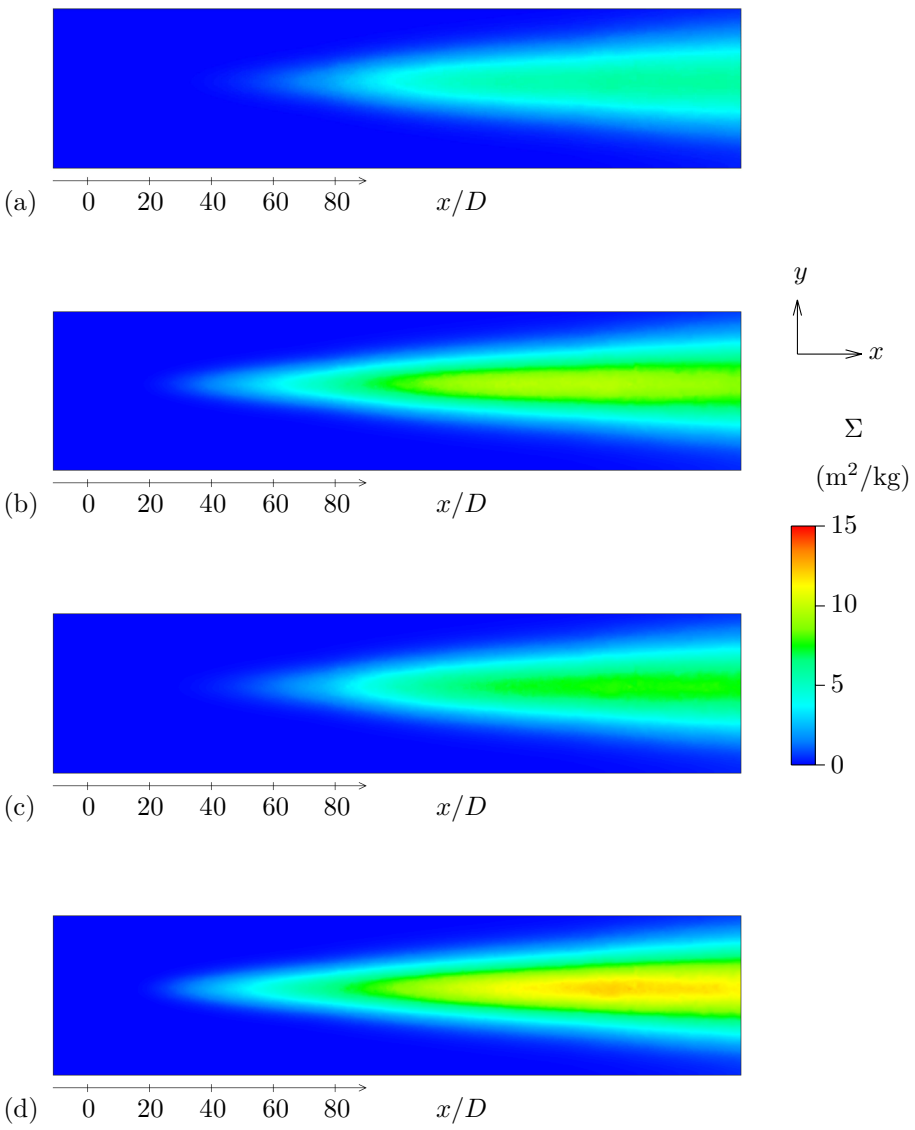

Figure 4.16: Top view of average Σ at $z = 5$ mm ($z/D = 11.1$): (a)U75P6Q2, (b)U75P6Q6, (c)U100P6Q2, (d)U100P6Q6.

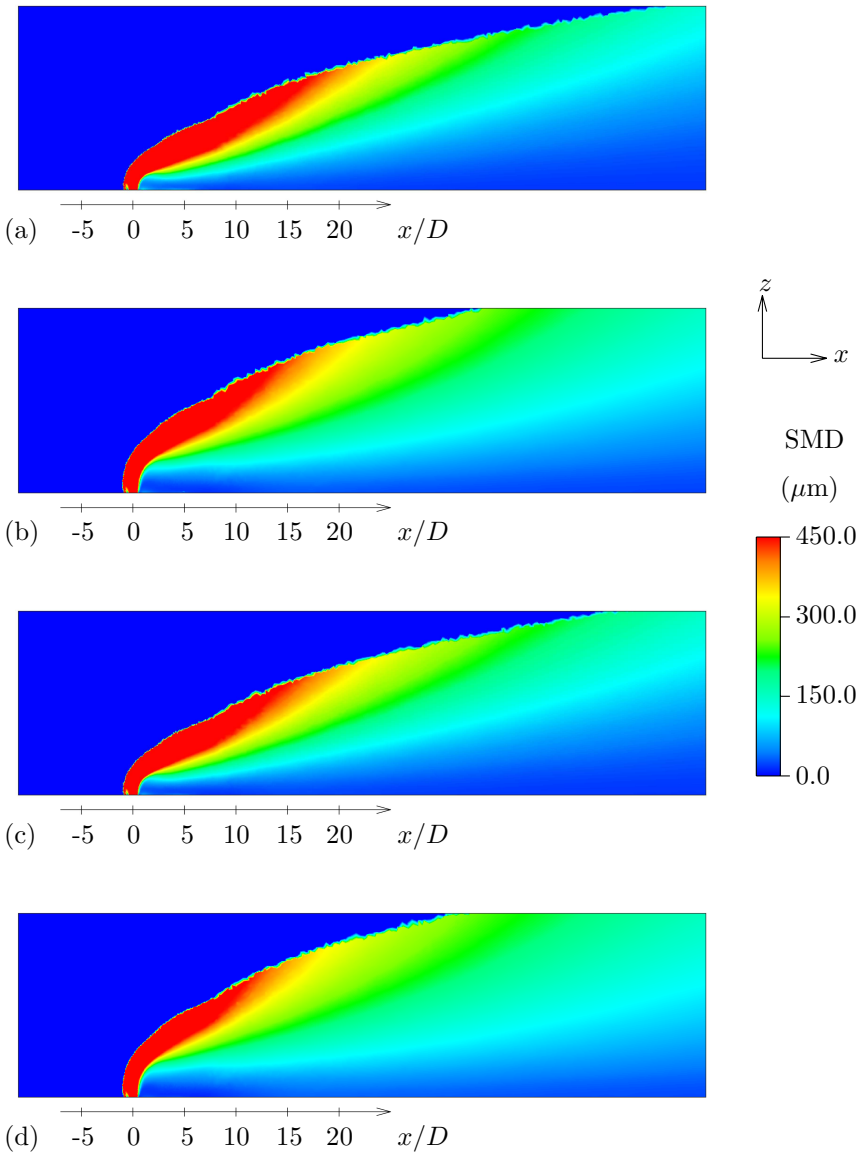

Figure 4.17: Predicted SMD of droplets in the central plane: (a)U75P6Q2, (b)U75P6Q6, (c)U100P6Q2, (d)U100P6Q6.

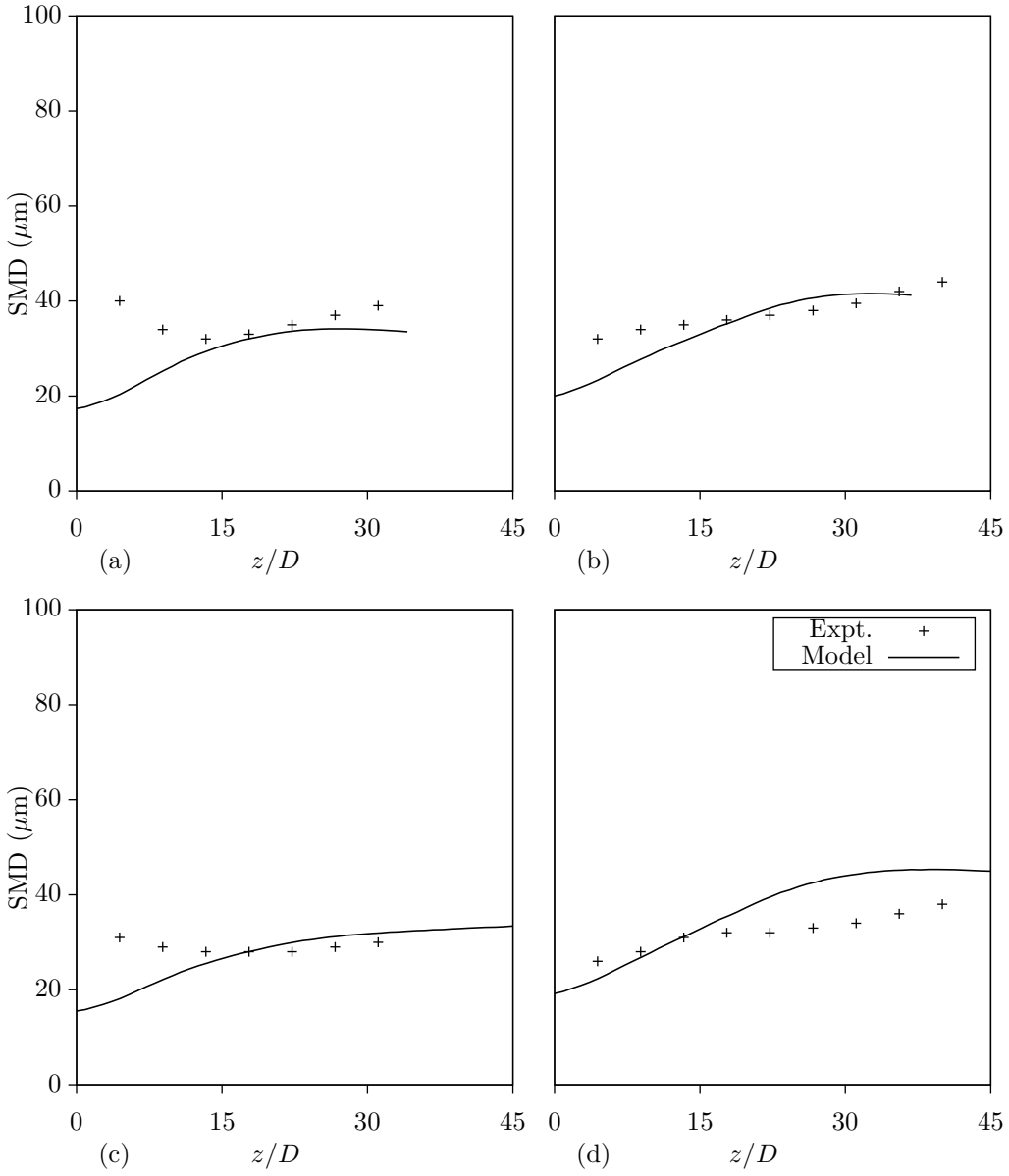

Figure 4.18: Predicted and measured SMD at $x = 80$ mm ($x/D = 178$): (a)U75P6Q2, (b)U75P6Q6, (c)U100P6Q2, (d)U100P6Q6.

Droplet equilibrium radii for high and low momentum ratios cases predict the primary concentration directly above the jet inlet, deflected in a similar fashion to that predicted for the liquid mass fraction with a lower magnitude secondary concentration of larger droplets present above the upper envelope of the jet. Since Eq. 2.38 is dependant upon flow turbulence, this concentration is a result of the shear breakup on the upper surface, as indicated by the turbulent kinetic energy in Figure 4.11. This results in a very similar prediction for all simulations and the resultant equilibrium surface area calculated from these droplet radii influences the rate of surface generation in Σ as a result of the global turbulence.

Predictions for Σ exhibits several key characteristics. The first is the uneven distribution on either side of the liquid inlet with the rear of the jet predicting only a small magnitude and concentration, as shown in Figure 4.15. This is due to the imposing of the novel Σ boundary condition which only assigns a value of Σ to the outer surface of the jet. At the rear, the liquid jet interacts heavily with the cross-flow air, effectively forcing the liquid concentration downstream or in the y direction as the jet acts as a barrier which forms a wake flow behind it; shifting the region of greatest concentration toward the front of the jet. The second is the dissimilar prediction at the floor depending upon momentum ratio. Lower ratios in (a) and (c) produce an almost even concentration in both magnitude and height well beyond $x/D = 20$ whilst (b) and (d) illustrate both a higher concentration in both magnitude and size up to $x/D = 15$ after which the concentrations drops to less than that predicted by (a) and (c), indicating a reduction in larger droplets within this region. Further downstream, Figure 4.16 shows a similar cone pattern prediction for all cases due to increasing droplet presence near the floor with distance downstream, but with a rising magnitude in the central region beyond $x/D = 100$ for higher momentum ratios representing an increase in larger droplets collecting within this area; possibly as a result of the liquid jet further breaking up past this point due to the mass fraction drop visible in Figure 4.14. With a more uniform distribution with height further downstream, the average surface area per unit mass suggests that the majority of surface area formation occurs between $x/D = 0$ – 20 for the higher momentum ratios, extending to $x/D = 40$ for lower velocities in keeping with the regions of highest liquid concentration and turbulent energy.

The droplet SMD in Figure 4.17 shows a large region of high magnitude droplet sizes present in the highest concentration of liquid above the jet inlet up to the bounding value of 0.45 mm. This gradually decreases with downstream distance, the largest droplets continuing to be predicted beyond the upper envelope of high liquid concentration up to $x/D = 20$ tending toward 0 by the domain floor. Gradually, a more even distribution of sizes occurs downstream as the breakup tends toward secondary atomization as a result of shear away from the primary zone close to the inlet. This suggests that the droplet size concentration is more evenly distributed downstream for a lower cross-flow velocity whilst a higher velocity promotes greater break-up but also allows larger droplets to penetrate further into the bulk flow, increasing the maximum SMD predictions; but only by a small magnitude.

The SMD predictions demonstrate a good agreement in comparison to the experimental data, in particular for the higher cross flow velocities. The overall range of SMD predictions remains below 50 μm for all simulations and both higher momentum ratio cases successfully predict the continuous increase in droplet size with the domain height. Individually, the prediction for U75Q6 represents the best overall match, see Figure 4.18, whilst U100Q6 over predicts downstream up to 10 microns past $z/D = 15$ but drops to 5 microns by the end of the measurement region; however it presents a better match close to the domain floor. This region between $z/D = 0$ - 10 is of import for both lower momentum ratio cases as the simulations fail to predict the sudden rise in droplet size close to the wall, instead forming a continuous decrease in diameter close to the wall as with both the higher momentum ratio cases. One possibility is the coalescence of liquid within this boundary region due to the slower downstream transport and reduced turbulence as a result of the lower velocities which may not be captured by the RANS modelling, although the significant mesh refinement in this area should prevent any adverse effects from the wall functions. Phenomena such as wall-wetting may also occur, this gives rise to the possibility of adding boundary conditions to the domain solid walls for Σ and Y to improve SMD modelling within this region. Despite this small region of discontinuity in the predictions, overall the match between the atomization version of the Σ–Y_{liq} model to experimental data presents a good agreement for a cold flow scenario under

varying liquid jet to gas momentum ratios and cross-flow velocities. This level of accuracy with regard to the jet height and droplet SMD show that the model is capable of predicting droplet SMD accurately downstream with a minimum of additional values required at the liquid boundary for a range of jet velocities and momentum ratios.

This comparison of momentum ratios and cross flow velocities shows that for a higher magnitude, the flow structure is altered by the increase in liquid jet penetration and reduced jet deflection. This correspondingly changes the prediction of the fuel concentration by increasing the liquid core length and predicts the presence of larger droplets travelling further into the cross flow. Additionally the concentration of high average surface area is shifted into the recirculation zone in front of the liquid inlet. The increase in shear between the two flows as result of the increased velocities and hence, kinetic energy, causes faster transport downstream which produces larger droplet sizes when compared to a lower cross flow velocity. The resulting downstream SMD comparison presents a good match to experimental data, no more than a 10 micron difference at peak with only the region close to the floor for low momentum ratios failing to predict an accurate value.

4.3 Vaporization

With all four atomization only cases presenting a good match to the experimental SMD, the next step was to expand into vaporization utilising equations 2.40 to 2.47 to supplement the atomization model to include vaporization of a liquid fuel. Using the previously converged atomization solution for U100P6Q6, the vaporization extension was applied with liquid and air inlet temperatures specified at 300K and 650K respectively. All other settings remained identical to the atomization run of U100P6Q6 covered in Section 4.2.2 in order to study the effect of vapour formation on the solution.

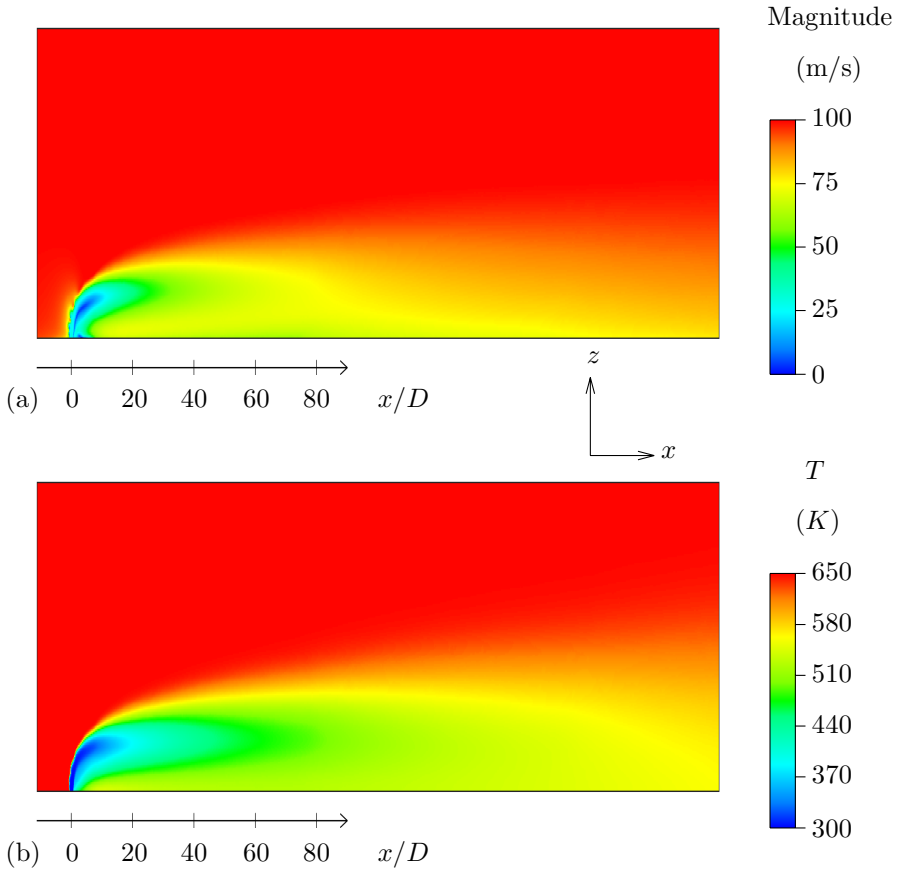

Figure 4.19: Velocity magnitude predictions for varying cross-flow air temperature on the domain symmetry plane. a) Average flow field for vaporization test case with 650 K cross flow, b) Average temperature for vaporization test case with 650 K cross flow.

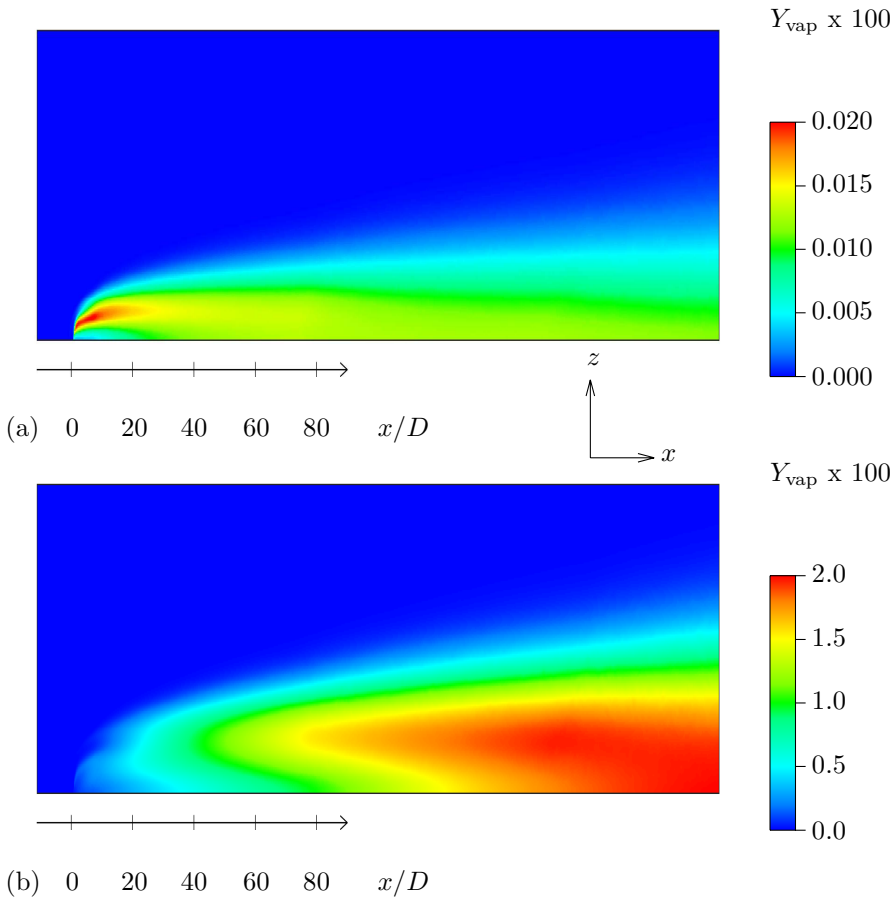

Figure 4.20: Average vapour mass fraction for cases with different cross flow temperatures: (a) $T = 300$ K, (b) $T = 650$ K.

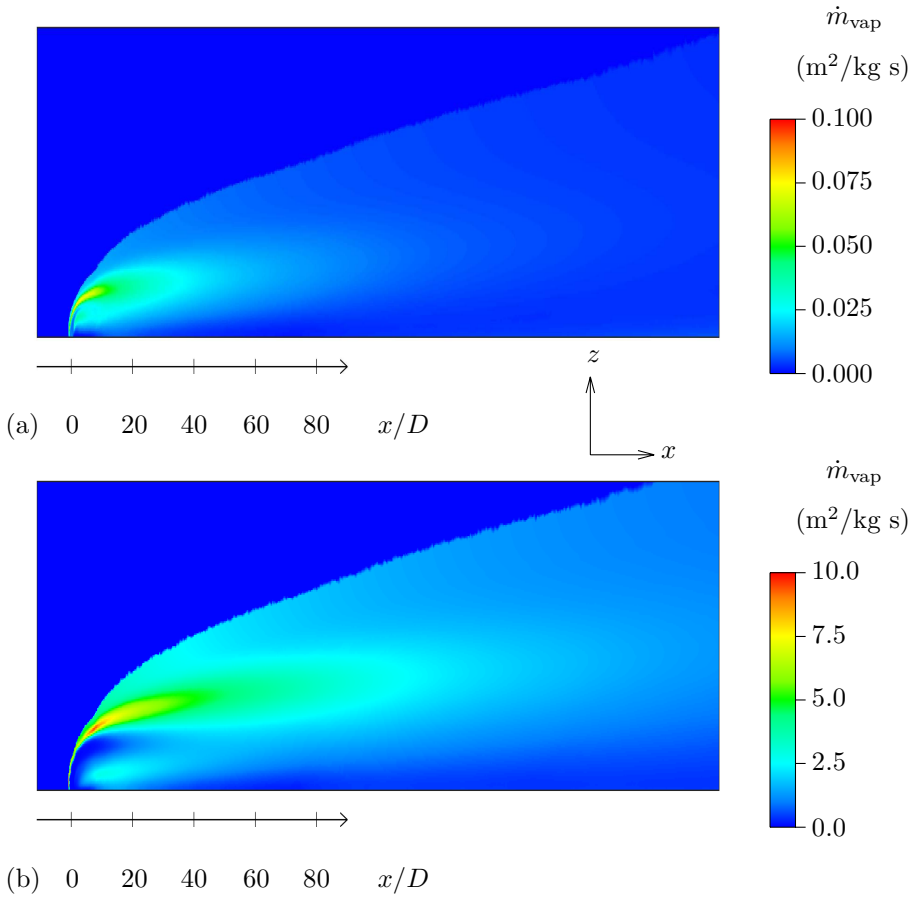

Figure 4.21: Average vaporization rate per unit mass for varying cross flow air temperature on the domain symmetry plane. a) 300K, b) 650K.

With the inlet temperature of 300K far below the fuels boiling point of 447.3 Kelvin, very little vapour formation was expected due to the very low temperature difference between jet and cross flow. The velocity magnitude shown in Figure 4.19 shows that although the velocity field is dependent upon temperature due to the change in density, raising the cross flow air temperature to 650K caused a small decrease in the jet deflection, shifting the low velocity region in front of the inlet to attach to the underside of the jet and move away from the domain floor. This temperature distribution also affects the liquid mass fraction predictions in the same fashion as the velocity field, shifting the concentration slightly in the z-direction but not any other significant changes. Σ predictions are also affected by the air temperature increase as there is a reduction in concentration beyond $x/D = 5$ between the floor and lower surface of the jet. Evaporation removes the smallest drops from the lower surface, thereby reducing the predicted surface per unit mass close to the inlet, further downstream beyond $x/D = 80$, this difference is less pronounced with both air temperatures predicting a similar magnitude and concentration.

With the liquid jet entering the domain at 300K, the average temperature quickly increase downstream from the inlet, visible in Figure 4.19, which in turn causes an increase in the average vaporization rate as the liquid surface temperature rises. The vapour generation occurs largely at the front of the liquid jet on the upper edge of the recirculation zone, causing an almost parallel intensity with the regions of highest liquid concentration. This formation rate results in the highest vapour concentration extending far downstream but never rising beyond a mass fraction of 0.0002 - indicating an upper limit of vapour production reached for this environment temperature. Increasing the air temperature from 300K to 650K increased the vapour mass fraction by several orders of magnitude, up from less than 0.0002 to 0.02 in Figure 4.20. The highest concentration now occurs downstream, increasing from $x/D = 20$ with the majority remaining close to the domain floor.

The average vaporization rate per unit mass predicts only a very low magnitude for 300K, as shown in Figure 4.21, concentrated above the liquid inlet within the region of high liquid mass fraction. This variable is bound by the presence of liquid fuel and each source term present in the transport equations will only

return a value where liquid surface is present. The highest vaporization rate, see Figure 4.21, is predicted toward the upper surface of the jet with the high shear between flows contributing to the production of numerous small diameter droplets which are easier to vaporise in the presence of the increased air temperature. The high level of turbulence in this region further contributes to the breakup by increasing instability in the liquid surface but has less of an effect in the bulk of the liquid as less shear breakup occurs in this region.

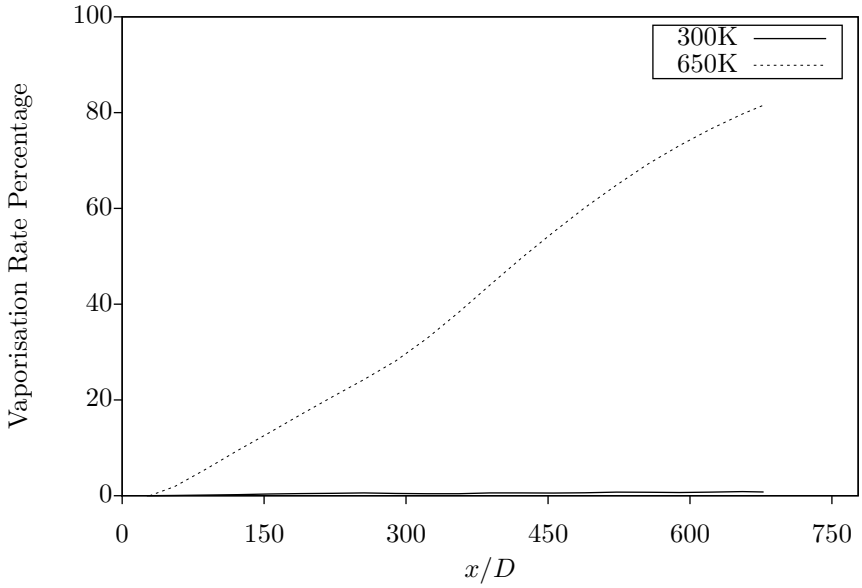

Figure 4.22: Integrated vapour mass flux versus downstream distance from the jet.

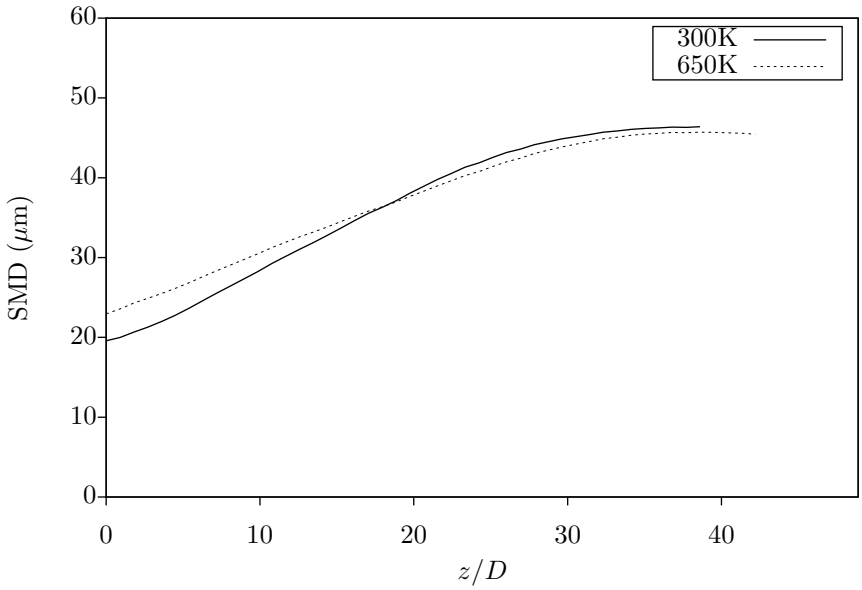

Figure 4.23: Predicted SMD of droplets at $x = 80$ mm ($x/D = 178$) for cases with different cross flow temperatures.

Over the total length of the domain from the liquid inlet, the total vaporization percentage was calculated for each air temperature in Figure 4.22. With a low evaporation rate of less than 1.5 % for the 300K air, even near the end of the domain at $x/D = 700$, the fuel spread from the jet central axis does not experience significant loss enough to alter the liquid mass fraction or shift the average surface area sufficiently to have much of an effect on the SMD. By comparison the high air temperature produces a total evaporation of up to 80 % by the end of the domain with the slight change in gradient between $x/D = 300$ to 350 indicates the change of mesh quality in the computational domain from fine to coarse which increases the cell size, this affects the evaporation rate jump but not dramatically.

Since the amount of fuel vapour produced is so small for the 300K air, there has been almost no change in the droplet SMD predictions shown in Figure 4.23 from the atomization equivalent case. Droplet SMD does reduce by several microns on the upper surface of the jet as a result of the increased temperature and lower fuel mass fraction, however the fuel is only vaporised by approximately 20 percent by this measurement region and the effect may be more evident downstream as only the largest droplets will remain at this point. Close to the domain floor, the SMD actually increases by up to 5 microns until $x/D = 15$ where the two profiles predict identical values, this change is likely a result of the evaporation of the smallest drops underneath the jet due to the increased temperature and the upward shift of the liquid off the domain floor. Overall the vaporization rate increases in accordance with a cross flow air temperature rise, vaporising the majority of the liquid fuel by the end of the domain and causing changes within the droplet SMD corresponding to the rate of liquid evaporation.

4.4 Summary

From the evaluation of multiple boundary conditions for the liquid jet, it has been shown that the new boundary assumptions detailed in Section 2.4.3 better represent inlet conditions by only assuming a value for Σ on the outer surface of the jet due to the presence of a liquid core. Along with a profiled velocity reminiscent of realistic turbulent pipe inlet flow these conditions provide the best approach for initialising the liquid jet simulations.

Comparison with experimental measurements of SMD for multiple momentum ratio boundary conditions showed a good match for all cases, with the higher momentum ratio jets presenting the best overall match. Neither of the low momentum ratio simulations could predict the near-wall increase of SMD close to the floor of the channel which may be attributed to droplet coalescence and/or wall wetting. It should also be noted that the known shortcomings of the k–ω turbulence model closure for relatively low turbulence cases could also account for these predictions. Fuel mass fraction predictions were consistent with the velocity fields: the deflection and penetration as a result of the momentum ratios changing the structure of the flow. Surface area generation was most prominent close to the jet inlet in regions of high turbulence.

The inclusion of vaporization was found to influence the predicted SMD with the low air temperature test case producing results consistent with an expected (low) vapour formation rate. With the temperature well below the boiling point of the fuel causing only a small fraction of vapour to be formed with less than 2% vaporised by the end of the domain. Increasing the air temperature to 650 K raised the total vaporization level up to approximately 80% over the full domain length and increased the downstream vapour mass fraction by orders of magnitude while also altering the flow structure by increasing the jet penetration. Despite this, the SMD predictions did not change dramatically with a small increase in total jet height and a maximum increase of 5 microns close to the floor. This was due to the low total vaporization of the fuel at $x/D = 80$ mm of less than 20%. Nevertheless the total fuel evaporation over the whole domain was well within expected behaviour.

Chapter 5

Application to an Industrial Gas Turbine

Following the validation of the Σ–Y_{liq} model for an atomization case study as described in Chapter 4, the model was applied to a liquid-fuelled gas turbine combustor. In this Chapter the results of atomization-only and vaporization test cases at the design temperature and pressure conditions of the combustor are compared to each other.

5.1 Siemens DLE Combustion System

The Siemens Dry Low Emissions (DLE) combustion system can be found on a range of gas turbines from the SGT-100 to the SGT-400 gas turbine, producing between 5MW to 15 MW and is capable of operation on liquid and gas fuels. This system focuses on operating in a lean and premixed setup for the purpose of reducing emissions (Norster and DePietro, 1996). Andrews (2013) contains a detailed review of swirl-stabilised combustion of this type with respect to the reduction of NO_x emissions.

Major components of this system can be seen in Figure 5.1, with the three main sections consisting of the pilot body, main burner and combustor. The main burner contains the radial swirler along with the main liquid and gas fuel systems and the pilot body contains the injectors and pilot galleries for liquid and gas (Igoe and McMillan, 1998). The combustor is of double-skin construction with

impingement jets providing cooling and contains a sudden expansion after the prechamber (Norster and DePietro, 1996). The introduction of gas and liquid fuel is in two stages: the pilot, which reduces with increasing load; and the premixed main injection (Bulat et al., 2007).

The radial swirler generates a sufficient swirl number to create vortex breakdown, leading to a central reverse flow region along the combustor axis (Bulat et al., 2009). A outer recirculation zone is also formed due to the expansion between the prechamber and combustion chamber. The shear layers generated between these two regions are used to stabilise the flame (Bulat et al., 2009).

The radial swirler consists of twelve rectangular passages of which six contain a liquid fuel nozzle at the floor. This six nozzle injection configuration is similar to a jet in cross flow and hence the model developed in this work is applied to SGT-400 with confidence. There are no experimental measurements for the SGT-400 to compare or validate the results from this model. Instead, the results shown here are mainly to highlight the liquid behaviour and spray characteristics in industrial gas turbines.

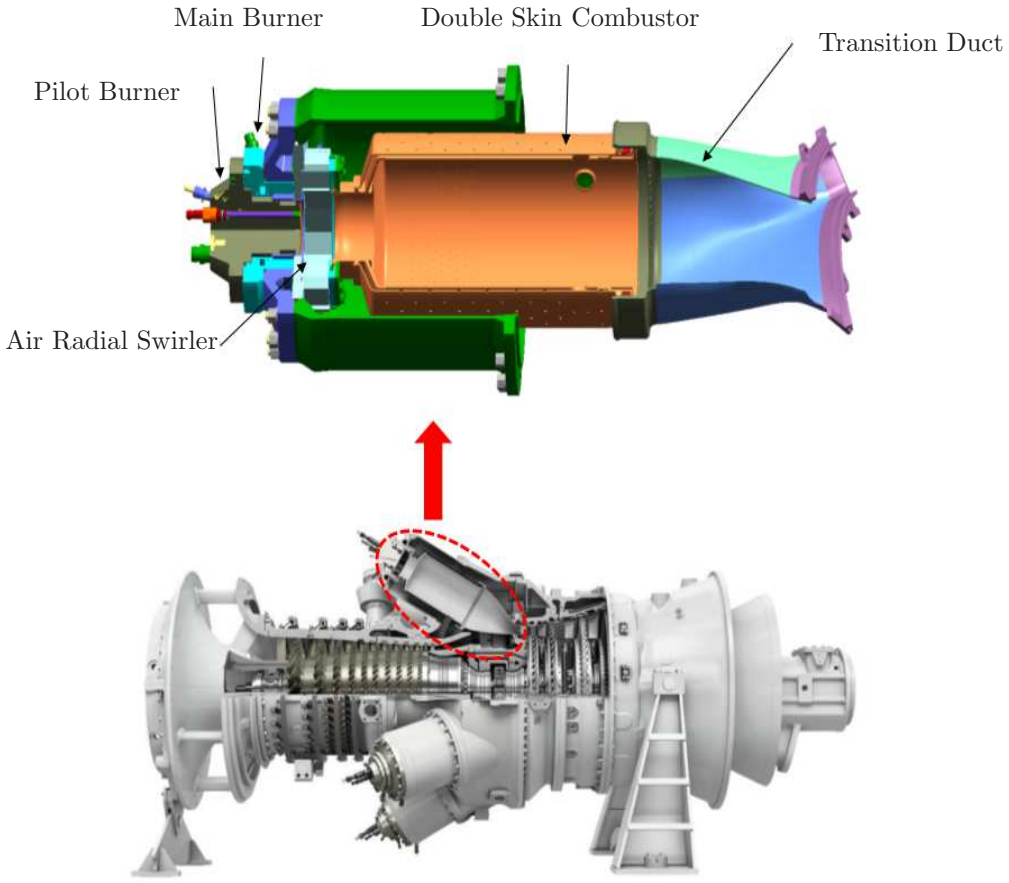

Figure 5.1: Major components of the Siemens DLE combustion system. (Image used with permission from Siemens, Lincoln. (Sadasivuni et al., 2012))

5.2 Numerical Setup

The SGT-400 Combustion system is simulated for liquid spray from main liquid nozzles at full load conditions. The pressure ratio for the SGT-400 at full load is approximately 16:1 (Liu et al., 2013). Diesel fuel is simulated from liquid injection from six nozzles in alternating swirler slots. ICEM CFD is used for generating the tetrahedral mesh for the combustor and is shown in Figure 5.2. A total of 9 million cells are used in accordance with the best practice typically used in industry (Sadasivuni et al., 2012) (Bulat et al., 2014). Additional refinement is included in regions of fuel injection, prechamber wall and partly into the expansion region. Both atomization and evaporation models are implemented on the SGT-400 combustor. The mesh used All simulations are run on an Intel Xeon processor with a minimum of 8 cores. Steady state simulations are conducted with a maximum physical time scale of 1×10^{-5} s and a minimum of 1×10^{-6} s were performed with a total of 0.103 and 0.114 CPU s per iteration per core for atomization and vaporization respectively. As with the simulations conducted in Chapter 4, this was a relatively small time penalty for the inclusion of vaporization.

The k–ω–SST model with standard wall functions (Menter, 2009) was used for turbulence closure within the Ansys CFX commercial CFD code and the liquid is modelled with Diesel as this fuel is typically used for industrial gas turbines.

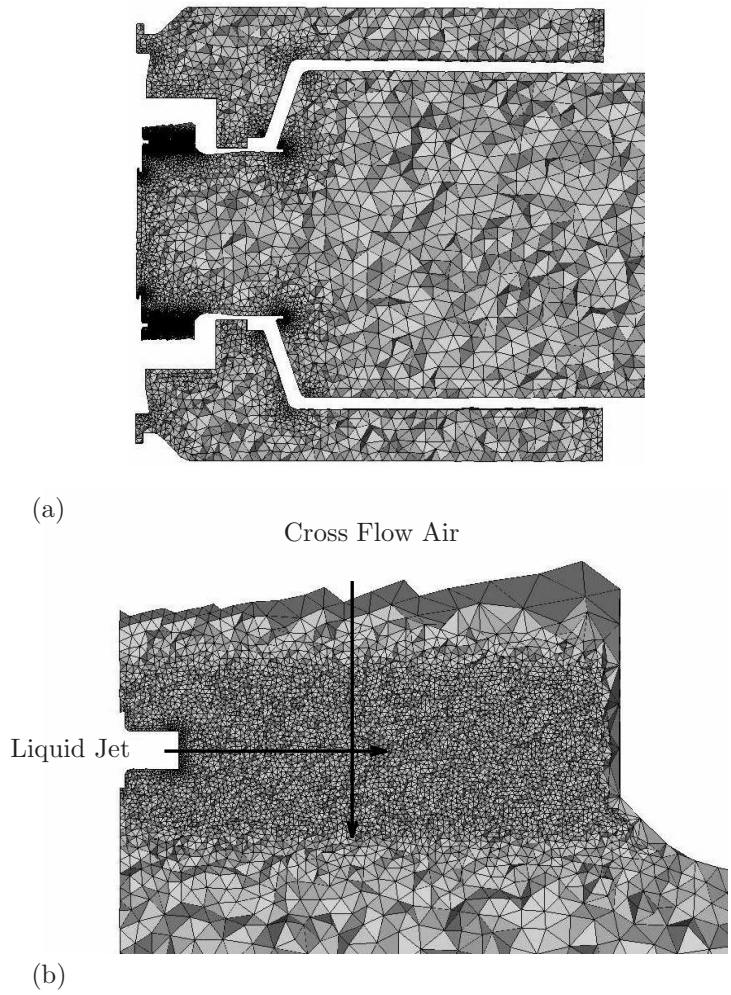

Figure 5.2: Computational mesh: (a) truncated side view of the combustor mid-plane, without the combustor exit; (b) refinement around the liquid fuel nozzle.

5.3 Results

A selection of results is presented showing key features of interest to evaluate the predictions of the Σ–Y model for atomization and vaporization in the SGT-400 dual fuelled gas turbine DLE combustion system for a non-reacting case. Results are focused on general flow field and aerodynamics, liquid spray distribution, effect of evaporation on liquid spray and its significance with respect to flame position in the main combustion chamber. The percentage of vaporization along the premixing region (pre-chamber) is also shown.

Figure 5.3 highlights the predicted flow field through the radial swirler and into the combustion chamber; the air flow through the radial swirler in combination with the size expansion beyond the prechamber give rise to the inner and outer recirculation zones (Sadasivuni et al., 2012) which are clearly visible for both atomization and vaporization predictions. Shear layers are formed between these zones as a result of the reverse flow and positive axial velocity at the prechamber walls and are used to stabilise the flame (Sadasivuni et al., 2012). These two large recirculation zones visible either side of the central axis successfully predict the expected flow pattern with only a small difference within flow structure between cases, this is expected because the addition of vaporization should only have a small effect upon the flow field; resulting in similar aerodynamics.

The liquid jet is first deflected by the cross flow air through the swirler channel before being transported through the prechamber. A liquid mass fraction of approximately 0.3 is present near the outer walls of the prechamber, for feeding the main flame, but is reduced by the subsequent breakup as a result of the increasing shear between flow regions before being recirculated towards the burner face by the inner recirculation zone. With the introduction of combustion, this concentration within the central region will reduce since the inner recirculation zone will be filled with hot product gases.

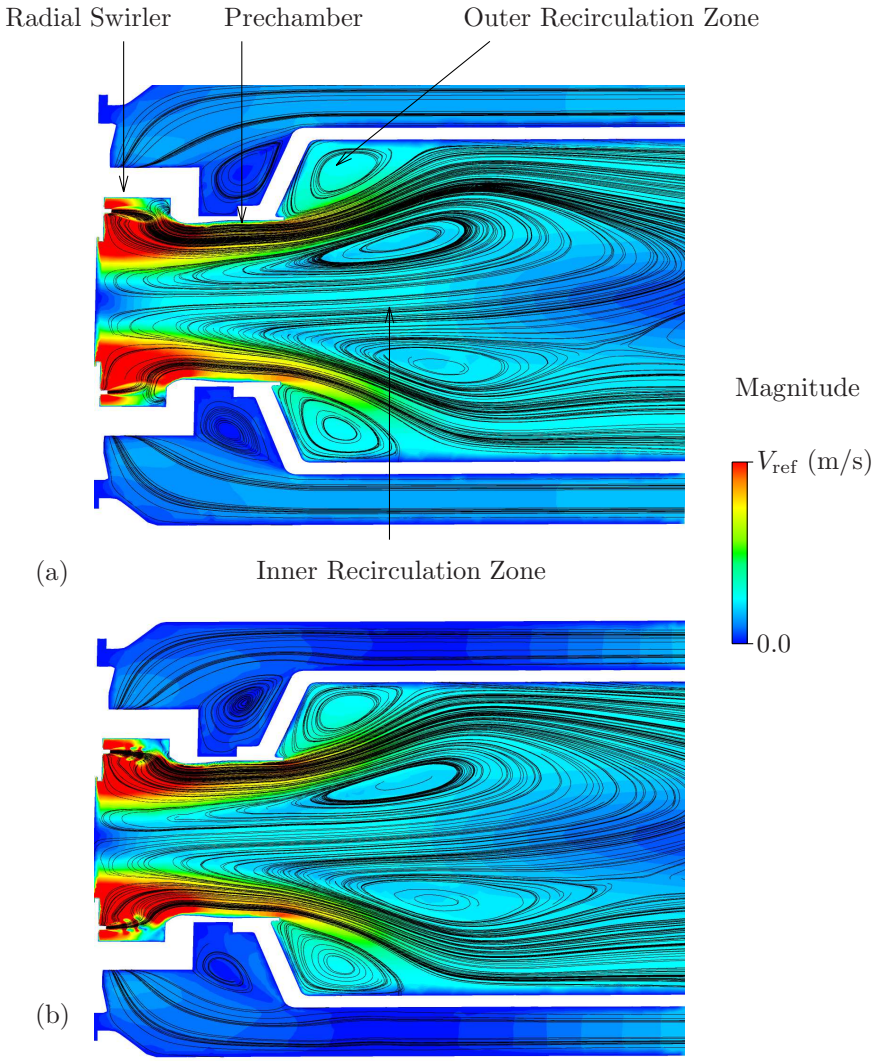

Figure 5.3: Average flow field predicted by RANS: (a) atomization-only case, (b) with vaporization.

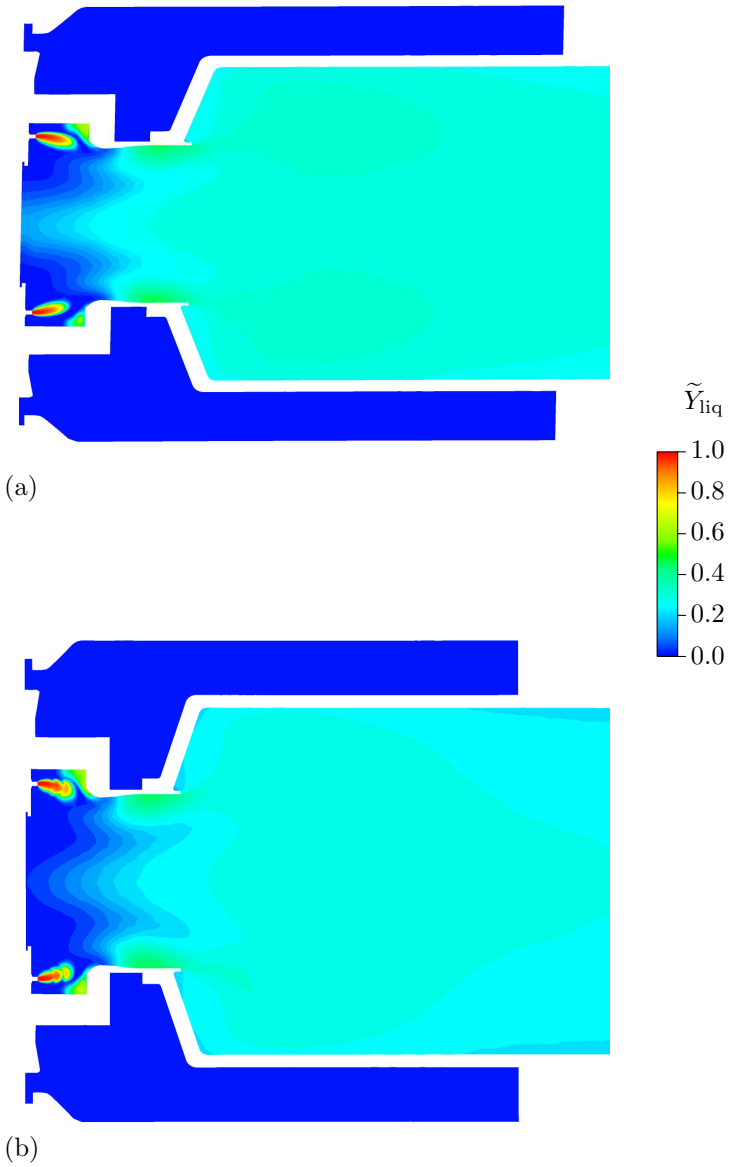

Figure 5.4: Average liquid mass fraction per unit mass: (a) atomization-only case, (b) with vaporization.

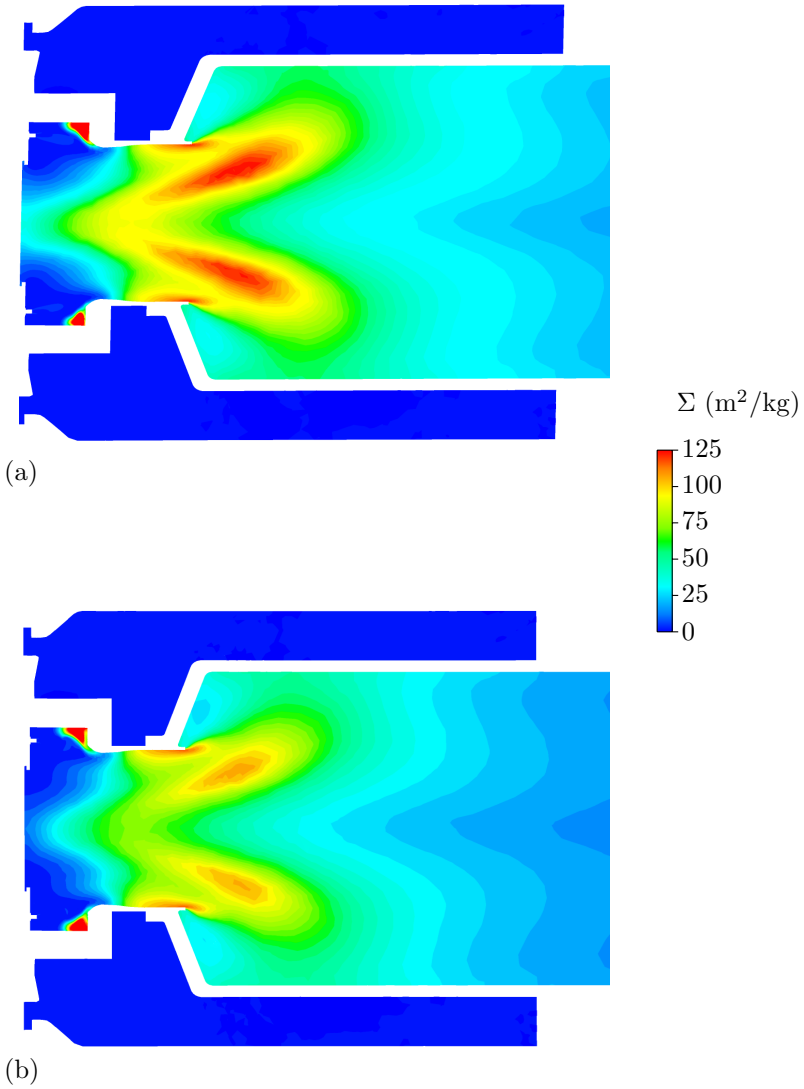

Figure 5.5: Average liquid surface area per unit mass: (a) atomization-only case, (b) with vaporization.

Figure 5.4 shows the changes that occur between atomization and vaporization, with the downstream liquid distribution for atomization in (a) exhibiting a visible increase within the first half of the prechamber. This results in increased concentration as the liquid is simply broken down and transported rather than any phase change occurring. Although the addition of vaporization in (b) causes the loss of liquid upstream, with a visible decrease in the first half of the prechamber, the downstream distribution across the combustion chamber is only slightly affected; but it should be noted that this region is subject to change with the inclusion of a flame. The liquid jet flow from the injectors can also visibly be seen to show 'wrinkling' for the vaporization case.

The average surface area per unit mass, Σ, is greatly affected by the inner and outer recirculation zones in addition to the breakup experienced by the jet in cross flow close to the injectors. The shear resulting from these recirculation phenomena causes a large increase of turbulent kinetic energy, which facilitates the liquid breakup, causing the formation of large numbers of smaller droplets due to the primary mechanism for surface breakup within the Σ–Y_{liq} model being dependant upon turbulence magnitude. This is supported by the high concentration and magnitude of Σ between these flows and along the prechamber walls in Figure 5.5, confirming that this area corresponds to liquid being broken down into smaller droplets of which some are recirculated towards the swirler. Vaporization reduces the total magnitude of the formed surface area within this region, reducing the downstream presence but retaining the same overall pattern with the two large concentrations between the shear layers. This region still accounts for the majority of the liquid breakup into the smallest droplets in both atomization and vaporization simulations. A reduction in concentration within the swirler is also notable, both these changes owing to the loss of liquid and surface generated as per Eq. (2.47) as a result of the evaporation. Overall the Σ–Y_{liq} predicts the largest concentration of average surface area per unit mass within the region of highest turbulence between the inner and outer recirculation zones on account of the shear between flows which causes increased liquid breakup; suggesting the presence of many small droplets within the region of positive axial velocity from the end of the prechamber.

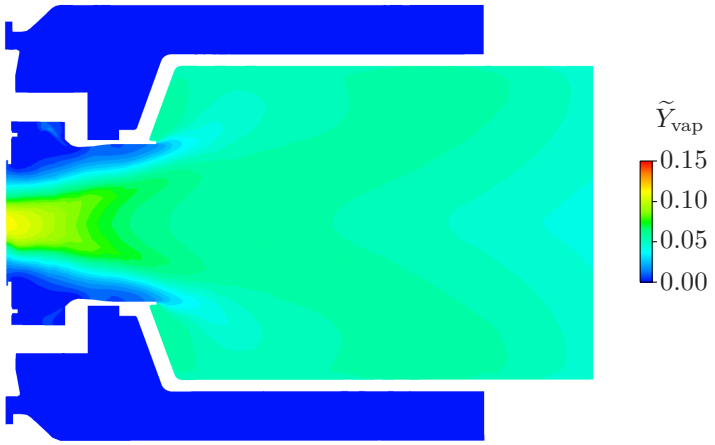

Figure 5.6: Average vapour mass fraction per unit mass.

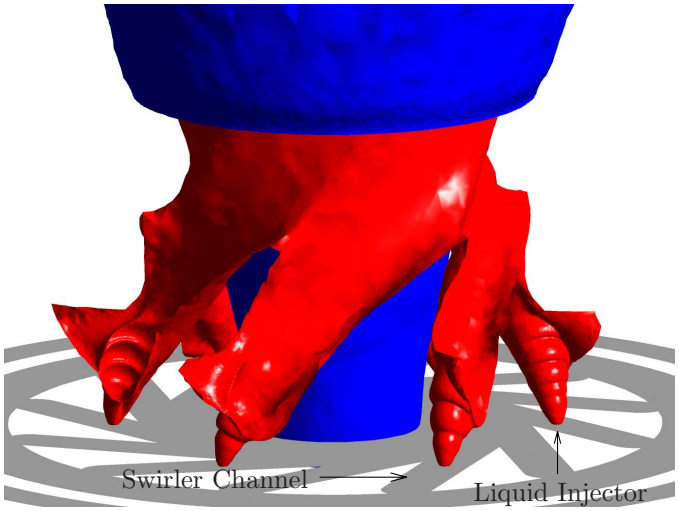

Figure 5.7: Isosurfaces of liquid and vapour mass fraction for the case with vaporization: (red) $\widetilde{Y}_{\mathrm{liq}} = 0.3$; (blue) $\widetilde{Y}_{\mathrm{vap}} = 0.045$.

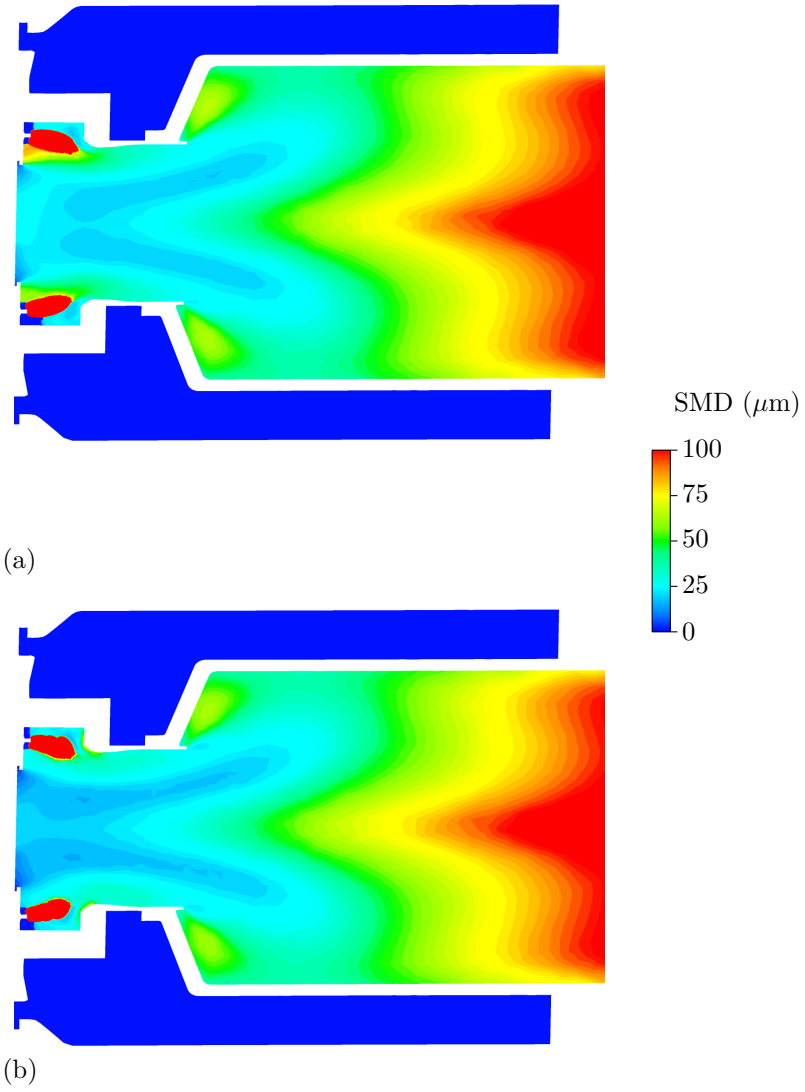

Figure 5.8: Predicted SMD in the mid-plane of the combustor: (a) atomization-only case, (b) with vaporization.

Although vapour formation occurs over the entire region, it is within the central recirculation zone where the highest concentration occurs, carried back into the swirler before transported downstream and retaining a fairly uniform magnitude throughout the combustion chamber. The light blue and green regions representing positive axial velocity through the prechamber, see Figure 5.6, show that liquid is vaporizing upstream before passing into the combustion chamber. This is supported by the average vaporization percentage of the liquid in Figure 5.10, shown to change by approximately 10% over the prechamber, and accounts for the small reduction within the downstream liquid mass fraction along with the reduction in recirculated liquid into the swirler where the highest vapour concentration is visible. Due to the mixing of the (cold) fuel and (hot) air, the average temperature is quickly brought below the boiling point of Diesel which results in a low vaproization percentage. However this data for the total vaporization % corresponds to the fuel vapour between the prechamber wall and inner recirculation zone only (positive axial velocity) as products recirculated upstream by the inner recirculation zone are discounted as the fuel vapour will have been burned when the flame is present. Therefore, the addition of vaporization shifts the average liquid concentration downstream within the prechamber due to evaporation, reducing liquid recirculation with a high vapour concentration predicted upstream in the swirler; influenced mainly by the inner and outer recirculation zones.

The isosurface plot in Figure 5.7 highlights two areas of importance from the fuel perspective. The first is the deflection of the liquid jets above the injectors by the cross flowing air, the second is the concentration of fuel vapour present within the central vortex. This figure serves to highlight the areas of vapour concentration, suggesting that the majority of the fuel vapour is recirculated on account of the reverse flow whereas the liquid jets are deflected and broken up into visible Gaussian plumes, before the individual plumes combine further downstream.

The effect of the inclusion of vaporization on the liquid mass fraction is visible in Figure 5.9 which shows the difference in droplet SMD throughout the prechamber between atomization and vaporization versions of the Σ–Y_{liq} model. With the total liquid vaporization percentage predicted at less than 4% at the

start of the prechamber there is a less than 10 μm difference upstream; possibly as a result of shifted liquid dispersion downstream visible in Figure 5.4. By the end of the prechamber, there is less than a 2 μm difference with the average SMD having dropped from approximately 80 to 30 μm. This close match suggests that the inclusion of liquid vaporization does not greatly influence the average SMD within the prechamber, with less than 15% of the total liquid vaporized by the end of this region, see Figure 5.10. With the majority of surface area increase occurring downstream within the shear layers for both simulations, see Figure 5.5, this indicates that more significant changes in SMD may be present within the regions of higher turbulence.

This low change within the average SMD throughout the prechamber can be seen in Figure 5.8, illustrating that there is almost no difference between the magnitude for atomization and vaporization. Due to the presence of the vortex within this region, the liquid breakup occurring within the shear layer has more of an effect upon the average SMD downstream whereas within the swirler, evaporation leads to the presence of smaller droplets and a changed liquid dispersion. Since the flow fields exhibit little difference as a result of the liquid vaporising and only the smallest droplets being recirculated within the inner zone, there is little change in overall pattern or magnitude which is not a result of the difference in surface generation within the shear layer or evaporation. Further downstream each case shows an increase within the average SMD, this can be explained due to the lack of combustion not reducing the liquid mass fraction along with the effect of the droplet number density, which will have a significant impact upon the predictions and is likely to be extremely low; indicating that although larger drops may remain downstream they will be very few in number. This means that this far downstream aspect of the predictions can be ignored.

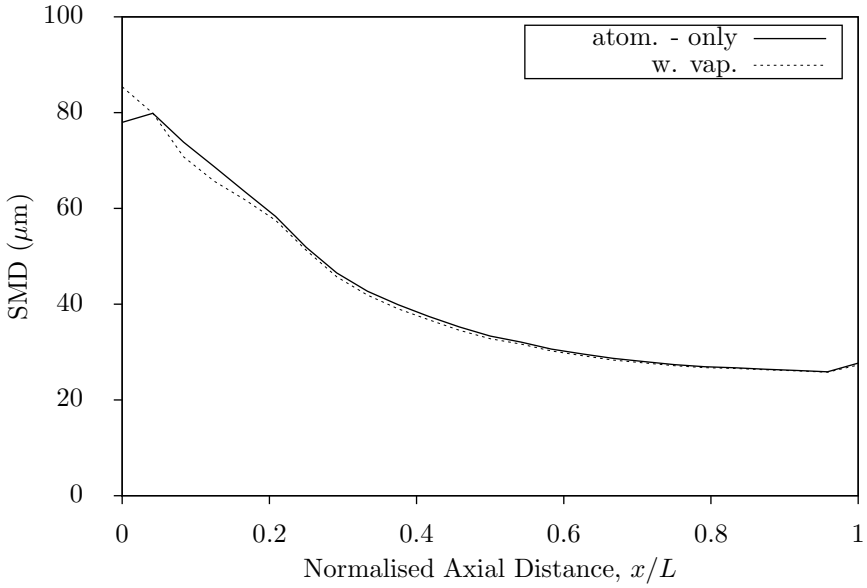

Figure 5.9: Predicted SMD of droplets versus normalised axial distance in the prechamber.

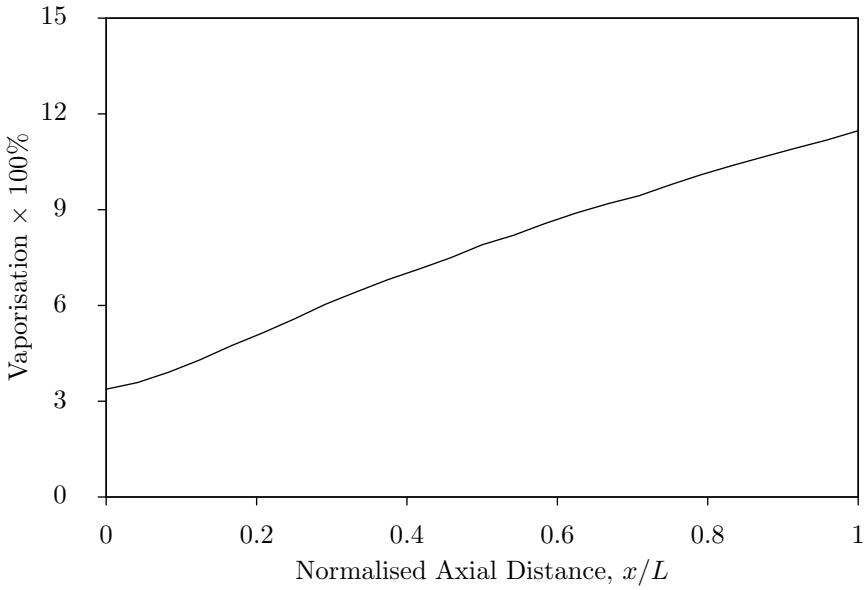

Figure 5.10: Integrated vapour mass flux versus normalised axial distance in the prechamber.

5.4 Summary

The Σ–Y_{liq} model successfully predicts liquid breakup dependent upon the local flow features in a gas turbine combustor. Non-reacting atomization and vaporization cases show a reduction in liquid magnitude and surface generation in the swirler and prechamber regions, with a corresponding vapour increase where Y_{liq} and Σ have been reduced. The inclusion of vaporization does not have a significant effect upon the average SMD predictions, particularly within the prechamber. However, it is noted that larger differences can be expected for a reacting case due to the inclusion of additional phenomena such as burning droplets.

Chapter 6

Conclusions and Future Work

6.1 Conclusions

Findings from the CFD software package comparison yielded very similar results for a RANS jet in cross flow prediction using standard constants. This established the importance of turbulence model tuning depending upon the flow type, a well known issue which can affect predictions.

Validation against experimental data for a gas jet found LES provided the best match with a 'flat' velocity profile. This was expected given the shortcomings of the RANS method such as the lack of resolving all large scales; however both methods managed to capture the major flow features. The use of a profiled jet inlet velocity based upon the experimental data improved RANS predictions, particularly the jet penetration and also yielded a reasonable match with the experiments. Varying the jet to cross flow momentum ratio changed the level of jet deflection and caused a corresponding shift in important flow features such as the recirculation zone and vortex pair. From these comparisons it was possible to conclude that a RANS approach with a profiled jet inlet velocity was adequate to capture the important large scale features of jet in cross flow and therefore a suitable base for the development of the Σ–Y model.

The novel boundary condition for Σ at the liquid inlet, which applies a non-zero value only on the outer edges of the jet, was found to be insensitive to the size parameter, Δr. This suggests that it may be possible to apply this boundary condition to LES studies which have suggested sensitivity to the Σ inlet boundary

conditions (Navarro-Martinez, 2014). Pairing this boundary condition with a profiled jet inlet velocity for validation of the Σ–Y model against a variety of jet to cross flow momentum ratios generally provided good agreement with experimental SMD data. Only the near-wall SMD for the lower momentum ratio cases did not match the experimental data, failing to predict the sudden increase in diameter. This phenomena has been predicted in previous Σ–Y studies (Sidhu and Burluka, 2008) which suggest that it is the RANS closure which is responsible for this issue and highlights the importance of the turbulence closure for atomization modelling. However this only occurs in a very small region with the remainder of the SMD predictions for all jet momentum ratios presenting a good match to the experimental data.

Vapour formation at both high and low air cross flow air temperatures was successfully predicted with the formation regions downstream of the inlet being correctly positioned along with the rise in total liquid vaporization from less than 1% at 300 K to over 75% at 650 K by the end of the domain under test conditions. These results demonstrate that the Σ–Y model is capable of predicting SMD values for a non-reacting liquid jet in cross flow using a RANS approach with a profiled jet velocity and the novel Σ boundary condition.

Application of the Σ–Y_{liq} model to a liquid fuelled gas turbine geometry showed that the liquid surface generation is heavily influenced by the the two recirculation zones causing a large increase in surface area formation due to shear between flows within regions of positive axial velocity. Droplets in the flame stabilisation region are of a similar size to those predicted in the Chapter 4 simulations. The addition of the vaporization mechanism causes a shift in the liquid concentration, reducing the predicted surface area due to evaporation but has little effect on the average SMD throughout the prechamber. With a relatively low total liquid evaporation of less than 14% by the end of the prechamber, this suggests that the net vaporization is constrained by the temperature due to the mixing of the air and fuel. It is therefore possible to conclude that the Σ–Y model was successful in liquid predictions for a complex geometry, with local flow phenomena showing an expected influence upon the liquid breakup for a non-reacting case. However it is likely that these results would change significantly if combustion was introduced as this would raise the average temperature,

altering the level of vaporization and removing the far downstream SMD presence. In addition, other phenomena such as burning droplets would affect the size distribution.

6.2 Future Work

Following the validation against experimental data and application to an industrial geometry as presented in the current work, the Σ–Y_{liq} model could be potentially used as a design tool within industry. Since the model is based upon a RANS approach in a commercial CFD package (Ansys CFX), it should be relatively easy to apply to URANS, which may improve the turbulence predictions. Further improvements of the near-wall atomization and vaporization could also be obtained via the use of different boundary conditions at the walls of the domain.

Another future consideration may be to couple the Σ–Y_{liq} model with a combustion model to allow application to reacting flows as per Borghi and Burluka (1999) for fast chemistry. This would allow the modelling of the full process from liquid injection to combustion and could result in a predictive capability with respect to emissions.

An additional possibility is the implementation of an LES version of the model using a CFD software package such as OpenFOAM which can account for all large scale turbulence phenomena. However, closure issues are anticipated regarding the turbulence dissipation terms which are used as inputs into the Σ–Y_{liq} model. Since these quantities are entirely modelled within the RANS approach, an alternate closure based around the SGS model is required for LES.

References

Abe, K. (2014). An advanced switching parameter for a hybrid LES/RANS model considering the characteristics of near-wall turbulent length scales. *Theor. Comput. Fluid Dyn. 28*, 499–519.

Abramzon, B. and W. A. Sirignano (1989). Droplet vaporization model for spray combustion calculations. *Int. J. Heat Mass Tran. 32*, 1605–1618.

Aggarwal, S. K. and F. Peng (1995). A review of droplet dynamics and vaporization modelling for engineering calculations. *J. Eng. Gas Turb. Power 117*, 453–461.

Alfonsi, G. (2009). Reynolds Averaged Navier-Stokes equations for turbulence modelling. *Appl. Mech. Rev. 62*, 1–20.

Anderson, D. A., J. C. Tannehill, and R. H. Pletcher (1984). *Computational Fluid Mechanics and Heat Transfer*. New York: McGraw Hill.

Andreopoulos, J. and W. Rodi (1984). Experimental investigation of jets in a cross-flow. *J. Fluid Mech. 138*, 93–127.

Andrews, G. (2013). Ultra-low nitrogen oxides emissions in gas turbine systems. In P. Jansohn (Ed.), *Modern Gas Turbine Systems*. Cambridge: Woodhead Publishing Limited.

Argyropoulos, C. D. and N. C. Markatos (2015). Recent advances on the numerical modelling of turbulent flows. *Appl. Math. Model. 39*, 693–732.

Bai, B.-F., H.-B. Zhang, L. Liu, and H.-J. Sun (2009). Experimental study on turbulent mixing of spray droplets in crossflow. *Exp. Therm. Fluid Sci. 33*, 1012–1020.

Balabel, A. and W. A. El-Askary (2011). On the performance of linear and nonlinear k–ε turbulence models in various jet flow applications. *Eur. J. Mech. B/Fluids 30*, 325–340.

Balasubramanyam, M. S. and C. P. Chen (2008). Modelling liquid jet breakup in high speed cross-flow with finite-conductivity evaporation. *Int. J. Heat Mass Tran. 51*, 3896–3905.

Banerjee, S. and C. J. Rutland (2015). Study on spray induced turbulence using Large Eddy Simulations. *Atomization Sprays 25*, 285–316.

Bayvel, L. and Z. Orzechowski (1993). *Liquid Atomization*. Washington DC: Taylor and Francis.

Becker, J. (2004). *Spray Dispersion in a Generic Premixing Module for Aero-engine Combustors (In German)*. Ph. D. thesis, Ruhr University Bochum.

Beheshti, N., A. A. Burluka, and M. Fairweather (2005). Eulerian modelling of atomization in turbulent flows. *Computer-Aided Chem. Eng. 20a-20b*, 139–144.

Beheshti, N., A. A. Burluka, and M. Fairweather (2007). Assessment of Σ-Y_{liq} model predictions for air-assisted atomisation. *Theor. Comp. Fluid Dyn. 21*, 381–397.

Belhadef, A., A. Vallet, A. Amielh, and F. Anselmet (2012). Pressure-swirl atomization: modelling and experimental approaches. *Int. J. Multiphase Flow 39*, 13–20.

Bianchi, G. M., P. Pelloni, F. E. Corcione, L. Allocca, and F. Luppino (2001). Modelling atomization of high-pressure diesel sprays. *J. Eng. Gas Turb. Power 123*, 419–427.

Bird, R. B., W. E. Stewart, and E. N. Lightfoot (2002). *Transport Phenomena* (2nd ed.). New York: John Wiley and Sons.

Birouk, M., C. O. Iyogun, and N. Popplewell (2007). Role of viscosity on trajectory of liquid jets in a cross-airflow. *Atomization Sprays 17*, 267–287.

Boileau, M., S. Pascaud, E. Riber, B. Cuenot, L. Gicquel, T. Poisnot, and M. Cazalens (2008). Investigation of two-fluid methods for Large Eddy Simulation of spray combustion in gas turbines. *Flow Turb. Combust. 80*, 291–321.

Borghi, R. and A. Burluka (1999). Simple model for turbulent two-phase combustion with fast chemistry. *Z. angew. Math. Mech. 79*, 37–40.

Bulat, G., W. Jones, and A. Marquis (2014). NO and CO formation in an industrial gas-turbine combustion chamber using LES with the Eulerian subgrid PDF method. *Combust. Flame 161*, 1804–1825.

Bulat, G., D. Skipper, R. McMillan, and K. Syed (2007, Jan). Active control of fuel splits in gas turbine DLE combustion systems. In *Proc. ASME Turbo Expo*, pp. 135–144.

Bulat, G., P. Stopford, M. Turrell, D. Frach, E. Buchanan, and M. Stöhr (2009, Jan). Prediction of aerodynamic frequencies in a gas turbine combustor using transient CFD. In *Proc. ASME Turbo Expo*, pp. 585–594.

Chesnel, J., J. Reveillon, T. Menard, and F. X. Demoulin (2011). Large Eddy Simulation of liquid jet atomization. *Atomization Sprays 21*, 711–736.

Cohen, H., G. F. C. Rogers, and H. I. H. Saravanamuttoo (1996). *Gas Turbine Theory* (4th ed.). Harlow: Longman.

Crabb, D., D. F. G. Durao, and J. H. Whitelaw (1981). A round jet normal to a crossflow. *J. Fluids Eng. 103*, 142–154.

De Luca, M., A. Vallet, and R. Borghi (2009). Pesticide atomization for hollow-cone nozzle. *Atomization Sprays 19*, 741–753.

Demoulin, F.-X., G. Beau, P-A. Blokkeel, A. Mura, and R. Borghi (2007). A new model for turbulent flows with large density fluctuations. *Atomization Sprays 17*, 315–345.

Demoulin, F.-X., J. Reveillon, B. Duret, Z. Bouali, P. Desjonqueres, and T. Menard (2013). Toward using Direct Numerical Simulation to improve primary break-up modelling. *Atomization Sprays 23*, 957–980.

Desantes, J. M., J. Arregle, J. J. Lopez, and J. M. Garcia (2006). Turbulent gas jets and diesel-like sprays in a crossflow: a study on deflection and air entrainment. *Fuel 85*, 2120–2132.

Desjardins, O. and H. Pitsch (2010). Detailed numerical investigation of turbulent atomization of liquid jets. *Atomization Sprays 20*, 311–356.

Dietzel, D., D. Messig, A. Piscaglia, Montorfano, G. Olenik, O. T. Stein, A. Kronenburg, A. Onorati, and C. Hasse (2014). Evaluation of scale resolving turbulence generation methods for Large Eddy Simulation of turbulent flow. *Comput. Fluids 93*, 116–128.

Duret, B., J. Reveillon, T. Menard, and F.-X. Demoulin (2013). Improving primary atomization modeling through DNS of two-phase flows. *Int. J. Multiphase Flow 55*, 130–137.

Fureby, C. (2008). Towards the use of Large Eddy Simulation in engineering. *Prog. Aerosp. Sci. 44*, 381–396.

Fureby, C., G. Tabor, G. Weller, and A. D. Gosman (1997). Comparative study of subgrid scale models in homogeneous isotropic turbulence. *Phys. Fluids 9*, 1416–1429.

Galeazzo, F. C. C., G. Donnert, C. Cardenas, J. Sedlmaier, P. Habisreuther, N. Zarzalis, C. Beck, and W. Krebs (2013). Computational modeling of turbulent mixing in a jet in crossflow. *Int. J. Heat Fluid Flow 41*, 55–65.

Galeazzo, F. C. C., G. Donnert, P. Habisreuther, N. Zarzalis, R. J. Valdes, and W. Krebs (2010, Jun). Measurement and simulation of turbulent mixing in a jet in crossflow. In *Proc. ASME Turbo Expo*, Glasgow. GT2010-227093.

Germano, M. (1992). Turbulence: the filtering approach. *J. Fluid Mech. 238*, 325–336.

Germano, M., U. Piomelli, P. Moin, and W. H. Cabot (1991). A dynamic subgrid-scale eddy viscosity model. *Phys. Fluids 3*, 1760–1765.

Gopalan, H., S. Heinz, and M. K. Stollinger (2013). A unified RANS-LES model: computational development, accuracy and cost. *J. Comput. Phys. 249*, 249–274.

Herrmann, M. (2009, Jun). Detailed numerical simulations of the primary atomization of a turbulent liquid jet in crossflow. In *Proc. ASME Turbo Expo*, Orlando. GT2009-59563.

Herrmann, M. (2011). The influence of density ratio on the primary atomization of a turbulent liquid jet in a crossflow. *Proc. Combust. Inst. 33*, 2079–2088.

Herrmann, M., M. Arienti, and M. Soteriou (2010, Jun). The impact of density ratio on the primary atomization of a turbulent liquid jet in crossflow. In *Proc. ASME Turbo Expo 2010*, Glasgow. GT2010-23016.

Hinze, J. O. (1975). *Turbulence* (2nd ed.). New York: McGraw Hill.

IEA (2014). World Energy Investment Outlook: Special Report. OECD/IEA, www.worldenergyinvestmentoutlook.org/investment.

Igoe, B. and R. McMillan (1998). Dual fuel DLE on the Alstom typhoon gas turbine. *Proc. Inst. Mech. Eng.*.

Ivanova, E., M. Di Domenico, B. Noll, and M. Aigner (2009, Jun). Unsteady simulations of flow field and scalar mixing in transverse jets. In *Proc. ASME Turbo Expo*, Glasgow. GT2009-59147.

Ivanova, E., B. Noll, and M. Aigner (2010, Jun). Computational modelling of turbulent mixing of a transverse jet. In *Proc. ASME Turbo Expo*, Glasgow. GT2010-22764.

Ivanova, E., B. Noll, and M. Aigner (2012, Jun). A numerical study on the turbulent Schmidt numbers in a jet in crossflow. In *Proc. ASME Turbo Expo 2012*, Copenhagen. GT2012-69294.

Javadi, K., M. Taeibi-Rahni, and M. Darbandi (2007, Nov). Evaluation of RANS approach in predicting the physics of incompressible turbulent jets into crossflow. In *Proc. ASME International Mechanical Engineering Congress and Exposition*, Seattle, WA. IMECE2007-41114.

Jones, W. and C. Lettieri (2010). Large Eddy Simulation of spray atomization with stochastic modeling of breakup. *Phys. Fluids 22*, 115106.

Jones, W., C. Lettieri, A. Marquis, and S. Navarro-Martinez (2012). Large Eddy Simulation of the two-phase flow in an experimental swirl-stabilized burner. *Int. J. Heat Fluid Flow 38*, 145–158.

Jones, W. P. and B. E. Launder (1972). Prediction of laminarization with a two-equation model of turbulence. *Int. J. of Heat Mass Tran. 15*, 301–314.

Karagozain, A. R. (2010). Transverse jets and their control. *Prog. Energy Combust. Sci. 36*, 531–553.

Karrholm, F. P., F. Tao, and N. Nordin (2008). Three-dimensional simulation of diesel spray ignition and flame lift-off using OpenFOAM and KIVA-3V CFD code. *SAE Tech. Paper*, 1–16. 2008-01-0961.

Keimasi, M. R. and M. Taeibi-Rahni (2001). Numerical simulation of jets in crossflow using different turbulence models. *AIAA J. 39*, 2268–2277.

Kelso, R. M., T. T. Litt, and A. E. Perry (1996). An experimental study of round jets in cross-flow. *J. Fluid Mech. 306*, 111–144.

Kim, S. W. and T. J. Benson (1992). Calculation of a circular jet in crossflow with a multiple time-scale turbulence model. *Int. J. Heat Mass Tran. 35*, 2357–2365.

Kleinstreuer, C. (2003). *Two-Phase Flow: Theory and Application*. New York: Taylor and Francis.

Kodavasal, J., C. P. Kolodziej, S. A. Ciatti, and S. Som (2015). Computational Fluid Dynamics simulation of gasoline compression ignition. *ASME J. Energy Resources Tech. 137*, 1–13.

Kokkinakis, I. W. and D. Drikakis (2015). Implicit Large Eddy Simulation of weakly-compressible turbulent channel flow. *Comput. Methods Appl. Mech. Eng. 287*, 229–261.

Kolmogorov, A. N. (1942). Equations of turbulent motion of an incompressible fluid. *Izv. Acad. Sci. USSR, Phys. 6*, 56–58.

Launder, B. and B. Sharma (1974). Application of the energy dissipation model of turbulence to the calculation of a flow near a spinning disk. *Lett. Heat Mass Transfer 1*, 131–138.

Launder, B. E. and D. B. Spalding (1972). *Lectures in Mathematical Models of Turbulence*. London: Academic Press.

Lebas, R., G. Blokkeel, P.-A. Beau, and F.-X. Demoulin (2005). Coupling vaporization model with the Eulerian-Lagrangian Spray Atomization (ELSA) in diesel engine conditions. *SAE Technical Report*. 2005-01-0213.

Lefebvre, A. H. (1983). *Gas Turbine Combustion*. New York: Hemisphere Publishing Corporation.

Lefebvre, A. H. (1989). *Atomization and Sprays*. New York: Hemisphere Publishing Corporation.

Lesieur, M. (2008). *Turbulence in Fluids* (4th ed.). Dordrecht: Springer.

Lightfoot, M. D. A. (2009). Fundamental classification of atomization processes. *Atomization Sprays 19*, 1065–1104.

Lilly, D. K. (1992). A proposed modification of the Germano subgrid scale closure method. *Phys. Fluids A4*, 633–635.

Lin, S. P. and R. D. Reitz (1998). Drop and spray formation from a liquid jet. *Ann. Rev. Fluid Mech. 30*, 85–105.

Liu, K., P. Martin, V. Sanderson, and P. Hubbard (2013, Jun). Effect of change in fuel compositions and heating value on ignition and performance for Siemens SGT-400 Dry Low Emission combustion system. In *Proc. ASME Turbo Expo*, San Antonio. GT2013-94183.

Liu, S. and A. Novoselac (2014). Lagrangian particle modeling in the indoor environment: a comparison of RANS and LES turbulence models. *HVAC & R Research 20*, 480–495.

Lubarsky, E., J. R. Reichel, B. T. Zinn, and R. McAmis (2010). Spray in crossflow: dependence on Weber number. *J. Eng. Gas Turb. Power 132*, 1–9.

Luret, G., T. Menard, A. Berlemont, J. Reveillon, F.-X. Demoulin, and G. Blokkeel (2010). Modelling collision outcome in moderately dense sprays. *Atomization Sprays 20*, 251–268.

Majander, P. and T. Siikonen (2002). Evaluation of Smagorinsky based subgrid-scale models in a finite-volume computation. *Int. J. Numer. Methods Fluids 40*, 735–774.

Majander, P. and T. Siikonen (2006). Large-eddy simulation of a round jet in cross-flow. *Int. J. Heat Mass Tran. 27*, 402–415.

Masri, A., S. Pope, and B. Dally (2000). Probability density fluctuation computation of a strongly swirling nonpremixed flame stabilised on a new burner. *Proc. Combust. Inst. 28*, 123–131.

Massey, B. and J. Ward-Smith (2006). *Mechanics of Fluids* (8th ed.). London: Taylor and Francis.

Menter, F. R. (1994). Two equation eddy-viscosity models for engineering applications. *AIAA J. 32*, 1598–1605.

Menter, F. R. (2009). Review of the shear-stress transport turbulence model: experience from an industrial perspective. *Int. J. Comput. Fluid Dyn. 23*, 305–316.

Menter, F. R., M. Kuntz, and R. Langtry (2003). Ten years of industrial experience with the SST turbulence model. *Turbulence, Heat and Mass Transfer 4*, 1–8.

Metzger, M. M. and J. C. Klewicki (2001). A comparative study of near-wall turbulence in high and low Reynolds number boundary layers. *Phys. Fluids 13*, 692–701.

Moffat, D. L. and A. A. Burluka (2013, Jun). Modelling of a turbulent jet in a gas cross-flow. In *Proc. of ASME Turbo Expo*, San Antonio. GT2013-94309.

Mohammadi, B. and O. Pironneau (1993). *Analysis of the k-epsilon Turbulence Model*. Chichester: John Wiley and Sons.

Montomoli, F. and F. Eastwood (2011). Implementation of synthetic turbulence inlet for Turbomachinery LES. *Comput. Fluids 46*, 369–374.

Morton, B. R. and A. Ibbetson (1996). Jets deflected in a crossflow. *Exp. Therm. Fluid Sci. 12*, 112–133.

Navarro-Martinez, S. (2014). Large Eddy Simulation of spray atomization with a probability density function method. *Int. J. Multiphase Flow 63*, 11–22.

Nerisson, P., O. Simonin, L. Ricciardi, A. Douce, and J. Fazileabasse (2011). Improved CFD transport and boundary conditions models for low-inertia particles. *Comput. Fluids 40*, 79–91.

Nikitin, N. V., F. Nicoud, B. Wasistho, K. D. Squires, and P. R. Spalart (2000). An approach to wall modeling in Large Eddy Simulations. *Phys. Fluids 12*, 1629–1632.

Ning, W., R. Reitz, A. Lipper, and R. Diwakar (2007, April). Development of a next-generation spray and atomization model using an Eulerian-Lagrangian methodology. In *17th International Multidimensional Engine Modelling User's Group Meeting*, Detroit.

Ning, W., R. D. Reitz, R. Diwakar, and A. Lipper (2007). An Eulerian-Lagrangian spray and atomization model with improved turbulence modelling. *Atomization Sprays 19*, 727–739.

Norster, E. and S. DePietro (1996). Dry low emissions combustion system for egt small gas turbines. *Trans. Inst. Diesel Gas Turb. Eng. 495*, 1–9.

Oda, T., H. Hiroyasu, M. Arai, and K. Nishida (1994). Characterization of liquid jet atomization across a high-speed airstream. *JSME Int. J., Series B 37*, 937–944.

Peters, N. (2000). *Turbulent Combustion*. Cambridge, UK: Cambridge University Press. Fourth Printing.

Pope, S. B. (1994). Lagrangian pdf methods for turbulent flows. *Annu. Rev. Phys. Mech. 26*, 26–63.

Pope, S. B. (2004). Ten questions concerning the Large Eddy Simulation of turbulent flows. *New J. Phys. 6*, 1–24.

Ragucci, R., A. Bellofiore, and A. Cavaliere (2007). Breakup and breakdown of bent kerosene jets in gas turbine conditions. *Proc. Combust. Inst. 31*, 2231–2238.

Rana, A. and M. Herrmann (2011). Primary atomization of a liquid jet in cross-flow. *Phys. Fluids 23*, 1109.

Reid, R. C., M. J. Prausnitz, and B. E. Polling (1987). *The Properties of Liquids and Gases* (4th ed.). New York: McGraw Hill.

Reveillon, J. and F.-X. Demoulin (2007). Evaporating droplets in turbulent reacting flows. *Proc. Combust. Inst. 31*, 2319–2326.

Riber, E., V. Moureu, M. Garcia, T. Poinsot, and O. Simonin (2009). Evaluation of numerical strategies for large eddy simulation of particulate two-phase recirculating flows. *J. Comput. Phys. 228*, 539–564.

Roache, P. (1998). *Fundamentals of Computational Fluids Dynamics*. Alberquerque, USA: Hermosa Publishers.

Sadasivuni, S. K., V. Sanderson, G. Bulat, and N. Swaminathan (2012, Jun). Application of scalar dissipation rate model to Siemens DLE combustors. In *Proc. ASME Turbo Expo*, Copenhagen. GT2012-68483.

Sankarakrishnan, R., K. A. Sallam, and F. W. Chambers (2005, Jun). Effects of turbulence on the breakup of round liquid jets in gaseous crossflow. In *Proc. ASME Fluids Engineering Division Summer Conference*, Houston, pp. 281–285. FEDSM2005-77407.

Sidhu, M. S. and A. A. Burluka (2008). Average vaporisation rate in turbulent subcritical two-phase flow. *Combust. Sci. Technol. 180*, 975–996.

Sirignano, W. A. (1983). Fuel droplet vaporization and spray combustion theory. *Prog. Energy Combust. Sci. 9*, 291–322.

Sirignano, W. A. (2010). *Fluid Dynamics and Transport of Droplets and Sprays* (2nd ed.). Cambridge: Cambridge University Press.

Smagorinsky, J. (1963). General circulation experiments with the primitive equations. Part 1: the basic experiment. *Mon. Weather Rev. 91*, 99–164.

Speziale, C. G., R. Abid, and E. C. Anderson (1992). A critical evaluation of two-equation models for near wall turbulence. *AIAA J. 30*, 324–331.

Stenzler, J. N., J. G. Lee, D. A. Santavicca, and W. Lee (1990). Penetration of liquid jets in a cross-flow. *Atomization Sprays 16*, 887–906.

Tabor, G. and M. Baba-Ahmadi (2010). Inlet conditions for Large Eddy Simulation: a review. *Comput. Fluids 39*, 553–567.

Temmerman, L., M. Hadziabdic, M. A. Leschziner, and K. Hanjalic (2005). A hybrid two-layer URANS-LES approach for Large Eddy Simulation at high Reynolds numbers. *Int. J. Heat Fluid Flow 26*, 173–190.

Vallet, A., A. A. Burluka, and R. Borghi (2001). Development of a Eulerian model for the atomization of a liquid jet. *Atomization Sprays 11*, 619–642.

Vuorinen, V., A. Chaudhari, and J.-P. Keskinen (2015). Large Eddy Simulation in a complex hill terrain enabled by a compact fractional step OpenFOAM solver. *Adv. Eng. Softw. 79*, 70–80.

Weller, H. G., G. Tabor, H. Jasak, and C. Fureby (1998). A tensorial approach to computational continuum mechanics using object-orientated techniques. *Comput. Phys. 12*, 620–631.

Wilcox, D. C. (1988). Re-assessment of the scale-determining equation for advanced turbulence models. *AIAA J. 26*, 1299–1310.

Williams, A. (1989). *Combustion of Liquid Fuel Sprays*. London: Butterworths.

Xue, Q., S. Som, P. K. Senecal, and E. Pomraning (2013). Large Eddy Simulation of fuel spray under non-reacting IC engine conditions. *Atomization Sprays 23*, 925–955.

Yuan, L., R. L. Street, and J. H. Ferzinger (1999). Large Eddy Simulation of a round jet in crossflow. *J. Fluid Mech. 379*, 71–104.

Zhao, B., C. Yang, X. Yang, and S. Liub (2008). Particle dispersion and deposition in ventilated rooms: testing and evaluation of different Eulerian and Lagrangian models. *Build. Environ. 43*, 388–397.

Zheng, Y. and A. W. Marshall (2011). Characterization of the initial spray from low-Weber-number jets in crossflow. *Atomization Sprays 21*, 575–589.